West Antarctica snow accumulation trend study (1979-2011) from Snow Radar and ice core profiles

by
Boyu Feng

Submitted to the graduate degree program in Geography and the
Graduate Faculty of the University of Kansas
in partial fulfillment of the requirements for the degree of
Master of Science

Dr. David Braaten, Chair

Dr. Xingong Li

Dr. Terry Slocum

Date Defended: August 15, 2014

The Thesis Committee for Boyu Feng certifies
that this is the approved version of the following thesis:

West Antarctica snow accumulation trend study (1979-2011) from Snow Radar and ice core profiles

Dr. David Braaten, Chair

Date Approved: Aug 21, 2014

Abstract

Ice sheets are under threat from increasing air and ocean temperatures. For Antarctica, observed changes are most apparent near the margins; inland the effects of a warming atmosphere and changing circulation patterns are less clear. Snow accumulation to the ice sheet offsets ice losses near the margin, and characterizing ice sheet accumulation rate is necessary for understanding ice sheet mass balance and predicting future sea level rise. Ice penetrating radar systems enable the measurement of ice sheet properties beneath the surface, such as ice thickness and internal layering. This study concentrates on mapping the depth of internal layers, and linking the layers to a chronology that allows snow accumulation rates over particular time periods to be determined. The focus is on one particular ice penetrating radar system: Snow Radar from the Center for Remote Sensing of Ice Sheet (CReSIS). The Snow Radar is a 2-8 GHz ultra-wideband (UWB), frequency-modulated, continuous-wave (FMCW) radar, having a ~5cm vertical resolution. The chronology of Snow Radar detected layers is validated to be annual layers using nearby ice core data and the results of a regional climate model (RACMO2.1/ANT). The measurement error of a manual layer picking procedure, and proximity of ice core density profiles to the Snow Radar data have been examined. The results show that the average error variance in manual picking is as small as 3.0e-4 m, and that it is reasonable to use ice core density profiles in Snow Radar data processing. Using Snow Radar data, a snow accumulation rate time series has been determined along two flight lines over West Antarctica. The spatiotemporal distribution of

snow accumulation has been analyzed and possible explanations for such distribution are discussed. No significant trend is found in snow accumulation during the 33-year study period (1979-2011). The snow accumulation spatial distribution has been related to topography and wind, showing that snow accumulation has a negative correlation with elevation and is generally lower on leeward slopes than on the windward slopes.

Acknowledgements

Two years ago, I first came to the U.S. knowing nothing about this country nor my subsequent research. But today I have made a lot of friends on the land far away from home and my thesis is finally finished. On this journey, I obtained a lot of help from different people, some of whom I may never have the chance to return the favor. Thus, I would like to express my gratitude to them here, because without their help I could not even think about finishing my thesis. In the first place, I thank my parents who are currently in China. It is them that support me to overcome the obstacles along the way. My advisor Dr. Braaten is the best mentor I can wish for, who helps me in my study and my life in the U.S. Dr. Paden in CReSIS gives me a lot of help in programming, which I am very thankful. I appreciate the suggestions and ideas provided by my committee members Dr. Slocum and Dr. Li. I am also obliged to my coworkers Kyle and Trey, who patiently explained the complex data structure in CReSIS to me when I firstly started my work there. And in later times, they solved the problems I encountered uncounted times. Additionally, I have to thank CReSIS for providing such a great opportunity for me to do this research and giving me the access to its unparalleled dataset that I would not be able to use elsewhere. In the end, I thank my friends in Lawrence and in China who gave me support during the last two years. Thank you all very much for your support, which means millions to me!

Contents

List of Figures

List of Tables

1 Introduction

1.1 Background

Human society is now faced with unprecedented challenges from global climate change. The observed worldwide glacier melting and sea level rise reflect the warming underway. The Intergovernmental Panel on Climate Change (IPCC) special report (Field, 2012) has identified direct regional impacts from climate change in polar regions and expects further impacts with global implications through various processes and feedbacks (Seneviratne et al., 2012). In the recent IPCC Fifth Assessment Report (AR5), more evidence from improved technologies have become available to confirm further ice loss from both the Greenland and Antarctic ice sheets (Stocker et al., 2013) since the release of AR4. During the post-1970 global warming period, the ice sheets have encountered impacts from increasing air and ocean temperatures. Significant glacial retreat and wastage were found worldwide; the rates of retreat exceed the historical record and natural variability since the beginning of the 21st century.

In the Arctic, the world's second largest ice body Greenland is experiencing accelerated ice sheet melting and discharge. This melting is most likely irreversible even if atmospheric composition and the

global climate go back to the pre-industrialization period (Gregory et al., 2004). Combining 18 recent studies on the Greenland ice sheet, the IPCC AR5 points out that the average ice mass change to Greenland has been –121 [–149 to –94] Gt/yr (a sea level equivalent of 0.33 [0.41 to 0.26] mm/yr) over the period 1993 to 2010, and –229 [–290 to –169] Gt/yr (0.63 [0.80 to 0.47] mm/yr sea level equivalent) over the period 2005–2010 (Stocker et al., 2013).

Meanwhile, ice mass loss in Antarctica is noticeable, though at least to date is less extensive than it is in the Arctic. A conclusion based on 10 studies has been made in the IPCC AR5 that the average ice mass change to Antarctica from the present assessment has been –97 [–135 to –58] Gt/yr (a sea level equivalent of 0.27 mm/yr [0.37 to 0.16] mm/yr) over the period 1993–2010, and –147 [–221 to –74] Gt/yr (0.41 [0.61 to 0.20] mm/yr) over the period 2005–2010. The cumulated Antarctic ice mass loss concluded from the 10 studies is shown in **Figure 1.1**. West Antarctica (WA) is more vulnerable than East Antarctica (EA), as much of it lies below sea level, with glaciers rapidly flowing to form floating ice shelves at the margin. Basal melting of ice shelves by warmer ocean temperatures is proposed as another key mechanisms facilitating mass loss of the marine-based West Antarctic ice sheet (WAIS) (Hellmer, 2004; Pritchard et al., 2012). The condition in EA is more stable, with some inland areas experiencing a mass gain (Davis et al., 2005; Wingham et al., 2006).

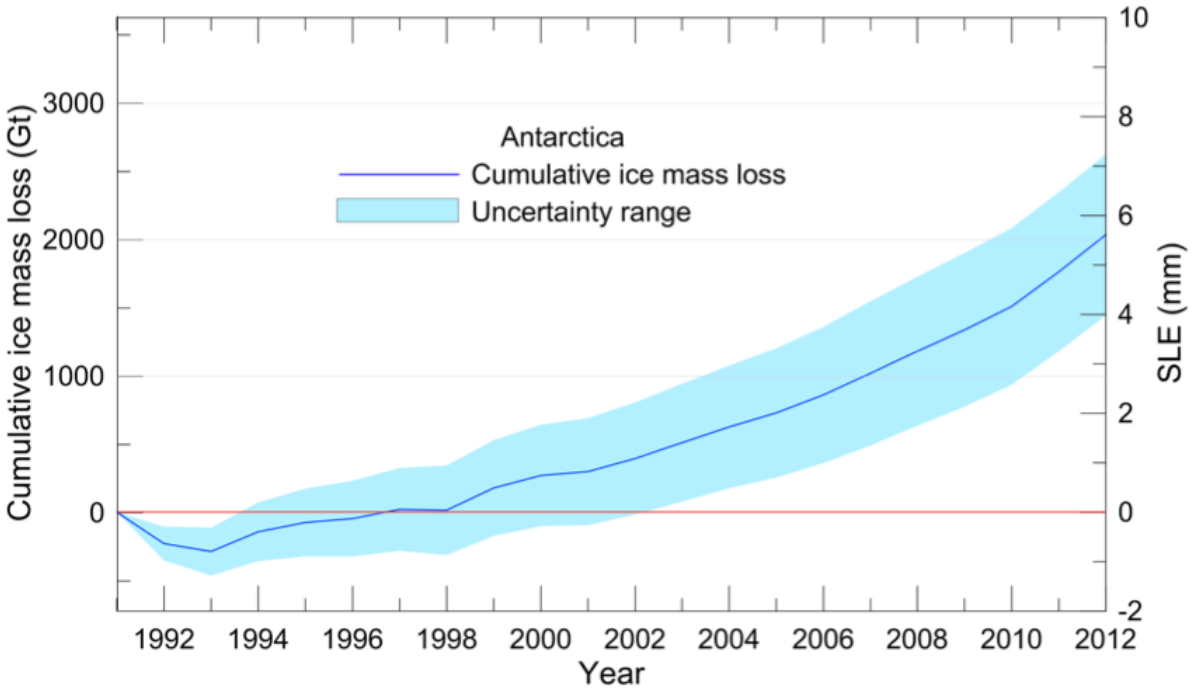

Figure 1.1 Cumulative ice mass loss (and sea level equivalent, SLE) from Antarctica derived as annual averages from 10 recent studies (Stocker, Dahe et al. 2013).

Owing to instability and its large volume, WA may become the biggest contributor to future sea level rise (Oppenheimer, 1998). Compared to the ice sheet in EA, WAIS has thicker internal layers along with easier annual layer detection property of the recent past, afforded by its higher accumulation rate. Answers and projections for sea level rise lie in Antarctica's responses and feedbacks on climate change. The dynamics of ice mass balance in WA, concerning precipitation and glacier discharge, is of great interest. The internal characteristics of ice sheets are valuable for learning about past climates and predicting future ice mass balance.

Myriad scientific observations have been made to understand ice sheet mass balance. Among the different methods, ice penetrating radar, because of its high spatial resolution, extensive coverage when

mounted on aircraft, and ability to penetrate below the surface of the ice, has become essential to glaciology. This research uses data from the airborne Snow Radar system, a system designed to provide high resolution, near-surface characteristics of the ice sheet. When annual layering can be detected, annual snow accumulation can be estimated. Using the MATLAB-based layer picking software (Picker) developed by CReSIS, the depth of internal layers detected by the Snow Radar are tracked. If these reflectors correspond to annual markers, annual accumulation may be determined. Using the distance between the individual reflectors and available density profiles from nearby ice cores, water equivalent accumulation for each annual layer can be determined from the time of the radar measurement to decades earlier. The number of years that can be analyzed depends on the local accumulation rate and snow characteristics. In this study accumulation was determined back to 1979.

1.2 Antarctic Ice Sheet Dynamics

Antarctic ice sheet (AIS) dynamics depends on the ice input through precipitation and output near the margins of the ice sheet through glaciers calving. The input of an ice sheet is through precipitation, mainly as snow, which then is compacted to form glacier ice and moves under gravity towards the coast. Inland, ice flow rates can be as low as a few meters per year, mostly due to internal deformation; while nearer the coast ice flow tends to be faster (up to hundreds or even thousands of meters per year) and most of it is carried to the coast by fast moving ice streams (Rignot et al., 2011). In terms of ice sheet output, at the beginning of glaciers calving, vast floating ice shelves form as coastal ice streams begin to float at the grounding zone, the transition region between the fully grounded ice sheet and the

free-floating ice shelf. These shelves then melt from below or calve off to give icebergs that eventually melt. If the transfer of the ice from the land to the sea is balanced by snow falling back on the land then there will be no net change to ice mass or contribution to sea level change.

In Antarctica, an increasing number and enlarging scale of ice shelf collapses have been identified (King et al., 2012; Rignot, 2006; Rignot et al., 2008), causing a further acceleration of ice flow near the coast (Joughin and Alley, 2011). Thus, the output of ice from AIS has been shown to be increasing. In terms of precipitation input to AIS, the snow accumulation rate in West Antarctica (WA) has been found to be in balance (Lenaerts et al., 2012a; Medley et al., 2013) or even decreasing over recent decades (Burgener et al., 2013). The snow accumulation rate trend in East Antarctic Ice Sheet (EAIS) is stable or experiencing a slight increase (Davis et al., 2005; Wingham et al., 2006).

1.3 Integral Ice Sheet Observation

Key methods used to determine the ice sheet mass changes of Antarctica include: altimetry; long-term changes in gravity field from the Gravity Recovery (GRACE), and the mass budget method (IPCC AR5) (Stocker et al., 2013).

The launch of the European Remote-sensing Satellites ERS-1, ERS-2, and Envisat satellite triggered a series of altimetric observations concerning the shape and volume of ice sheets. Altimetry is a powerful tool for ice sheet observation and has been widely used (Davis, 2005; Griggs, 2011; Wingham, 2006; Zwally, 2005). The changes in the volume of the ice sheet are gained by repeatedly measuring the height

of the ice-sheet surface. The changes in ice elevation and topography deduced from altimetry provide insights into important processes on the ice sheet. Moreover, altimetry also provides other information such as backscatter and waveform shape that can be used to characterize surface roughness or snow pack properties (Rémy, 2009). Another important method to estimate the ice mass balance is through temporal changes of the gravity field. The GRACE satellites enable the measurement of changes in ice-sheet mass via repeated and very accurate measurement of the Earth's gravity field (Chen et al., 2009). A myriad of studies have applied GRACE data to AIS mass balance (Ivins et al., 2013; Velicogna, 2009).

For two of the methods, radar altimetry and GRACE, the consistency in their results is striking (Chen, 2013; Horwath, 2012; Horwath, 2009). Comparison and joint interpretation of results from the ENVISAT radar altimetry and GRACE illustrate an agreement in the spatial patterns of linear trends over a common period, not only for the extreme ice losses in the Amundsen Sea Sector of WA but also for an alternating sequence of gains and losses along the East Antarctic coast (Horwath, 2012).

The mass budget method estimates the difference between the input (net surface mass balance derived from a meteorological model) and output (perimeter ice discharge flux derived from measurements of ice velocity and ice thickness at the grounding line) over the ice sheet (Stocker et al., 2013). The meteorological model estimates the net snow accumulation rate from precipitation, surface sublimation, meltwater runoff, erosion by drifting snow, and sublimation of drifting snow. Currently, the regional climate model becomes more and more popular than other meteorological model methods (recalibrated

or corrected with in situ data, downscaling of global reanalysis data, or interpolation of in situ measurements) (Stocker et al., 2013), probably due to its finer spatial resolution and practical computing time. This estimation provides the input of ice sheet mass. The ice output is given by ice surface velocity data from satellite radar interferometry and ice thickness at the grounding line provided by ice penetrating radar.

Altimetry, GRACE and the mass budget method provide reliable observations in assessing the mass balance of the AIS, but need validation. The ice sheet itself contains information that may be used for validation. Information can be accessed through ice cores and the application of ice penetrating radar.

1.4 Ice Cores

A common way to get past climate information is by obtaining an ice core. Ice cores contain abundant information about climate. Depending on isotope and chemical variations in the deposited snow and gases trapped within bubbles, proxy records for many aspects of the paleoenvironment can be obtained, including temperature, ice accumulation rate, moisture source, atmospheric dust loading (and dust source), greenhouse-gas concentration, and bioproductivity (Morse et al., 2002). In many locations in Antarctica the air temperature is always below the freezing point of water, which assures well-structured and well-preserved ice cores.

Using density, stable isotope, and conductivity profiles derived from ice cores, it is possible to construct an annual accumulation series at each site and then beyond using interpolation methods. Several ice

cores from the U.S.-International Trans-Antarctic Scientific Expedition (ITASE) in WA have assisted in the calculation of snow accumulation over time and space, from which maps have been created (Kaspari et al., 2004; Medley et al., 2013; Morse et al., 2002). The new ice cores from Satellite Era Accumulation Traverse (SEAT) team in 2010 provide an additional data source to the former ITASE dataset. Among SEAT ice cores, the SEAT-10-1 is in the same location of ITASE-00-1, which was drilled in 2001. Though ice core data provides high temporal resolution, it has low horizontal resolution for snow accumulation studies. When using an ice core it is important to consider the effects of small-scale perturbations from topography and wind redistribution.

1.5 Ice Penetrating Radar System

By collecting several ice cores, an accumulation rate study may ensure a reliable result (Burgener et al., 2013). But ice core data still can hardly cover and represent the broad WA area; thus the snow accumulation trend derived from ice cores only represents the local condition, not a trend over a region. Ice penetrating radar complements ice core data by linking a wide area to a core using radar on airplanes or ground-based vehicles.

In 1933, U.S. Army researchers first found the ice penetrability of a radar signal in very high frequency (VHF, 30 MHz ~ 300 MHz) and ultra high frequency (UHF, 300 MHz ~ 3 GHz) bands (Allen). This finding led to the realization that a radar could be used to retrieve thickness and other internal features of ice sheet. The use of ice penetrating radar or radio-echo sounding (RES) to obtain internal information of the ice sheet began in early 1960s (Evans and Smith, 1969). Other studies continued to explore new

applications of ice penetrating radar. Besides the ice thickness and bed feature detection (Alley et al., 1986; Drewry, 1975; Shabtaie and Bentley, 1988), the internal layers detected by radar were also found to yield important information, including volcanic eruptions (Millar, 1982), aquifers(Bamber, 1987; Davis et al., 1990), and snow accumulation patterns (Nereson et al., 2000).

1.5.1 Snow/Ice Properties

The detected internal layers depend both on the snow/ice properties and radar features. It is the abrupt changes in snow/ice properties that produce radar reflections during its propagation. For radar of different frequency and bandwidth, the type or threshold of such changes in snow/ice properties that cause radar reflections are different. Three snow/ice properties are found to be responsible for the majority of radar reflections (internal layers): snow/ice density, acidity, and crystal orientation fabrics (Ackley and Keliher, 1979; Fujita et al., 1999; Fujita et al., 2000; Hammer, 1980; Harrison, 1973). While the snow/ice density and crystal orientation fabrics cause radar reflections through permittivity[1] variations, acidity causes radar reflections through conductivity variation. At different depths, the influences from those properties towards radar reflection vary: density change governs the radar reflection from the surface down to 700-900 m; below 700-900 m, changes in acidity and crystal

[1] The permittivity is an electromagnetic property of a medium concerning the resistance that is encountered when forming an electric field in the medium. It is often given as relative permittivity, which equals to the ratio of the magnitude of the external electric field and the magnitude of the internal resisting electric field. The relative permittivity is the same concept as the complex dielectric constant, mentioned in **2.3.2 Retrieving Snow Accumulation Rate from Radar Data Using TWTT** that portraits the change of the electric field when it propagates in a medium.

orientation fabrics both appear to be the reason for radar reflection (Fujita et al., 1999; Fujita et al., 2000).

The specific mechanism, characterizing radar reflections related to snow/ice properties (density, acidity, and crystal orientation fabrics), is defined by the power reflection coefficient. The power reflection coefficient describes the amplitude of a reflected wave relative to that of the incident wave. In the case of ice penetrating radar, this coefficient can be expressed as below (Ackley and Keliher, 1979; Moore, 1988):

$$\boldsymbol{r_i = \frac{Z_{i-1} - Z_i}{Z_{i-1} + Z_i}}, \tag{1.1}$$

where Z_{i-1} is the characteristic bulk impedance of the (i-1) th ice sheet internal layer and Z_i is the characteristic bulk impedance of the i th ice sheet internal layer.

According to Paren and Fujita, the power reflection coefficients caused separately by permittivity and conductivity are proportional to the square of the changes in permittivity ($\Delta\varepsilon$) or conductivity ($\Delta\delta$) respectively (Fujita and Mae, 1994; Paren, 1975). In fact, the power reflection coefficient (r_i) is connected to the actual radar received power (P_R) by a radar equation as below (Fujita et al., 1999):

$$\boldsymbol{P_R = \frac{P_T G^2 \lambda^2 q r_i}{64\pi^2 \zeta^2 L}}, \tag{1.2}$$

where P_T is the transmitted power; G, λ, and q are antenna gain, wave length in vacuum, and "reflection gain"; r_i is the power reflection coefficient; ζ is the depth to the reflector retrieved from the travel time of electromagnetic waves in ice; and L is the loss factor due to energy absorption.

1.5.2 Snow Radar Features

Radar specifications, including frequency, bandwidth, pulse length, and antenna properties, govern the magnitude and shapes of its reflections. Different radar systems have different strengths and weaknesses for a particular application. Thus, for measurements of near-surface internal layers of an ice sheet, the radar system is designed to detect internal layers with high vertical resolution.

The radar system used to collect the data used in this research is a UHF, ultra-wideband (UWB), and frequency-modulated continuous-wave (FMCW) radar—Snow Radar, designed by CReSIS. The UHF feature of this radar guarantees the strong penetrating ability. UWB radar is suggested to ensure a fine vertical resolution (Kanagaratnam et al., 2004), with a trade-off of a shallower penetrating depth. The FMCW feature further increases the vertical resolution to ~5cm, the penetrability of the Snow Radar signal, and also simplifies the modulation and operation of the radar system (Butler et al., 2007). In this radar, a long chirp signal (~250 μs) is generated which sweeps linearly in frequency from the start frequency to the stop frequency. With this particular design, Snow Radar aims at mapping near-surface internal layers with fine resolution and determining the spatial and temporal variability of the snow accumulation rate (Gogineni et al., 2003; Panzer et al., 2013).

The Snow Radar is carried by flights from the NSF, CReSIS, and NASA IceBridge projects, which combines multiple instruments to map ice surface topography, bedrock topography beneath the ice sheets, grounding line position, and ice and snow thickness. This research uses Snow Radar data from the 2011 Antarctica NASA IceBridge DC-8 mission, which has a frequency of 2 GHz~6 GHz and chirp duration of 255 μs. The raw radar data are processed using a model-based approach that generates radar echograms.

1.6 Research Questions

The internal reflectors from the ice penetrating radar, especially new ones like Snow Radar, are still in the process of being understood (Eisen et al., 2004; Rotschky et al., 2004). As the radar echo has associated noise, the verification of the radar echo internal layers becomes a key step in interpreting ice penetrating radar data. Ice core data is an important input. High consistency between the patterns in the ice core and radar echogram can be persuasive evidence for the cause of internal layers seen in radar echograms.

The Snow Radar is a system designed and built by CReSIS to measure snow thickness and internal layers within ice sheets (Panzer et al., 2013). The initial research has demonstrated that the internal layers detected by the Snow Radar are annual layers in high accumulation regions with annual accumulation greater than 0.25 m water equivalent in WA (Medley et al., 2013). But the definition of a layer (annual or multi-annual) is less certain in low accumulation regions. Thus, comparison between Snow Radar data and nearby ice core data in both high and low accumulation areas are made to answer

the question: **(1) What is the chronology of the prominent internal layers detected by the Snow Radar in West Antarctica? Are they annual layers, a mix of annual and multi-annual layers, or are they completely uncoupled from annual cycles? What are the limitations of annual layer detection for the Snow Radar?**

Ideally, the Snow Radar has a resolution to correctly detect annual layers, which would provide a dataset for annual accumulation rate calculation. If this is the case, the internal annual layer detected by the Snow Radar is a valuable data source for temporally tracing the variability in WAIS snow accumulation over a large area, which can be used to address the question: **(2) How does the WAIS accumulation and surface mass balance change over space and time periods? How do ice core and regional climate model derived average accumulation rate and accumulation rate trends compare with those derived from Snow Radar?**

Another important data source in the assessment of ice sheet accumulation is in situ weather station records. Local weather conditions can provide insights into precipitation and redistribution of snow. For this study, Byrd station (80°S, 119°W) is close to the Snow Radar segments. At this site, 3-hourly observations of surface temperature, pressure and winds are available for over 3 decades from automatic weather station (AWS) records. In addition, the sea ice extent (SIE) in Antarctica has also experienced changes. Though sea ice changes in the Amundsen Sea have been small, the annual variations in SIE near the study area could influence snow accumulation. This study relates the Byrd AWS dataset and SIE dataset from the National Snow and Ice Data Center (NSIDC) with radar determined snow

accumulation data to answers the question: **(3) What are the relationships between regional WAIS snow accumulation and long-term Automatic Weather Station (AWS) observations and SIE observations?**

1.7 Thesis Outline

This thesis contains 5 chapters plus appendices to thoroughly document my analyses undertaken and results obtained during the quest to answer the above research questions. The structure of this thesis is:

Chapter 1: The background on WAIS, key methods for ice sheet monitoring, ice core applications, and principles in ice penetrating radar are covered.

Chapter 2: Study area, available datasets and the necessary data prepossessing (extracting annual snow accumulation from Snow Radar and taking care of missing data in Byrd station archive) are covered.

Chapter 3: Measurement error analysis and statistical methods are covered, including the definition of picking error, influence from the extrapolation of density profiles, Mann-Kendall trend test, and Wilcoxon rank sum test.

Chapter 4: Results and analyses are covered. In the sequence of the three research questions, this chapter provides evidence on the chronology of Snow Radar detected layers, the long period trend of what in derived SWE series, and the correlation among snow accumulation, AWS, and SIE data. In addition, the

annual layer detection limit in Snow Radar and the spatial distribution of snow accumulation are discussed.

Chapter 5: Conclusions are given. The problems encountered in this study are provided to shed light on continuing work with this dataset and in planning future field experiments.

2 Available Data and Data Preprocessing

2.1 Study Area

Considering the data availability and earlier ice sheet accumulation distribution studies (Burgener et al., 2013; Medley et al., 2013; Morse et al., 2002), I choose a broad region in central WA, most of which is on the north side of Ross/Amundsen ice-flow divide. In particular, two 2011 Antarctic DC-8 mission flight segments[2] were selected, one is flown on November, 9th, 2011 (20111109_02); the other is flown three days later on November, 12th, 2011 (20111112_01). Subsections of these two flight segments were studied in this research: the frames[3] from 20111109_02_112 to 20111109_02_196 (approximately 370 km) and the frames from 20111112_01_286 to 20111112_01_295 (approximately 45 km) (**Figure 2.1**). As there is no duplicate frame number among the frames that have been analyzed in this research,

[2] A segment is a contiguous dataset where the radar settings do not change. The segment ID is YYYYMMDD_SS where YYYY is the 4-digit year (e.g. 2011), MM is the 2-digit month from 1 to 12, DD is the 2-digit day of the month from 1 to 31, and SS is the segment number from 0 to 99. Segments are always sorted in the order in which the data was collected.

[3] Each segment is broken into frames to make analyzing the data easier. Frames span 33 seconds covering 4 to 5 km dependent upon aircraft speed. The frame ID is a concatenation of the segment ID and a frame number and follows the format YYYYMMDD_SS_FFF where FFF is the frame number from 000 to 999.

the rest of the thesis uses only frame number (FFF), instead of frame ID (YYYYMMDD_SS_FFF), to identify the frame. It should be noted that the frame numbers mentioned in this thesis correspond to an earlier processed version of the dataset, rather than the current dataset that can be downloaded from the CReSIS website. The currently available Snow Radar data divides the flight line into slightly differently segments and has renumbered the frames. Frame numbers 112 to 196 used in this study correspond to frame numbers 140 to 232 in the currently available dataset; and the frame numbers 286 to 295 used in this study correspond the frame numbers 313 to 321 in the currently available dataset.

Studied frames on segment 20111109_02 experience an accumulation change along the line probably due to changes in elevation. Two shallow ITASE (Mayewski et al., 2005) ice cores (ITASE-00-1 and ITASE-01-3) are located near the beginning and ending points of the selected study frames on this segment. Segment 20111112_01 is closer to the coast and passes over ice core ITASE-01-2. Among the three ice cores, ITASE-00-1 (79.38°S, 111.24°W) is closest to the Byrd station (~100km). ITASE-00-1 and ITASE-01-3 (78.12°S, 95.64°W) are located along segment 20111109_02, and ITASE-01-2 (77.84°S, 102.91°W) is located on segment 20111112_01, which is closer to the coast, flown 3 days later.

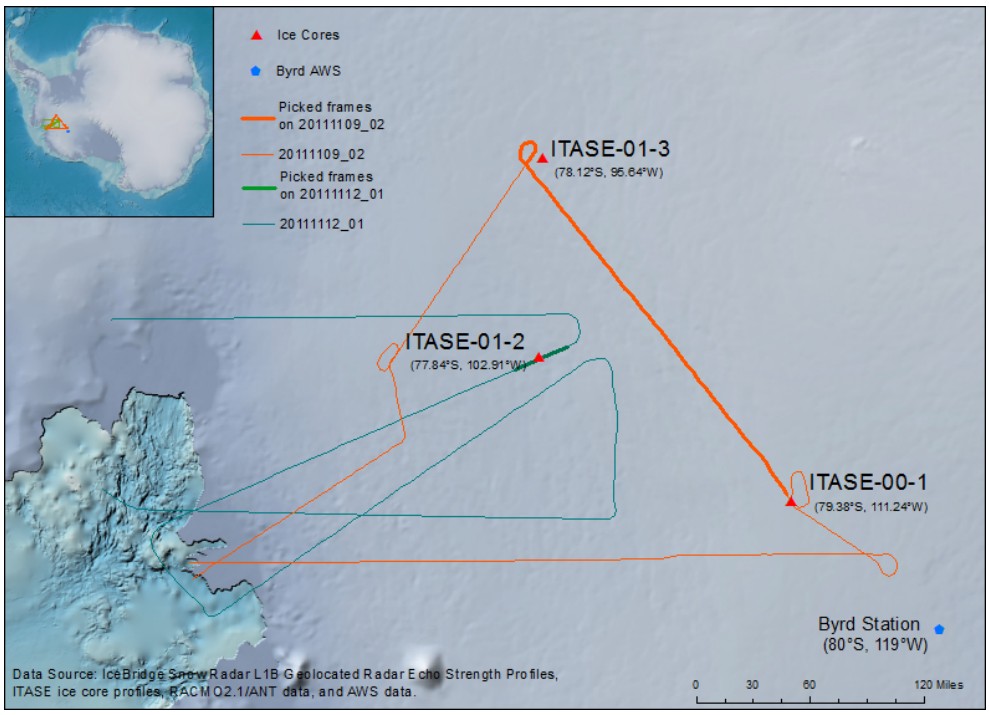

Figure 2.1 Study Region in WA indicating flight, ice cores and Byrd station locations.

2.2 Available Dataset

This research made use of five datasets: ITASE ice core profiles; airborne Snow Radar data; regional climate model (RACMO2.1/ANT) data; weather archive from the Byrd station; and satellite-derived Bellingshausen and Amundsen seas sector SIE records. All datasets cover the 33-year time period from 1979 to 2011, except for the Byrd AWS data that cover from 1980 to 2011, and the ITASE ice core data that cover from 1979 to 2001(ITASE-01-3 and ITASE-01-2) and 1979 to 2000 (ITASE-00-1).

The ITASE project has been collecting Antarctic ice core data since 1990. This study uses 3 ice core profiles (ITASE-00-1, ITASE-01-2, and ITASE-01-3) from the ITASE project (Mayewski et al., 2005). The ITASE-00-1 was drilled during the 2000/01 field season and reaches a depth of about 105 m, going back 348 years to 1653; ITASE-01-02 was drilled during the 2001/02 field season and reaches 71 m back 113 years to 1890; and ITASE-01-3 was drilled during the 2001/02 field season and reaches 71 m back 143 years to 1859. The ice core profiles provide snow accumulation water-equivalent (m), layer thickness (m), depth (m), date the snow was deposited, and density (g/cm^3) (**Figure 2.2**). The ITASE cores have been dated by annual-layer counting, primarily through the identification of summer peaks in non-sea-salt sulfate ($nssSO_4^{2-}$) concentration; the absolute dating accuracy of better than 2 years and relative dating accuracy better than 1 year is demonstrated by the identification of multiple volcanic marker horizons in each of the cores (Steig et al., 2005).

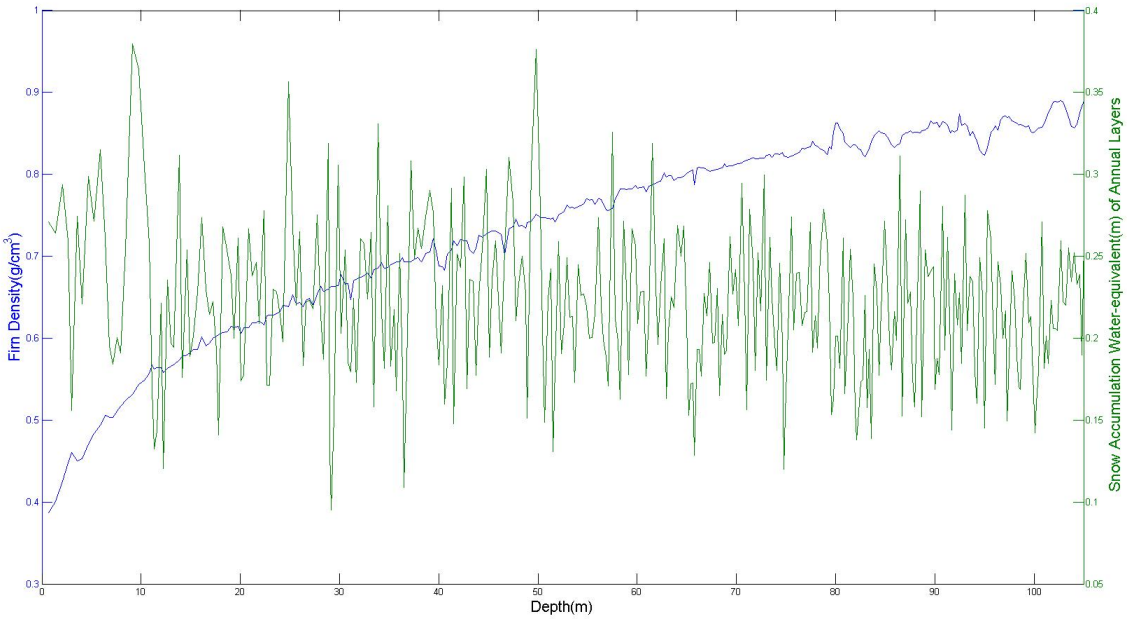

Figure 2.2 Ice core density and annual snow accumulation water-equivalent profiles against depth (ITASE-00-1).

During November 2011, Snow Radar data were obtained for large areas in West Antarctica, including a flight segment that passed within ~70 km of Byrd Station. This segment includes data frames from 112 to 196 (Leuschen, 2010). This research used IceBridge Snow Radar Level-1B Geolocated Radar Echo Strength Profiles (IRSNO1B), which includes echograms with measurements for time, latitude, longitude, elevation, as well as flight path charts and echogram images. This dataset is available in Matlab format (.mat), stored in the main processer in CReSIS and can be accessed through the Picker, a Matlab based software developed by CReSIS to pick the visible layers from radar echograms (**Figure 2.4**).

The RACMO2.1/ANT climate model provides additional snow accumulation data over the study region. This climate model predicts snow accumulation data as the sum of precipitation, surface sublimation,

runoff due to melt and erosion by drifting snow and sublimation of drifting snow per unit area (Lenaerts et al., 2012a). The atmospheric dynamics in RACMO2.1/ANT are from the High Resolution Limited Area Model while the description of the physical processes is adopted from the European Centre for Medium-Range Weather Forecasts. The current available data covers a time period from 1978 to 2012 with monthly temporal resolution and a 27 km spatial resolution. It is a gridded dataset and each record provides average surface mass balance, and latitude and longitude for the center of the grid cell.

The surface weather observations were provided by the Antarctic Meteorological Research Center (AMRC), an Antarctic research program funded by the National Science Foundation (NSF) that is based out of the Space Science and Engineering Center (SSEC) at the University of Wisconsin (Lazzara et al., 2012). The AMRC has several automatic weather stations (AWSs) in Antarctica. The Byrd AWS used in this research has one of the longest data records on the continent (1980 to present). Additionally, nearby flight routes and ice core data are available. Surface temperature, pressure, wind speed, and wind direction every 3 hours are included in the Byrd AWS records.

The National Snow & Ice Data Center (NSIDC) provides comprehensive cryosphere sea ice extent (SIE) data. For the Bellingshausen and Amundsen seas sector (60°W–120°W, **Figure 2.3**) in the study region, sea ice information is available through the time period of 10/26/1978 to 12/31/2012. Along with one historical dataset from the Electrically Scanning Microwave Radiometer (ESMR), this data product was derived from the Scanning Multichannel Microwave Radiometer (SMMR), the Special Sensor Microwave/Imager (SSM/I), and the Special Sensor Microwave Imager/Sounder (SSMIS). The dataset

was computed using the NASA Team algorithm, and the product is provided by the NASA Goddard Space Flight Center (GSFC). It is a daily dataset, with a two-day time resolution before July, 9, 1987 and daily time resolution starting in July, 9, 1987.

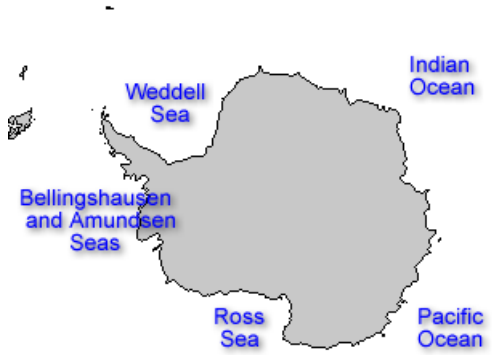

Figure 2.3 Bellingshausen and Amundsen seas sector study region used to study sea ice changes.

2.3 Snow Radar Data Preprocessing

Although automatic picking and tracing of internal layers shows some promise (Crandall et al., 2012), current algorithms cannot reliably track internal layers seen in radar echograms. In order to get the snow accumulation rate from Snow Radar data, the internal layers in echograms need to be manually traced through a region of interest. Initially, the internal layers were extracted using software code known as the "Picker", Matlab based code developed by CReSIS to pick the visible layers from radar echograms. The Snow Radar data have been previously loaded onto the OpenPolarServer (OPS), a CReSIS developed spatial database based on GeoServer. Data on the OPS can be accessed and processed through

the Picker. Every layer picked using this software has a separate file containing the two-way travel time, longitude, latitude and elevation, etc. for every picked point in the layer. The key extracted layer information that is needed for layer thickness calculation is two-way travel time (TWTT) of the reflected radar signal. The TWTT of the radar reflectors can be converted to depth, layer thickness, and water-equivalent using a simplified radar signal propagation model that uses a snow density profile.

2.3.1 Manually Tracing Internal Layers

Visually tracing internal layers in the echograms is the first step in generating the snow accumulation dataset. The Snow Radar echograms can be accessed through the Picker (**Figure 2.4**). The visible internal layers are the detected radar reflections. The clarity of these layers depends heavily on the raw signal processing, local snow accumulation condition, and the radar features.

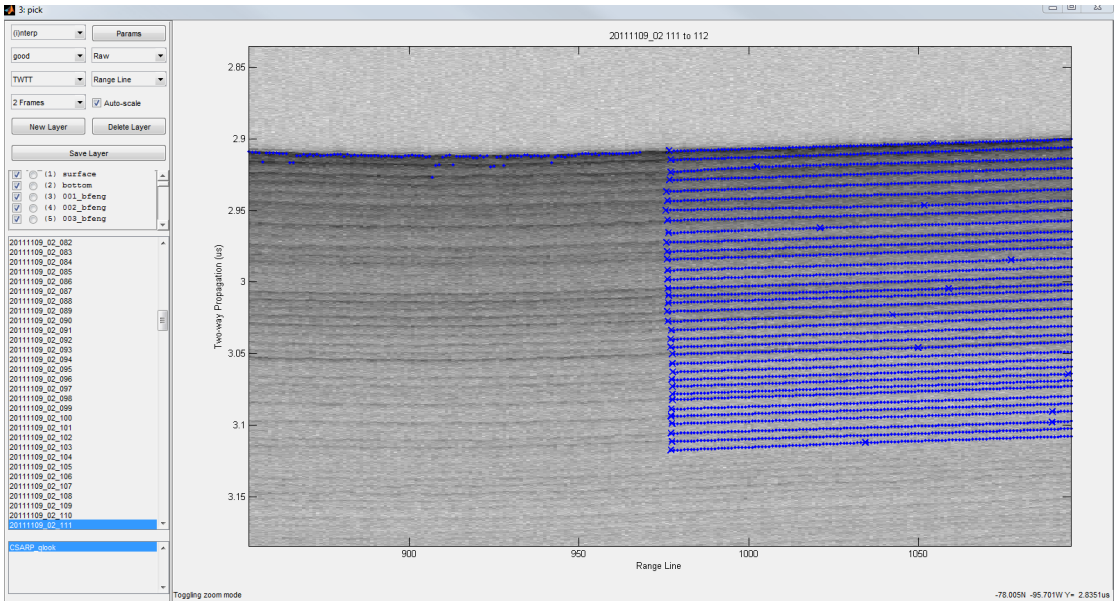

Figure 2.4 A screen shot of the Picker user interface when doing picking.

During the picking, I found that most of the layers were easily distinguishable, but there were also blurry areas in echograms that were difficult to pick. On the other hand, although most of the internal layers can be traced throughout the continuous frames, a few layers were found to be discontinuous. One discontinuous layer appears in frames 140 to 145 between the 14th and 15th layers (**Figure 2.5**). Two discontinuous layers appear in frames 190 to 195 separately between 13th, 14th, and 15th layers (**Figure 2.6**).

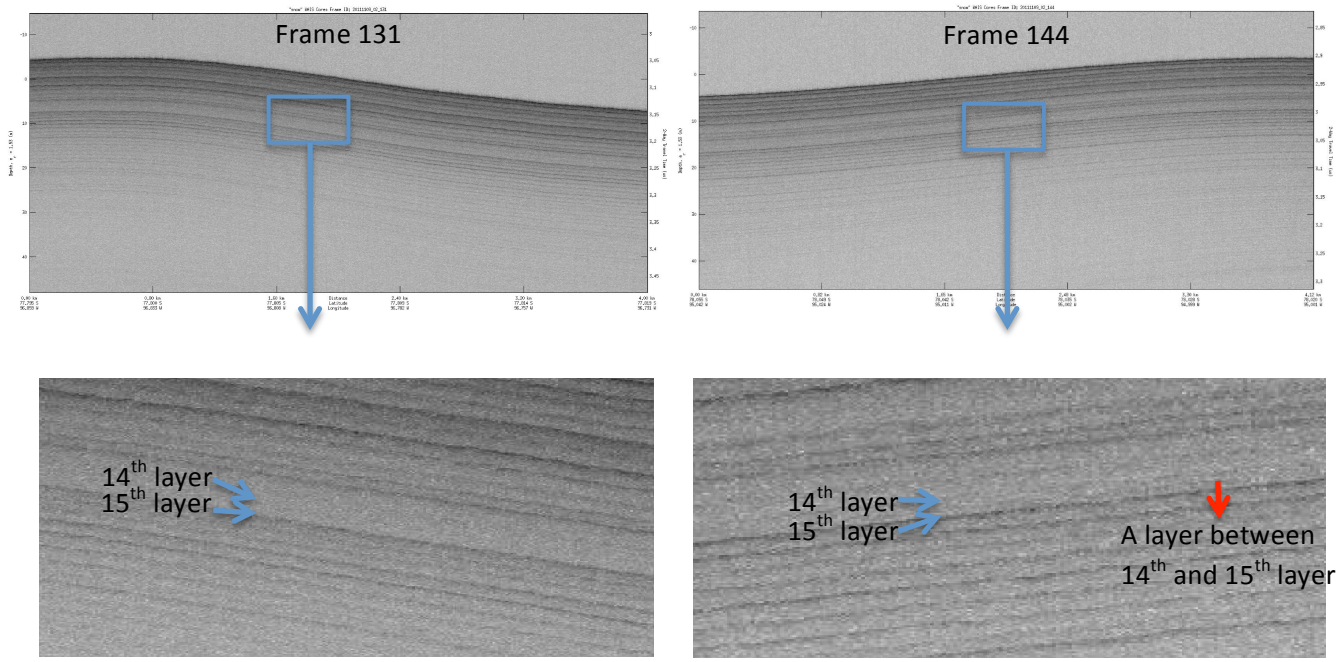

Figure 2.5 Discontinuous layer in echogram from frame 131 (no layer between 14th and 15th layer) and 144 (an extra layer between 14th and 15th layer).

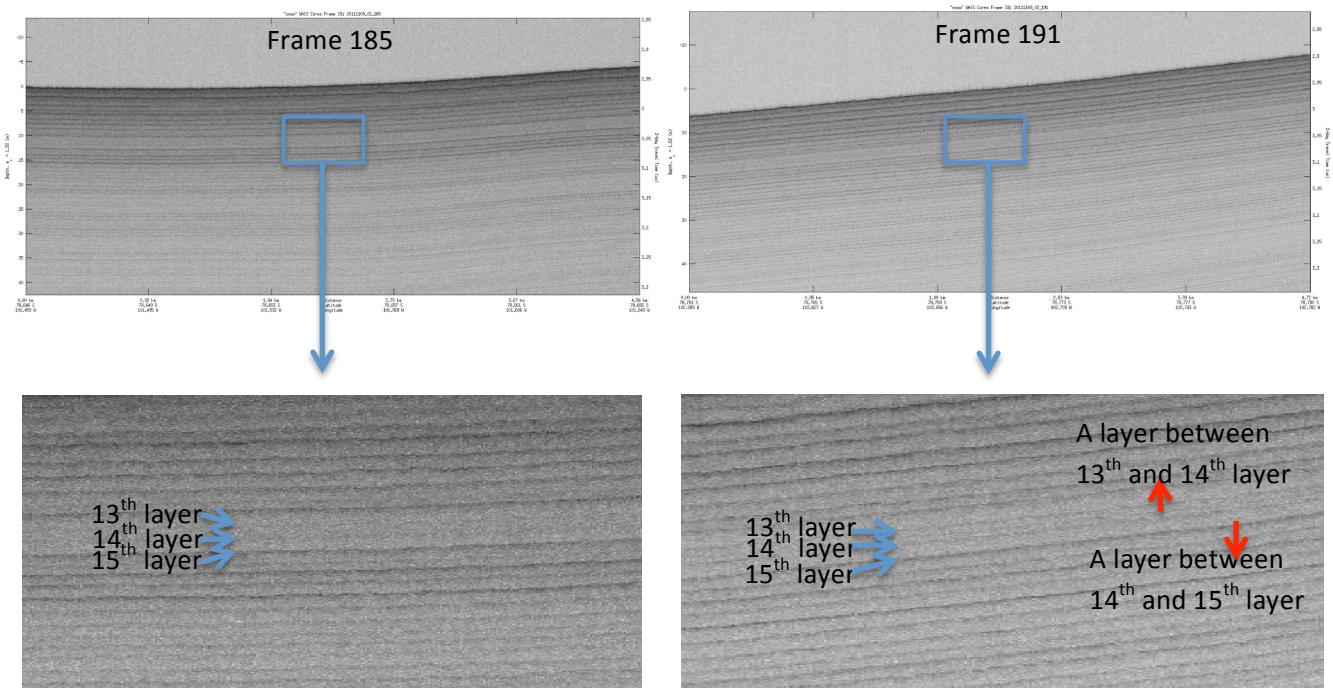

Figure 2.6 Discontinuous layer in echogram from frame 185 (no layer between 13th, 14th and 15th layer) and 191 (two extra layers separately between 13th, 14th and 15th layer).

Discontinuous layers are not uncommon in ice penetrating radar systems and various explanations may apply. An obvious explanation for discontinuous layers is that there is an actual layer separation caused by local differences in snow accumulation rate (Jacobel and Hodge, 1995). The discontinuity is also found to be more common with increasing depth, especially as the bed is approached, since the layer pattern near the bed is influenced more by the basal topography (Jacobel and Hodge, 1995; Morse et al., 1999). Yet, it is stated that in shallow layers, e.g. layers studied by this research (depth < 30 m), the relative features of the layers are primarily controlled by burial rate (Morse et al., 1999).

In my case, the example shown in **Figure 2.5**, the discontinuous layer in frame 141 to 143 is likely related to the high snow accumulation aspect of this location. The average annual snow accumulation

water-equivalent derived from frame 141 to 143 was found to be 0.4077 m. The snow/ice properties in this high accumulation area may produce an additional reflector within an annual layer, which then disappears as the snow properties change. In the example shown in **Figure 2.6**, the discontinuous layers in frames 193 to 195 may result from the low snow accumulation rate in this location. The average annual snow accumulation water-equivalent within these three frames is 0.2364 m. This could be due to the nature of the reflectors in this low accumulation area and the radar sensitivity. Possible causes of these discontinuous layers are not addressed in this thesis, but have led to discussions with the radar engineers in CReSIS.

While picking internal layers, the Picker stores the picked points in a file. After completing the internal layer picking of interesting frames, the picked layer can be extracted from the main processer using a Matlab function "ops_create_posting"[4]. This function returns all of the picked layer data from the selected segment. The extracted layer data structure is shown in **Figure 2.7**. Each frame has an independent Matlab format file. This file contains the basic information of the frame ("Surface", "Time", "Longitude", "Latitude", etc.) and the "layerData" that is manually picked. Each cell in the "layerData" is a layer, and for my case, the 34 cells include the snow surface and 33 internal layers that I picked. The cell contains "longitude", "latitude", "elevation", and most importantly "twtt" (TWTT) for each picked point along a given internal layer. The TWTT is later used to derive the layer depth and the snow accumulation water-equivalent.

[4] Author: Kyle W. Purdon

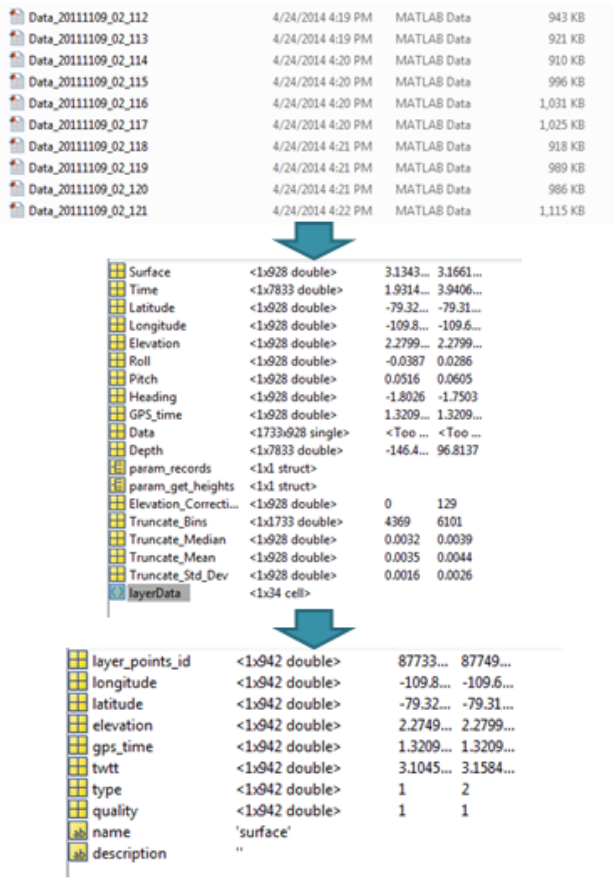

Figure 2.7 Extracted layer Matlab data structure.

2.3.2 Retrieving Snow Accumulation Rate from Radar Data Using TWTT

This research uses the Snow Water Equivalent (SWE) as the internal layer derived annual snow accumulation rate measurement. It is the amount of water contained between internal layers and can be understood as an equivalent depth of liquid water. Obtaining SWE data from the layer data are realized by converting TWTT to layer depth, obtaining a distance between two layers, and converting that distance to SWE. The TWTT and the corresponding depth are connected by the radar signal speed. The product of the one-way travel time to an internal layer and the speed of radar signal along its path gives

the distance of that layer from the radar antennas. Subtracting the distance to the snow surface from the radar antenna gives the depth of the internal layer in the snow. The signal speed is mainly determined by the complex dielectric constant (ε), which is related to snow/ice density, frequency of the radar signal, and other ice properties.

The correlation between complex dielectric constant, snow/ice properties, and radar characteristics is complicated. For this research, the calculation of complex dielectric constant is simplified to only consider the vertical density profile of the snow/ice. This approximation is reasonable, because the research focuses on the shallow layers, whose complex dielectric constant are governed primarily by density changes with depth (Fujita and Mae, 1994; Fujita et al., 1999; Fujita et al., 2000; Tiuri et al., 1984).

The behavior of the complex dielectric constant varies by radar frequency, and a compilation of related studies is given by Warren (1984).The Snow Radar operates at frequencies between 2 GHz to 6 GHz. Hence the complex dielectric constant formula is adopted from Tiuri et al. (1984), Matzler et al. (1987) and Matsuoka et al. (1996). The real part of ε is given by Tiuri et al. (1984) as:

$$\varepsilon' = 1 + 1.7 \cdot den + 0.7 \cdot den^2, \tag{2.1}$$

where *den* is density of snow/ice. Therefore, for a given density (den), its dielectric constant is given by:

$$\varepsilon = \varepsilon_0 \cdot \frac{1+1.7 \cdot den+0.7 \cdot den^2}{1+1.7 \cdot den_0+0.7 \cdot {den_0}^2}, \tag{2.2}$$

where ε_0 is the complex dielectric constant of ice ($\varepsilon_0 = 3.15$); and den_0 is the density of ice ($den_0 = 0.917\ \mathrm{g}/cm^3$).

With the derived complex dielectric constant profile, the speed of the radar signal can be obtained as it propagates into the snow. While the speed of radar signal is constant ($3\times10^8\ m/s$) in a vacuum, it decreases as it propagates through different materials. For each complex dielectric constant, there is a corresponding propagation constant (γ); the imaginary part of the propagation constant determines the speed of radar signal. The propagation constant for a given material is defined by the ratio of the amplitude at the source of the wave to the amplitude at some distance x ($\frac{A_0}{A_x} = e^{\gamma x}$). It is a complex number because the sinusoid phase of the wave varies with distance. The propagation constant can be expressed as below:

$$\gamma = \alpha + j \cdot \beta = j \cdot \sqrt{-j \cdot 2\pi \cdot f \cdot u0 \cdot (j \cdot 2\pi \cdot f \cdot \varepsilon \cdot e0))}, \tag{2.3}$$

in this function, α is the real part of propagation constant (γ), called the attenuation constant; j is the imaginary symbol; β is the phase constant, imaginary part of propagation constant (γ); f (Hz) is the radar frequency and for Snow Radar f is set to be $5 \cdot 10^9$ Hz, the middle frequency in its bandwidth; $u0 = 4 \cdot 10^{-7} \cdot \pi\ (N \cdot A^{-2})$ is the permeability of free-space; ε is the dielectric constant; $e0 = 8.85 \cdot 10^{-12}(F/m)$ is the permittivity of free-space.

The imaginary part of propagation constant is called the phase constant (β, rad/m), representing the change in phase per meter along the path travelled by the wave at any instant:

$$\beta = imag(\gamma), \tag{2.4}$$

wave length (λ) of the electromagnetic wave is given by:

$$\lambda = 2\pi/\beta, \tag{2.5}$$

finally, the wave speed (v) is:

$$v = f \cdot \lambda, \tag{2.6}$$

and distance between two internal layers detected at *twtt1* and *twtt2* (thickness) is:

$$thickness = (twtt1 - twtt2)/2 \cdot v; \tag{2.7}$$

2.3.3 Deriving Snow Accumulation Rate

According to the last section, the speed of the radar signal in each internal layer is primarily based on a density profile. These data can be obtained by extracting an ice core and obtaining snow density of core segments from the mass and volume of the individual core segments. Using the depth of each core segment, a vertical density profile can be constructed. As previously mentioned, density profiles from the three ice cores are available within the study area of this research. Since the study area is large, the distance between flight line segments and ice core locations can be very large. To test the sensitivity of this on the results, I calculated the Snow Radar SWE using different density profiles. Based on these

results, I developed a procedure for choosing ice core density profiles, which will be explained in section **3.1.2, Optimal Density Profiles**.

The actual calculation of SWE from the extracted layer data from the Picker is realized using interpolation. With the ice core density profile, the radar signal speed along the ice core depth profile can be calculated from the complex dielectric constant and propagation constant. A TWTT profile is inversely calculated using the principles introduced above for the ice core annual layer depth profile. This relates an exact TWTT with a depth. The depth of the picked internal layers is then obtained by interpolating the ice core depth according to the two TWTT profiles: the ice core derived one and the Snow Radar measured one. This processing method is illustrated in **Figure 2.8**, which shows the relationship between the ice core density profile, the inversely derived ice core TWTT profile, and the Snow Radar layers TWTT profile.

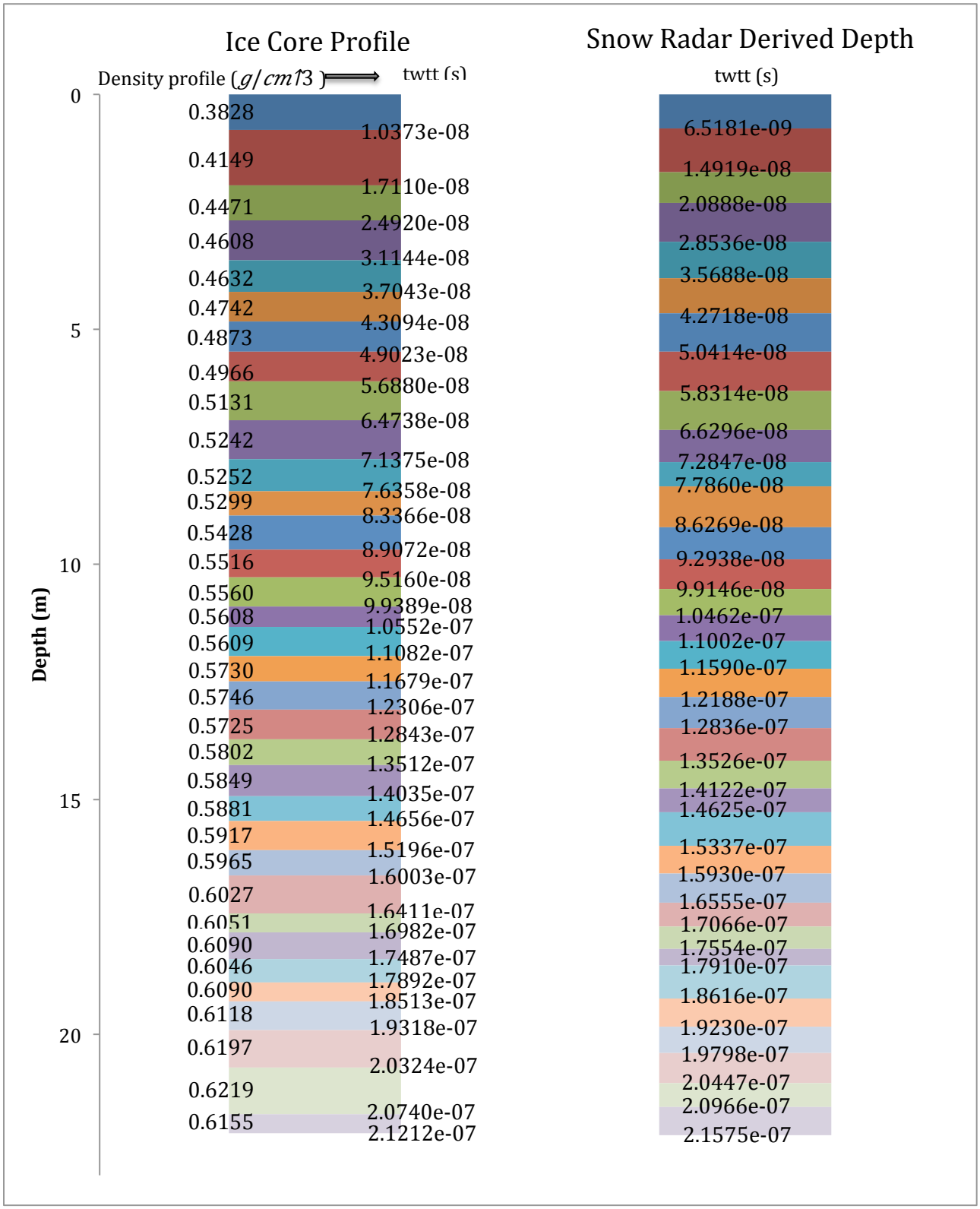

Figure 2.8 Process of retrieving SWE from ice core profiles (ITASE-01-3).

2.4 Regional Climate Model Data

An approach to obtain the ice accumulation rate over a large area is to use a regional atmospheric climate model (RACMO). The model estimates the input (precipitation) and inland output (surface sublimation, meltwater runoff, erosion by drifting snow, and sublimation of drifting snow) of ice over WAIS, providing the net snow accumulation rate. The RACMO2.1/ANT climate model has been studied in several papers, and is favored for its comprehensive consideration of different ways of inland ice loss (Lenaerts et al., 2012a; Rignot et al., 2008). Continuous improvements have been applied to the RACMO2.1/ANT model to obtain better agreement between the simulations and observations. In a newly revised RACMO2.1/ANT, the basic snow accumulation rate estimation is calculated using the formula below (Lenaerts et al., 2012b):

$$SMB = \int_{year}(P - SU_s - RU - ER_{ds} - SU_{ds})dt; \tag{2.8}$$

where SMB stands for surface mass balance, which is a same concept with snow accumulation; P is precipitation; SU_s is surface sublimation; RU is runoff due to melt; ER_{ds} is erosion by drifting snow; and SU_{ds} is sublimation of drifting snow.

The new implementation of Lenaerts' RACMO2.1/ANT model comes from the fact that it couples a drifting snow routine to RACMO2.1/ANT, which is ignored by former versions of the model because of the difficulty of modeling drifting snow. The data from this new RACMO2.1/ANT model agrees well with in situ observations (Lenaerts et al., 2012b). A map of the average annual accumulation from the

RACMO2.1/ANT data is shown in **Figure 2.9**. The comparison among different models: Merra, ERA-Interim, ERA-40, RACMO2.1/ANT, and Polar MM5, shows noticeable consistency (Burgener et al., 2013).

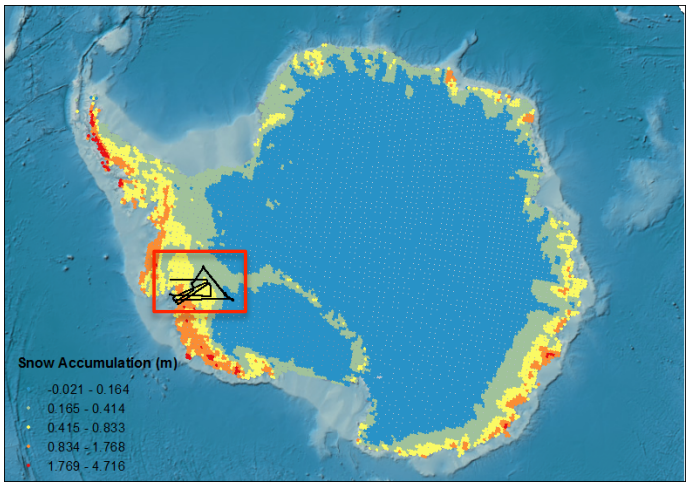

Figure 2.9 Average annual snow accumulation rate (1979-2012) from the RACMO2.1/ANT model (the red box shows the study arae).

2.5 AWS and SIE Data

The entire Byrd Station AWS temperature and atmospheric pressure dataset has been examined for incomplete and missing data. This analysis has found that missing data may exist for a whole month or for just a few hours. The distribution of missing data is thus variable. The downloaded AWS data were organized by year, such that each year has a Matlab variable containing four columns representing temperature, pressure, wind speed, and wind direction. For this research, if more than two thirds of the observations for a given months were missing, the entire month was categorized as missing. A year with four or more missing months is considered to be missing. Thus, missing temperature data was assigned

to ten years, and missing pressure data was assigned to ten years (**Figure 2.10**). For the sea ice (SIE) data, the time series is mostly complete, with only 41 missing days occurring from 11/3/ 1987 to 1/12/1988.

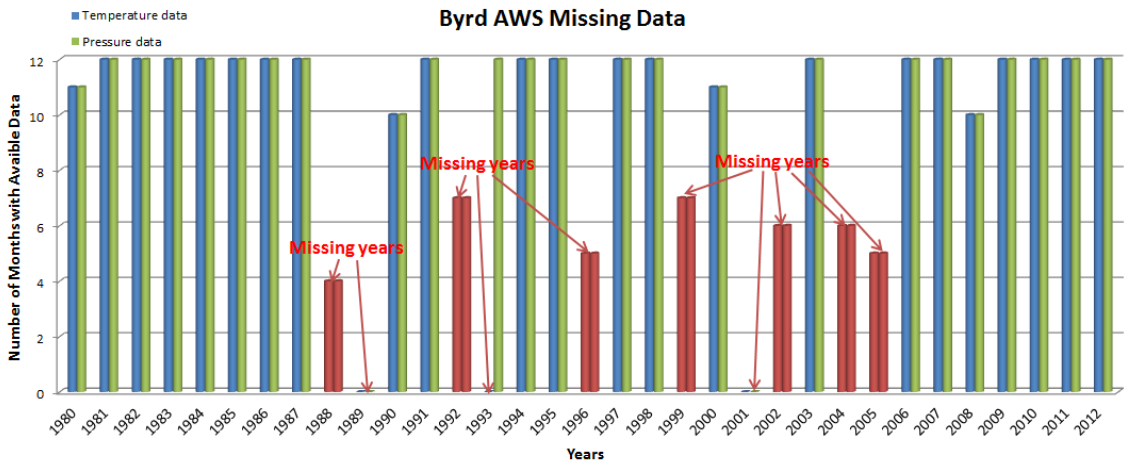

Figure 2.10 Byrd AWS Missing Data.

After tagging the missing AWS and SIE data, the next step was to unify the weather station, SIE, and Snow Radar data. One concern in considering three datasets is their varying temporal resolution, which is a strictly required feature to build them into one dataset. The Snow Radar data has the coarsest temporal resolution (yearly). On the other hand, AWS data are provided at 3 hour intervals and SIE data are provided daily. To make them unified, the weather variable and sea ice data should be downscaled to yearly. A representative factor is needed for every year for both AWS and SIE data.

For the AWS data, the approach of examining weather extremes was taken, since extreme weather conditions partly reflect the climate change and may be a possibility for the rapid ice mass loss in WA considered in this research. Examining the values at tails of the annual distributions (e.g. 5th and 95th

percentile) was undertaken. Similar statistics of extremes are widely used to quantify how often and how intense extremes happened each year (Feldl and Roe, 2011; Gershunov, 1998; Sen Roy and Balling, 2004). In the case of SIE, the maximum, median, and minimum values can reflect the sea ice formation processes for that year. The parameters for weather and SIE condition are plotted in **Figure 2.11** and **Figure 2.12**. The break points in **Figure 2.11** are caused by the missing data.

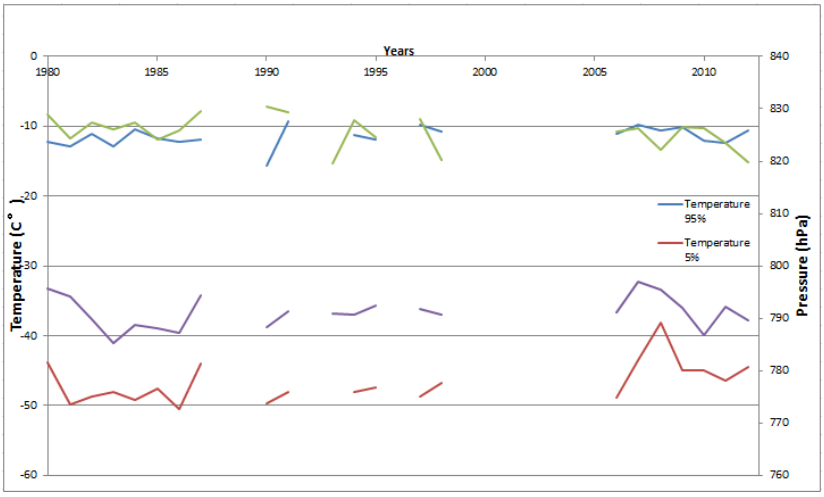

Figure 2.11 Temperature and pressure values at 95% and 5% (Byrd AWS).

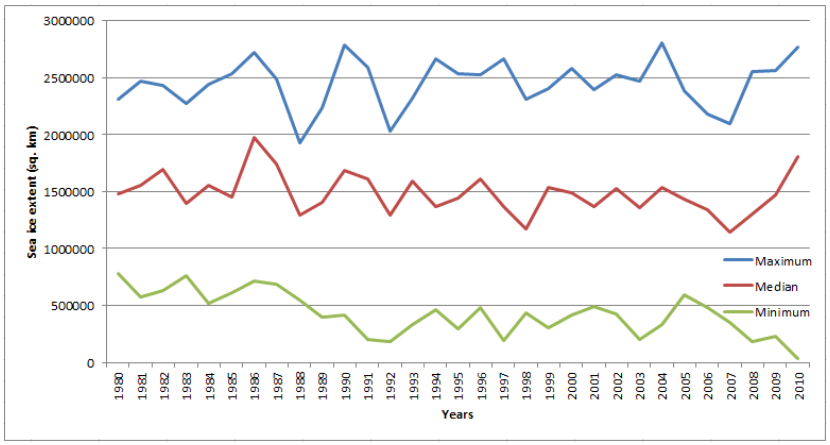

Figure 2.12 Bellingshausen and Amundsen seas sector (60°W–120°W) annual maximum, median, and minimum SIE.

3 Research Methods and Uncertainty Analysis

3.1 Measurement Errors in Picking

Besides the instrument measurement uncertainty of the Snow Radar data and initial signal processing, analysis errors occurs during layer picking. In this study, internal layers are obtained through manual picking, which is a moderately subjective process. The resulting internal layer depths obtained depend to a certain degree on the judgment of the person who is picking them. Fortunately, an experienced "picker" should have a consistent picking accuracy and if repeatedly picking the same echogram, the differences between the datasets should be small and consistent. The results from repeated picking on the same Snow Radar dataset provide a way to quantify the uncertainty in the analysis step we call picking.

3.1.1 Classical Additive Measurement Error Model

In this research, I am the only "picker" and the subject in testing the measurement error in picking. As the subject of this research, I did not deliberately over or under estimate the depth of the layers I see in

the radar echogram. Thus, the picking process is an unbiased measurement of the depth of radar reflector. Under this circumstance, the measurement error in picking has zero mean conditional on it, given by:

$$E(U_{ij} \mid X_i) = 0. \tag{3.1}$$

When the measurement error is either independent of the true value of the mismeasured variable or holds zero mean conditional, the classical additive measurement error model (CAMEM) applies (Hu and Schennach, 2008). Further, the CAMEM is usually good with measurements uniquely done by an individual, which can be replicated (Carroll et al., 2012); in this research the picking process is exclusively done by me and can be replicated. Thus, I adopted CAMEM to explain the measurement error in picking. This model explains the correlation between the measurement and true values given by:

$$W_{ij} = X_i + U_{ij}, \tag{3.2}$$

where W_{ij} is *j* th unbiased measure of X_i, and in my case it is *i* th layer in *j* th measure; X_i is the true value for *i* th subject, and in my case it is the true SWE of *i* th annual layer in ice sheet; and U_{ij} is the measurement error for *i* th subject in *j* th measure, and in my case is the measurement error in picking for *i* th layer in *j* th picking.

In CAMEM, the measured value is the true value adding measurement error. Naturally, the measured values (W_{ij}) have a larger variance than the true values (X_i):

$$\sigma^2_{W_{ij}} = \sigma^2_{X_i} + \sigma^2_{U_{ij}}. \quad (3.3)$$

3.1.2 Distribution of Measurement Error in Picking

Another common property of CAMEM is that the measurement error is approximately normal distributed with constant variance (Carroll et al., 2012), which can be expressed as $U_{ij}|X_i \sim Normal\ (0, \sigma_u^2)$. Such distribution of measurement error can be tested by graphical devices based on repeated measurements (Carroll et al., 2012):

(1) Plot the sample standard deviation of the W_{ij} values for an individual against her/his sample mean, call it $\overline{W_{ij}}$. If there are no obvious trends, this suggests that the measurement error variance does not depend on X_i.

(2) Form the differences between replications within an individual, and then form a normal q-q plot of these differences across individuals. If the normal q-q plot shows no evidence of non-normality, this suggests that the measurement errors are also roughly normally distributed.

In order to test whether measurement error in picking fits the common measurement error distribution in CAMEM, I performed the above two graphical devices on repeated picking data. Due to the large number of Snow Radar data used in my analysis, a subset of data frames was used in this analysis. It is assumed that measurement error in picking is consistent for an experienced picker regardless of the amount of data. For this analysis, I choose four uniformly distributed locations along 20111109_02

segment (**Figure 3.1**), with mean annual SWE falling into low, median, and high SWE categories. Specifically, the four locations are frame groups 112 – 113, 141 – 142, 171 – 172, and 194 – 195; the mean annual snow accumulation for these four locations are 0.3546 m, 0.4118 m, 0.3934 m, and 0.2316 m, respectively.

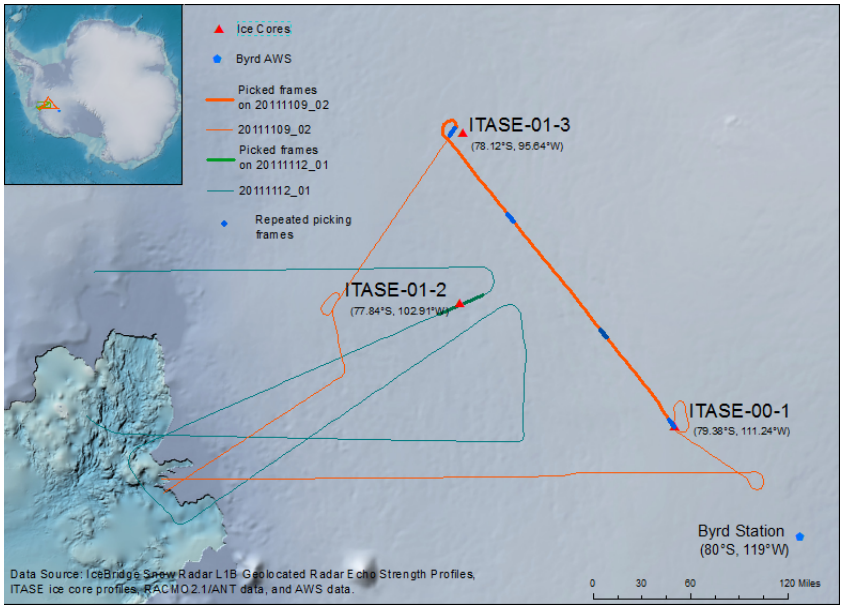

Figure 3.1 Testing frames for picking error.

The judgment on the plot of standard deviation of the W_{ij} values for an individual against her/his sample mean depends on whether a confident regression line exists in the plot. R square (R-sq) and F-ratio as two widely used values in the evaluation of a regression model are used in this test. R-sq is the square of the correlation coefficient R. It is the fraction of the variation in dependent variable that is explained by the regression. Hence, a higher R-sq value indicates a better confidence in the regression slope. F-ratio evaluates the variation of the dependent variable around the regression line, reflecting how well the dependent and independent variables interact. It tests for null hypothesis that

R-sq is equal to zero, meaning no correlation exists between the two variables. F-ratio is the ratio of mean square (MS) of regression to mean square (MS) of residual:

$$F = \frac{MS_{regression}}{MS_{residual}}. \tag{3.4}$$

The MS are computed by taking the sum of squares (SS) and dividing by the corresponding degrees of freedom (DF). DF for regression is equal to the number of independent variables in the model, and in my case is equal to one, for the only independent variable (sample mean ($\overline{W_{ij}}$)). DF for residual is equal to the total number of cases used in the regression minus the number of independent variables plus one. Thus, in my study, DF for the residual is equal to the total number of picked layers from the four frame groups (132) minus the number of independent variables (1) plus one, which gives 130 DF for residual.

To find out whether the obtained F-ratio is significant to reject the null hypothesis, I used the Table of critical values for the F distribution from NIST/SEMTECH Engineering Statistics Handbook (Filliben, 2002). Only when the F-ratio is larger than the given critical value, can the null hypothesis be rejected. Five repeated pickings at four frame groups provide twenty SWE series, which is the measurement (W_{ij}). Arranged by picking numbers, the twenty SWE series contain 132 records, that each record is five SWE values of a certain layer from five pickings. The standard deviation of every record are calculated and plotted against their respective mean (**Figure 3.2**).

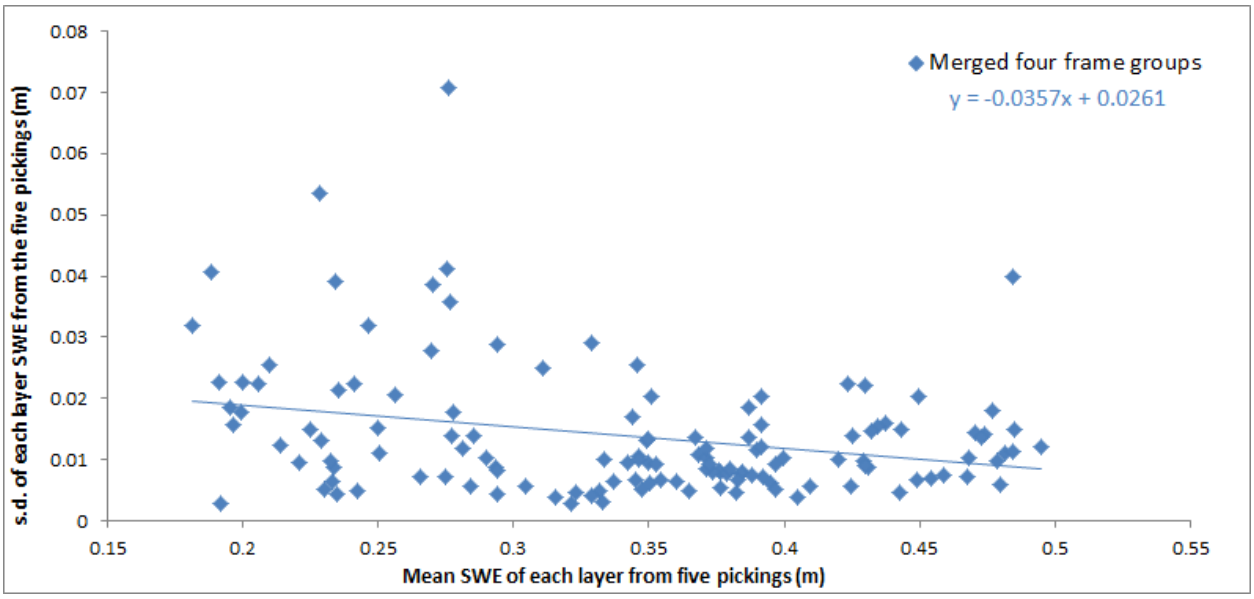

Figure 3.2 Plot of the within-individual standard deviation versus mean of SWE (merged four frame groups).

In **Figure 3.2**, a slightly negative linear regression slope is found, indicating the potential measurement error variance dependency on $\overline{W_{ij}}$ and X_i. The resulting R-sq, F-ratio, and significant level are 0.082, 11.636 and 0.00086. The significant level is smaller than 0.01, meaning that there is more than 99% possibility that the standard deviation of SWE series relates to their respective mean. Thus, the chances are greater than 99% that the measurement error variance correlates with the true value of the subject. The first linear regression coefficient is -0.036, suggesting a slightly negative correlation. This result is reasonable, since low SWE regions have reflectors that are closer together, which can increase the difficulty in picking. With the same radar resolution, a thinner snow layer tends to be more difficult to track than a thicker layer, and hence produce larger measurement error variance. The relation between measurement error variance and SWE is important in planning future surveys using the Snow Radar. By using known or modeled SWE for the survey region, analysis uncertainty can be assessed to determine if

the goals of the experiment are likely to be met. An analysis of the measurement error variance dependency on SWE is discussed further in **4.2 Snow Radar Annual Layer Detection Limit**.

The dependence of measurement error variance on SWE violates the assumption of a constant measurement error variance across the survey domain, and precludes the calculation of the measurement error variance from equation (3.3). Thus, I further tested the four frame groups separately, in order to obtain constant measurement error variance within each frame group. In these separate frame group cases, the significance level of the linear regression between the standard deviation and mean is no longer smaller than 0.05, hence the linear regression is statistically insignificant and measurement error variance can be considered as independent of SWE value. **Figure 3.3** shows the linear regression lines for each frame group.

In the merged frame group the maximum difference in annual SWE is as large as 0.314 m and within the individual frame groups the maximum difference in annual SWE is < 0.2 m. Although measurement error variance increases as annual SWE decreases, it can be considered nearly constant in the individual frame group where the variation in annual SWE is small. This fact permits the calculation of measurement error variance within each frame group, where the range of mean annual SWE is normally smaller than 0.2 m.

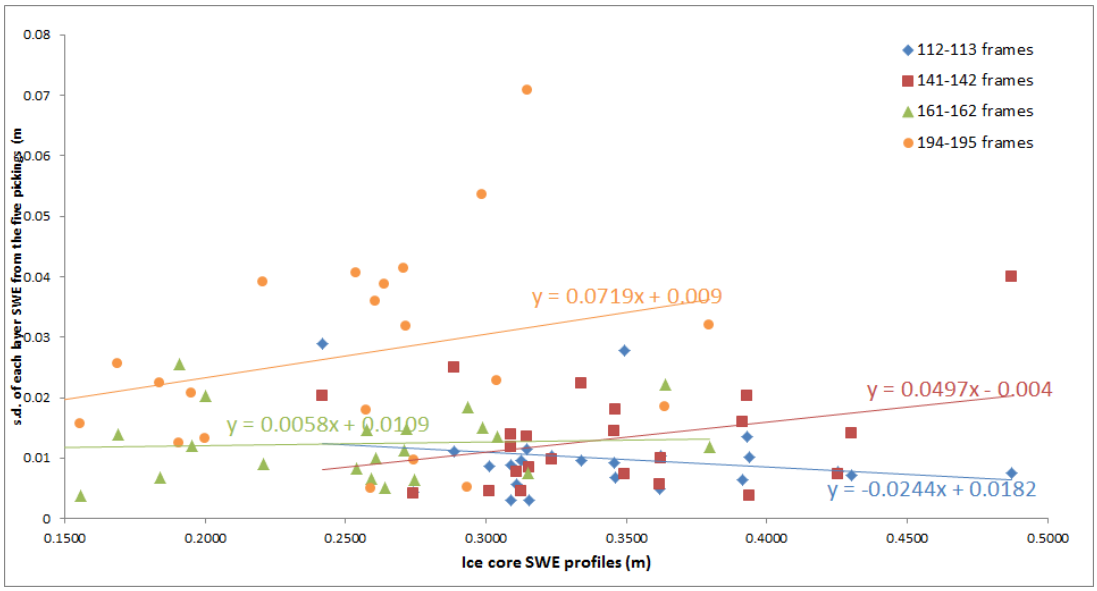

Figure 3.3 Plot of the within-individual standard deviation versus mean of SWE (four frame groups separately).

The second analysis method, q-q plot, is a graphical method for comparing two probability distributions by plotting their quantiles against each other. A normal q-q plot is used to evaluate how well the distribution of a dataset matches a standard normal (Gaussian) distribution. If the shape of normal q-q plot is close to y=x, it can be concluded that the test data has a roughly normal distribution. I made normal q-q plots of the differences between replications both for the merged one frame group and the separated four frame groups. The five normal q-q plots are all close to y=x, implying the differences between five repeated layer pickings approximately follow a normal distribution. This finding proves that the measurement errors in picking are roughly normally distributed. Only the normal q-q plot for the merged frame group is shown in **Figure 3.4**.

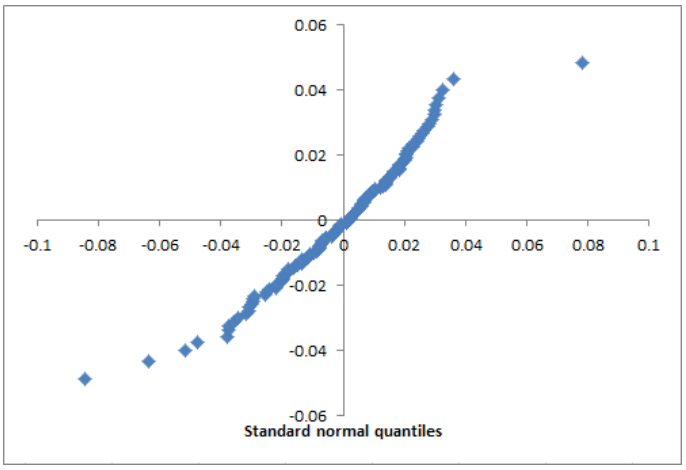

Figure 3.4 Normal q-q plot of the differences in layer SWE between five repeated layer pickings.

3.1.3 Size of Measurement Error

The above analysis methods further confirm that the picking error fits CAMEM. The measurement error variance, though it changes over a large area due to the variation in SWE, within each of the four locations it is constant and follows equation (3.3). Thus the measurement error variance can be given as:

$$\sigma_{U_{ij}}^2 = \sigma_{W_{ij}}^2 - \sigma_{X_i}^2. \tag{3.5}$$

In this study, $\sigma_{W_{ij}}^2$ is the variance of five different pickings. The $\sigma_{X_i}^2$ can not be directly obtained for each layer, otherwise we would not need Snow Radar to get the W_{ij} for ice sheet study. But because of the analysis above proves that X_i and U_{ij} are independent and $\sigma_{U_{ij}}^2$ is constant when the variation in SWE is no more than 0.2 m, the following equation holds (Divers et al., 2011):

$$Cov\left(W_{ij}, W_{il}\right) = Cov\left(X_i, X_i\right) = Var\left(X_i\right) = \sigma_{X_i}^2. \tag{3.6}$$

where *Cov ()* is the covariance sign, and *Var()* is the variance sign. Equation (3.6) implies that the admixture proportion estimates computed on the *j* th and *l* th subsets are both measuring the same underlying latent variable (Divers et al., 2011), which in my case is the true SWE. For the lack of an official covariance concept adopted to n-variabile, I approximated $\sigma_{X_i}^2$ to the mean covariances among five repeated layer pickings $(Mean\ (Cov\ (W_{i1}, W_{i2}), Cov\ (W_{i1}, W_{i3}) \ldots, Cov\ (W_{i4}, W_{i5}))$. The resulting $\sigma_{W_{ij}}^2$, $\sigma_{X_i}^2$, and $\sigma_{U_{ij}}^2$ for the four frame groups are shown in **Table 3-1**. The calculated σ_{u}^2 is considerably small in all the regions and is about one order of magnitude smaller than $\sigma_{\mathrm{X_i}}^2$, which means that the variation caused by measurement error is much smaller than the variation in true SWE values. Thus, the measurement error in picking can be neglected. Further, the mean measurement error variance of these four frame groups is 3.0e-4 m, which gives a standard deviation of 0.017 m. This standard deviation value provides a reference threshold to determine whether one factor is significant enough to influence the distribution of SWE. If the standard deviation in SWE due to some changing factor is smaller than that of the measurement error, then this factor can be neglected in SWE distribution study.

Table 3-1 Measurement error variance (m)

	Frames 112-113	**Frames 141-142**	**Frames 161-162**	**Frames 194-195**
$\boldsymbol{\sigma_{W_{ij}}^2}$	0.00278091	0.00395677	0.00297638	0.00185448
$\boldsymbol{\sigma_{X_i}^2}$	0.0026564	0.0037634	0.00282105	0.00111842
$\boldsymbol{\sigma_{U_{ij}}^2}$	0.00012451	0.00019337	0.00015533	0.00073606

3.2 Optimal Density Profiles

Besides the measurement error introduced by picking, an approximation has to be made for the density profile that is used in the Snow Radar signal propagation speed and SWE calculation. When calculating the snow accumulation from the radar TWTT, an approximate density profile is needed to derive the complex dielectric constant, which further governs the radar signal propagation speed and SWE. This density profile serves as an approximation of the local density profile along the flight segment. How close the density profile is with the local ice sheet density profile determines the accuracy of this calculation.

In this study, I have three available ice core density profiles. The four locations that mentioned above (frame 112 – 113, 141 – 142, 171 – 172, and 194 – 195) are chosen to test the impact of using different density profiles to calculate SWE. I separately used different ice core density profiles from the three ice cores to derive the SWE in the four locations. The standard deviation of the results from different density profiles is calculated and shown in **Figure 3.5**. It can be seen that the influence from density profiles towards SWE calculation is very small, based on the small standard deviation between the SWE calculated using different density profiles. Further, the standard deviation by using different density profiles is smaller than the mean standard deviation of measurement error in picking (0.017 m), which illustrates that for the depths investigated in this study, the fluctuation in SWE from the influence of using different density profiles is negligible compared to the measurement error in picking. In light of

this, the choice of density profile becomes less critical, since it has even less influence over SWE than picking.

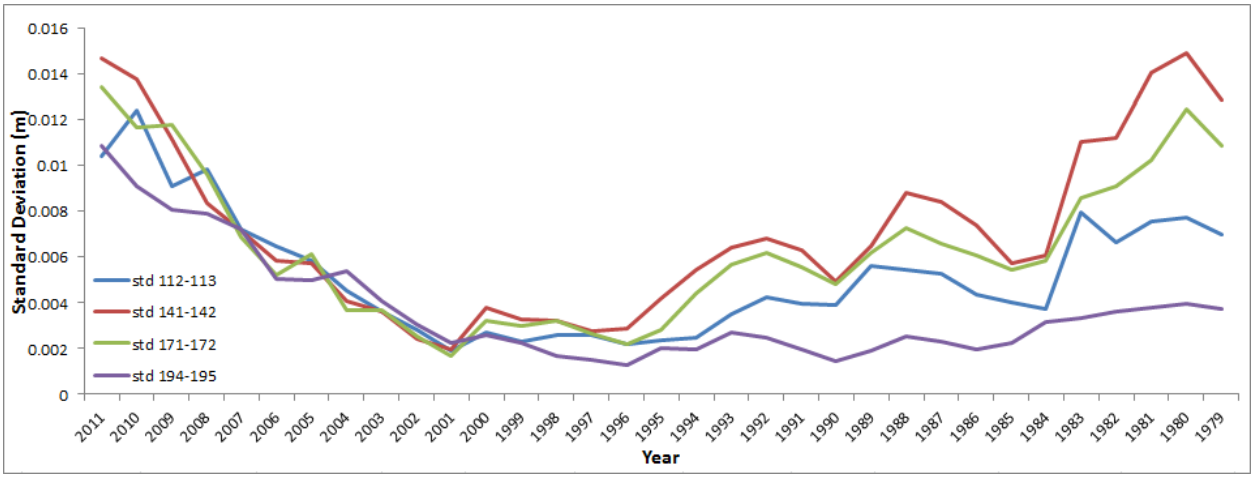

Figure 3.5 Standard deviation of SWE derived from three density profiles.

Based on these results, this study uses the density profile from the nearest ice core to calculate SWE from TWTT. The density profile selected according to this principle holds for an entire frame. The distance between a frame and ice cores is defined as the middle point on that frame to the ice core. According to this rule, frames 112 to 142 use ITASE-01-3 density profile; frames 143 to 169 and frames 291 to 295 use ITASE-01-2 density profile; and frames 170 to 196 use ITASE-00-1 density profile. These relationships are mapped in **Figure 3.6**.

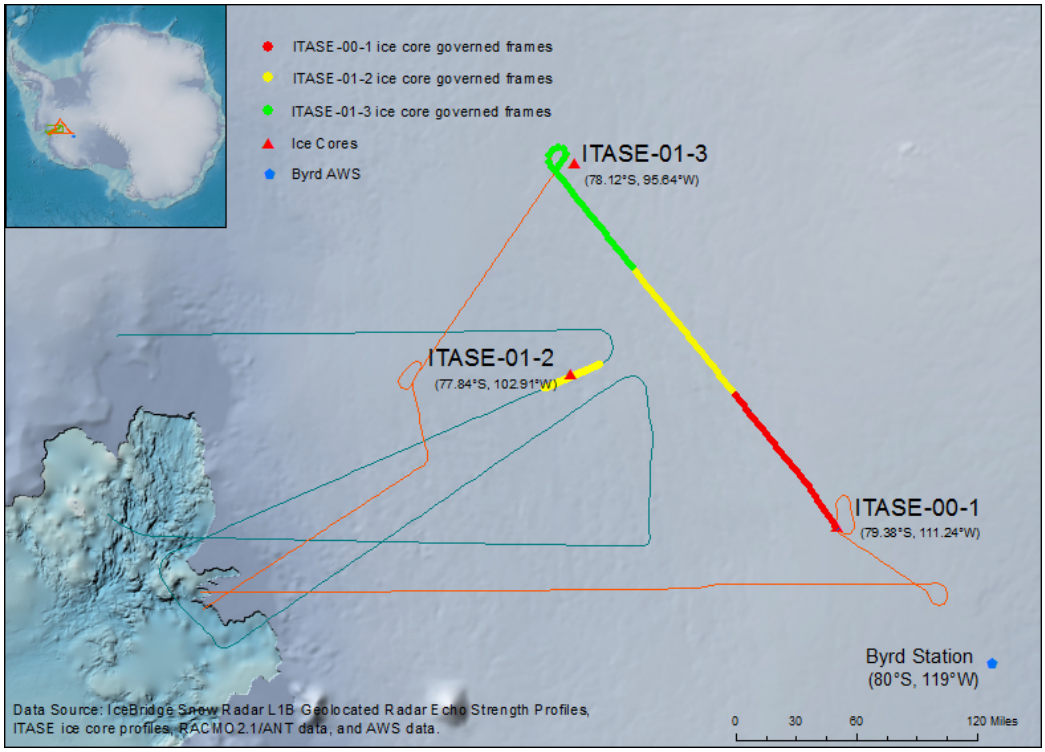

Figure 3.6 Ice core density profiles used for flight segments.

3.3 Snow Radar Chronology Test

As ITASE ice cores and RACMO2.1/ANT data provide annual SWE sequence, they are the two sources for the verification of Snow Radar chronology. This study compares the Snow Radar, ITASE ice core, and RACMO2.1/ANT derived SWE time series to confirm that the internal layers identified in Snow Radar echograms are annual layers as assumed. Their mean and standard deviation are compared. Since SWE from the three datasets have a direct physical connection to each other, the correlation coefficient and p-value are used for a correlation test between these SWE time series. Since the ITASE ice core and RACMO2.1/ANT SWE data are not exactly collocated with the Snow Radar frames, an assumption that the SWE is comparable in different locations has to be made. This assumption is assessed and described

in section **4.2.1 Compatibility of Snow Radar, Ice Core and RACMMO2.1/ANT**. Besides comparison with other datasets, on the accuracy of the derived chronology also can be tested by comparing to dates of strong reflectors to the time of eruption of major volcanic events.

3.4 Mann-Kendall Trend Test

Addressing the second research question, this research tests if there is any predominant long-term trend in snow accumulation within the studied area over the past three decades (1979-2011). The Mann-Kendall trend test is adopted to realize such needs. The Mann-Kendall trend test originated from the rank correlation study, which aims to find the correlation between two different rankings. By substituting one ranking with a time series, the rank correlation becomes a trend test. For a series of numbers that has a negative correlation with the time series, it experiences a decrease with time, and vice versa. In addition, Mann-Kendal trend test is a non-parametric test, meaning that it does not require the data to be normally distributed.

3.4.1 Kendall Tau Coefficient

The rank correlation test for two sets of observations $X = x_1, x_2, \dots, x_n$ and $Y = y_1, y_2, \dots, y_n$ is formulated as follows. The statistic score S is calculated as below:

$$S = \sum_{i<j} a_{ij} b_{ij}, \tag{3.7}$$

where

$$a_{ij} = sign(x_j - x_i) = \begin{cases} 1 \; if \; x_j - x_i > 0 \\ 0 \; if \; x_j - x_i = 0 \\ -1 \; if \; x_j - x_i < 0 \end{cases}, \tag{3.8}$$

and b_{ij} is similarly defined for the observations in *Y*. If the values in *Y* are replaced with the time order of the time series *X, i.e. 1, 2, ..., n,* the test can be used as a trend test. In this case, the statistic *score S* reduces to (Kendall, 1948):

$$S = \sum_{i<j} a_{ij} = \sum_{i<j} sign(x_j - x_i). \tag{3.9}$$

The Kendall tau coefficient is determined by:

$$t = \frac{Actual\ score\ S}{Maximum\ possible\ score\ S} = \frac{S}{\frac{1}{2}n(n-1)}, \tag{3.10}$$

where the maximum possible *score S* occurs when the series of numbers is continuously increasing, indicating a perfect positive correlation between the series of numbers and the time series. Thus, according to the three properties of Kendall tau coefficient (*t*) (Kendall, 1948), when replacing one of the rankings with a time series, the values of *t* should indicate the trend as follows:

(1) if the agreement between the observation and time series is perfect, i.e. every observation has the same rank with the time series, *t* should be +1;

(2) if the disagreement between the observation and time series is perfect, i.e. every observation has the inverse rank with the time series, *t* should be -1;

(3) for other arrangements t should lie between these limiting values; and in some acceptable sense increasing values from -1 to 1 should correspond to increasing agreement between the observation and the time series.

3.4.2 Test of Significance

Given a value of *S* or Kendall tau coefficient, it is also important to know the reliability of the observed trend (significant level). Such evaluation is done by the analysis of the frequency distribution of *S*. Assumed that for a series of numbers with *n* observations, the number of possible rankings is *n!*, the possibilities of all *n!* rankings are equally probable, the shape of the frequency polygon tends to that of the normal curve (Kendall, 1948). Thus the frequency distribution of the *S* for any observation can be derived, only knowing the number of observations (*n*). With this assumption, the expected mean (*E*) and variance (*var*) of *S* are given by(Kendall, 1948):

$$E(S) = 0, \tag{3.11}$$

$$var(S) = \frac{1}{18} n(n-1)(2n+5). \tag{3.12}$$

For a normal distribution, an *S* value for a certain ranking would have a z-value:

$$Z = \frac{S-E(S)}{\sqrt{var(S)}} = \frac{S}{\sqrt{var(S)}}. \quad (3.13)$$

From this z-value, a probability p-value of *S* can be derived from the normal distribution using a z-value to p-value formula(Yue et al., 2002):

$$P = \frac{1}{\sqrt{2\pi}} \int_{-\infty}^{Z} e^{-\frac{t^2}{2}} dt. \quad (3.14)$$

3.4.3 Modified Mann-Kendall Trend Test for Auto-correlated Data

The original Mann-Kendall trend test is based on an assumption that the data are serially independent, which may not be the fact, especially in hydrological and climatic dataset that often are auto-correlated. Under the influences from seasonality or longer climatic cycles, like El Niño and La Niña, hydrological and climatic dataset may repeat some trend within its whole time series. Snow accumulation series also has such an issue. Two types of solutions accounting for the effect from autocorrelation on the trend test are proposed: pre-whitening and variance correction approaches (Yue et al., 2002). Pre-whitening method, as its name implies, aims to remove the auto-correlation part directly in data before the trend test (Kulkarni and von Storch, 1995). The auto-correlation used in pre-whitening could be derived from various models, including auto-regression model and moving average model (Hamed and Ramachandra Rao, 1998). Variance correction, on the other hand, tries to account for the underestimation/overestimation in the variance of *S* separately due to a positive auto-correlation/negative auto-correlation (Hamed and Ramachandra Rao, 1998).

Yue et al. has tested the effectiveness of both pre-whiting and variance correction approaches and brought them into question: pre-whiting removes part of the magnitude of the trend compared with the true one and variance correction cannot properly correct the influence of the presence of autocorrelation on the Mann-Kendall trend test (Yue et al., 2002). In order to obtaining a reliable solution for eliminating the autocorrelation effect on the trend test, Yue et al proposed a trend-free pre-whitening (TFPW) procedure. The TFPW Mann-Kendall trend test has been used and tested by a many researchers, from which its accuracy has been proved (Danneberg, 2012; Gao et al., 2011; Rivard and Vigneault, 2009). This study also adopted this method to analyze the trend in snow accumulation. The TFPW Mann-Kendall method has a four-step procedure (Yue et al., 2002):

(1) Remove the series trend using the Thiel–Sen Approach (TSA):

$$Y_t = X_t - bt. \tag{3.15}$$

(2) Remove the correlation using the lag-1 autocorrelation coefficient (r_1):

$$Y'_t = Y_t - r_1 Y_{t-1}. \tag{3.16}$$

(3) Put back the slope in the series:

$$Y''_t = Y'_t + bt. \tag{3.17}$$

(4) Apply the non-parametric Mann–Kendall test to the modified series (of step 3).

In this procedure, the TSA is an estimated slope of a trend and is given by (Sen, 1968; Theil, 1992):

$$b = median\left(\frac{X_j - X_l}{j-l}\right) \ \forall l < j, \tag{3.18}$$

where *b* is the estimate of the slope of the trend and X_l is the *l* th observation; and *median()* is the median value in one series.

The lag-1 auto correlation coefficient is given by (Kulkarni and von Storch, 1995):

$$r_1 = \frac{\sum_{t=2}^{T} X_t X_{t-1}}{\sum_{t=1}^{T} X_t^2}, \tag{3.19}$$

where X_t is the *t* th observation.

3.5 Wilcoxon Rank Sum Test

This study also unites SWE, AWS, and SIE data to find if there is a traceable relation between the three of them. The Wilcoxon rank sum test is used to determine whether such relation exists. This test is an alternative for the t-test, but it works better for small size datasets and does not require the data to be normally distributed, like the t-test. The Wilcoxon rank sum test is based solely on the order in which the observations from the two samples fall, and compares two samples to assess whether their population mean ranks differ.

Specifically, suppose two samples x_1 and x_2 both have N records, which give N pairs. Calculate $|x_{2,i} - x_{1,i}|$ and exclude pairs with $\left|x_{2,i} - x_{1,i}\right| = 0$. The remaining pairs number is denoted as N_r.

Starting with one, rank the remaining N_r pairs from smallest absolute difference to largest absolute difference ($|x_{2,i} - x_{1,i}|$) and the rank is denoted as R_i. Then, the test statistic W is given by (Wilcoxon and Wilcox, 1964):

$$W = \sum_{i=1}^{N_r}[sign(x_{2,i} - x_{1,i}) \cdot R_i], \tag{3.20}$$

where $sign(x_{2,i} - x_{1,i})$ follows equation (3.8). When $N_r \geq 10$, a z-score is approximated as below:

$$Z = \frac{W-0.5}{\sigma_W}, \tag{3.21}$$

$$\sigma_W = \sqrt{\frac{N_r(N_r+1)(2N_r+1)}{6}}. \tag{3.22}$$

Then the p-value can be calculated using a Z value through equation (3.14). This test usually gives a logical value h as a result. The result h=1 indicates a rejection of the null hypothesis, and h=0 indicates a failure to reject the null hypothesis at the 5% significance level.

3.6 Snow Radar Derived Snow Accumulation Rates

Using the method stated in **2.3.3 Deriving Snow Accumulation Rate**, I derived snow accumulation rates (1979-2011) in the two sections of Snow Radar flight segments. The results are saved in Matlab files as a matrix. Each frame has depth/ SWE matrixes; the size of these two matrixes is the number of layers (34: surface and 33 picked layers) times the number of picked points in that frame (varying from frame to frame). Rows in depth/ SWE matrix stand for layers and store depth/SWE values for picked

points on the corresponding layer. For the large number of picked points in one frame (~1000), it is impractical to analyze the distribution of the whole matrix. Further, as spatial noise contaminates the spatial distribution of snow accumulation within 1 km, it is unnecessary to analyze the distribution of snow accumulation within 1 km distance. This study thus averages the depth/SWE matrixes over different distances for various applications, e.g. analysis on the snow accumulation temporal trend due to climate change averages the matrixes over ~100 km for the large range climate influences, and analysis on the snow accumulation spatial distribution due to wind redistribution averages the matrixes over 1 km for the small range the wind influences. **Figures 3.7-3.9** show the averaged layer depth over 45 km (approximately 10 frames) against the density profile of the closest ice core.

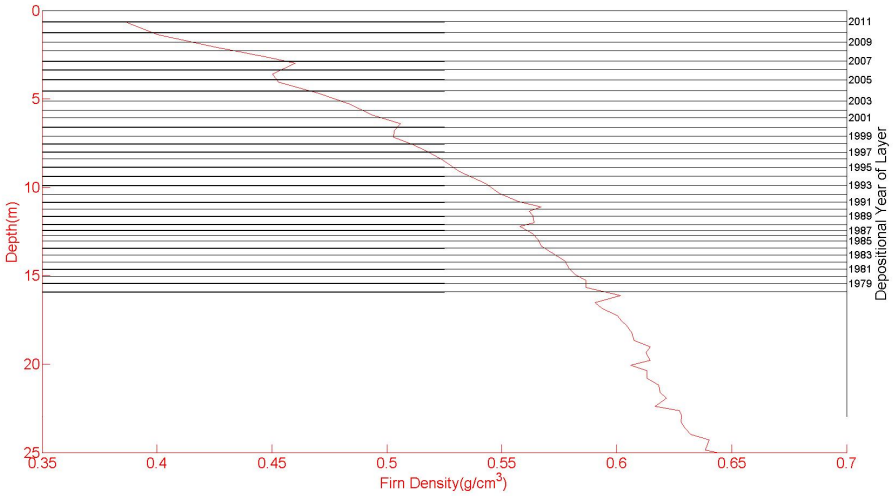

Figure 3.7 Density profile(ITASE-00-1) against mean layer depth derived from Snow Radar(frame 185-196).

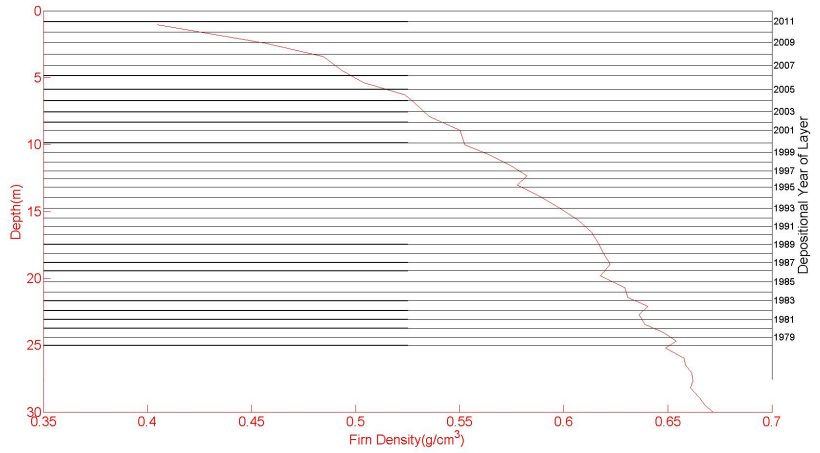

Figure 3.8 Density profile(ITASE-01-2) against mean layer depth derived from Snow Radar(frame 286-295).

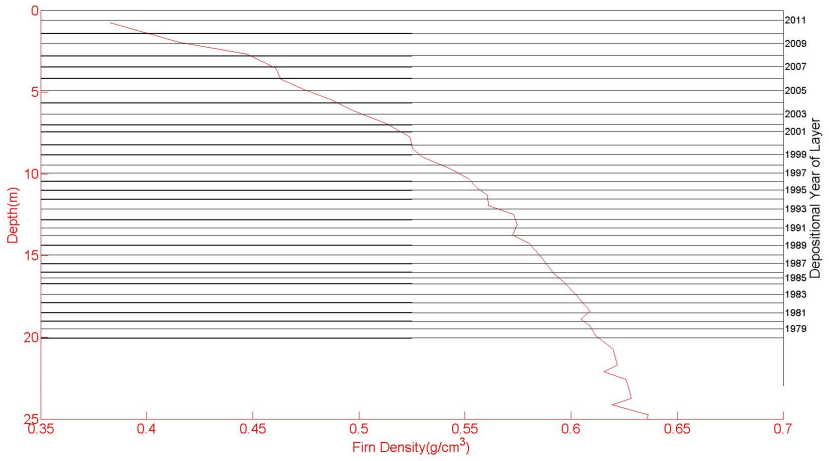

Figure 3.9 Density profile(ITASE-01-3) against mean layer depth derived from Snow Radar(frame 112-131).

From **Figures 3.7-3.9**, it can be observed that the Snow Radar derived snow accumulation has captured a similar spatial pattern in the study area with ice core data: nearby ITASE-00-1 the snow accumulation is low, nearby ITASE-01-2 the snow accumulation is high, and nearby ITASE-01-3 the snow

accumulation is in between. In the same 33-year time span (1979-2011), the 1979 accumulation layer from the Snow Radar reaches 15 m in depth in the frames near ITASE-00-1, compared to a core depth of 15.3 m for 33 years of accumulation. The 1979 Snow Radar layer depth is 25 m in the frames near ITASE-01-2 compared to a core depth of 27.1 m for 33 years of accumulation. And the 1979 Snow Radar layer depth is 20 m in the frames near ITASE-01-3 compared to a core depth of 21.7 m for 33 years of accumulation. This relationship strongly supports the accuracy of annual layer dating of Snow Radar data. Furthermore, it is clear from these figures that the three widely spaced ice cores have density profiles that are very similar to each other.

4 Results and Interpretation

4.1 Chronology of Snow Radar

In order to answer the first research question concerning the accuracy of the derived chronology of Snow Radar detected internal layers, comparisons were made with the ITASE ice core and RACMO2.1/ANT data. If Snow Radar derived SWE series had a close mean, standard deviation, and annual accumulation pattern with ITASE ice core and RACMO2.1/ANT data, this supports the chronology of Snow Radar layers to be annual. Further, I identified strong radar reflection layers caused by volcanic ash deposition, surface melting, or some other process to try to add confidence to the chronology chosen for the internal layers.

4.1.1 Compatibility of Snow Radar, ITASE Ice Core and RACMO2.1/ANT

Snow Radar segments and ITASE ice core locations are generally aligned as the study flight line passed three ice core locations (**Figure 4.1**), apart from ice core ITASE-01-3 that is about 9 km away from the closest point on the Snow Radar flight path. ITASE-00-1 core location is on the 20111109_02 segment

and the ITASE-01-2 core location is on the 20111112_01 segment. The effects from accumulation during the ~10 year (2001/02-2011) gap between the Snow Radar measurements and when the ITASE cores were obtained leads to some uncertainty in the comparison. As RACMO2.1/ANT is a gridded dataset with 27 km resolution (a subset of grid corner points are shown in **Figure 4.1**), this model provides an averaged snow accumulation over a grid cell. The lengths of Snow Radar flight line in each RACMO2.1/ANT grid cell varies from less than 1 km to more than 30 km. Obviously, these facts introduce uncertainty in comparing the three datasets, but counting Snow Radar layers back in time should align the datasets.

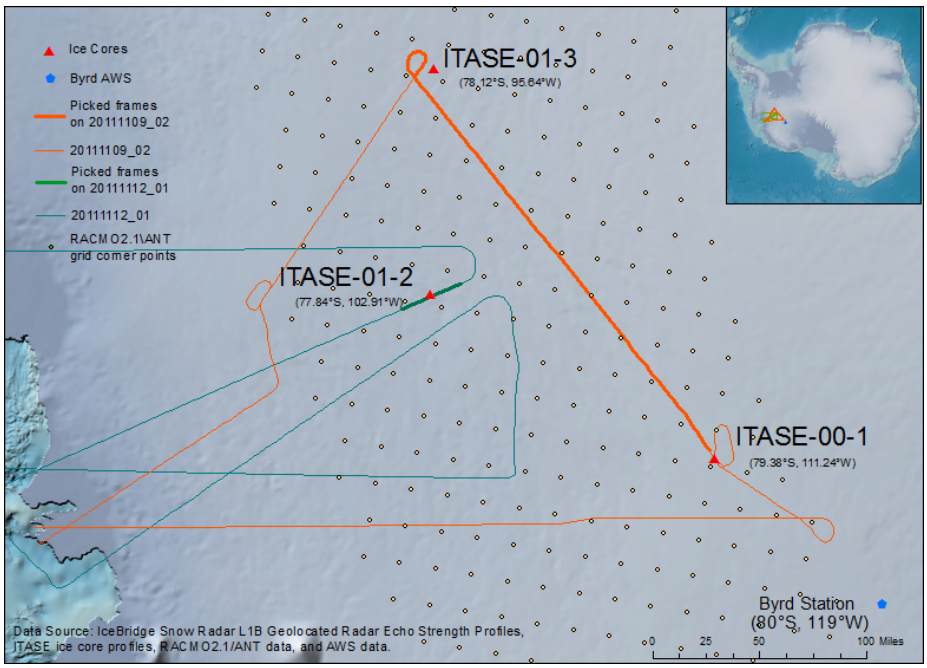

Figure 4.1 Locations of Snow Radar, ice cores, and RACMO2.1/ANT grid corner points.

I analyzed the Snow Radar derived snow accumulation of the 370 km 20111109_02 segment to verify the consistency in snow accumulation series within 20 km along the flight line. The variability in snow

accumulation for each layer is measured by the standard deviation over 40 different lengths from 0.5 km to 20 km, with a 0.5 km interval (e. g. 0.5 km, 1.0 km, … 19.5 km, 20 km). Such an examination provides information on the spatial variability in snow accumulation at different depths. The result is shown in **Figure 4.2**.

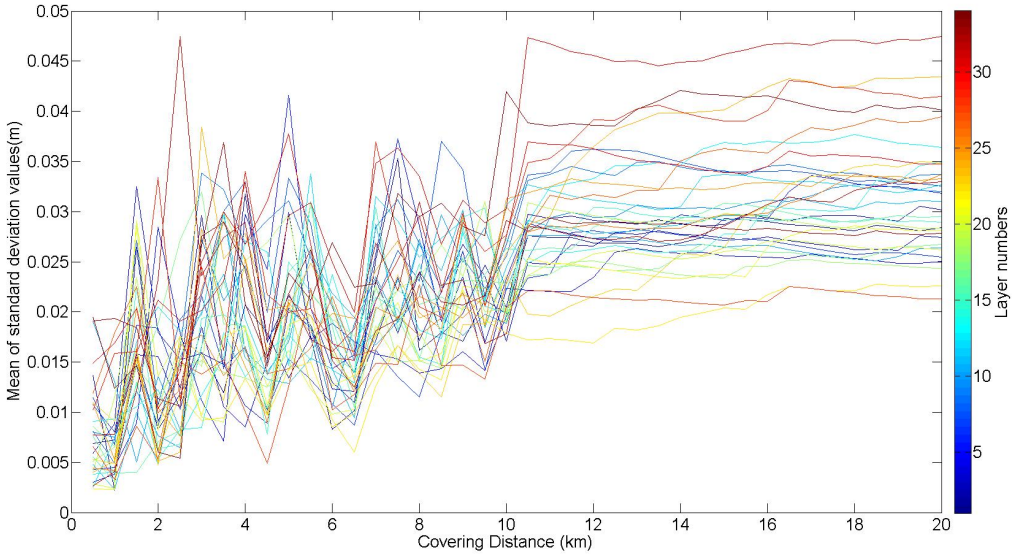

Figure 4.2 Mean standard deviation at different averaging distances.

In **Figure 4.2**, the colors from blue to red represent the layer depth: the blue color represents the shallowest layers (depth of <10 m), and red represents the deepest layers (depth >25 m). The "Covering distance" represents the different lengths along the segment that the standard deviation is calculated over. "Mean standard deviation" represents the mean of the calculated standard deviation over the entire studied frames on the segment. For example, with a "Covering distance" of 0.5 km, the entire segment (370 km) breaks into 740 parts; each is 0.5 km in length. The standard deviation of a certain layer is calculated in all the 740 parts, and the mean of the 740 standard deviations is shown in **Figure 4.2**.

The averaged standard deviation of the 33 layers within 5 km is 0.0164 m, within 10 km it is 0.0186, and within 20 km it is 0.0247. Compared to the threshold given by **3.1.3 Size of Measurement Error** (0.017 m), it can be concluded that within 5 km the spatial variability of snow accumulation is negligible; and when the range increases to 10 km the spatial variability of snow accumulation is a little greater than the fluctuation caused by picking, which may start to introduce noticeable errors due to the difference in the snow accumulation patterns; in the end, when the range reaches 20 km the spatial variability of snow accumulation continues to grow. In other words, locations that are about 5 km apart should correlate with each other very well; locations that are about 10 km apart may start to have noticeable differences and have worse correlation with each other than locations within 5 km; and locations that are about 20 km apart would have even more difference in snow accumulation pattern.

Another factor that needs attention is the anisotropy in snow accumulation spatial distribution. The distance perpendicular to the coast (moisture source) probably affects snow accumulation more than the distance parallel to the coast. With the two flight lines in this study, the change in mean annual accumulation rate per RACMO2.1/ANT grid cell along 20111109_02 (parallel to coast) is approximately 0.0098 m, and along 20111112_01 (perpendicular to coast) it is approximately 0.032 m. This is because the open sea is the main resource of water vapor, the prerequisite of precipitation. The distance perpendicular to the coast has more influences on water vapor transport than the distance parallel to the coast. This pattern can be noticed in **Figure 4.3**, RACMO2.1/ANT derived mean annual SWE (1979-2012), that mean annual SWE has more variability along a distance perpendicularly to the coast than along a similar distance but parallel to the coast. But there are still some big changes when

travelling parallel to the coast, since apart from the water vapor resource the snow accumulation rates depend on other factors, e.g. elevation and surface roughness. This may explain some of the variability seen in the standard deviation for segment lengths up to 10 km.

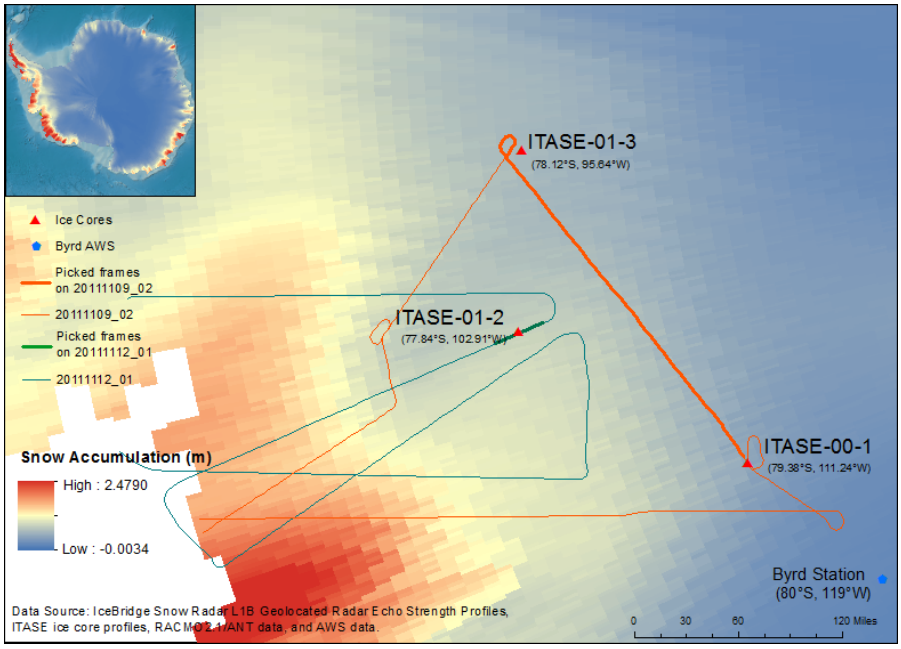

Figure 4.3 Segments on RACMO2.1/ANT derived mean annual SWE (1979-2012) background.

4.1.2 Comparison between Snow Radar and Ice Core

ITASE-00-1 is collected in 2000; while ITASE-01-2 and ITASE-01-3 are collected in 2001. Therefore, 11 and 10 years difference exist correspondingly between ice cores and the Snow Radar data. The comparable time span between ice cores and Snow Radar is their overlapping years: 2000–1979 for ITASE-00-1, and 2001–1979 for ITASE-01-2 and ITASE-01-3. I have more than 94900 picking points on each layer, and it would be confusing and unnecessary to compare all of them separately with three ice cores. Hence, I average SWE series over every frame, and downscaled the Snow Radar SWE series

to 95 frames. The length of each frame is approximately 4.5 km, and according to **4.2.1 Compatibility of Snow Radar, Ice Core and RACMO2.1/ANT**, this distance should maintain consistent snow accumulation distribution. Initially, Snow Radar derived SWE has similar mean and standard deviation values with the ice core profiles through their common 22/23 layers traced from 2000/2001 to 1979 (**Table 7-1**). This provides good evidence that the Snow Radar resolves annual layers.

I plot the SWE series from ITASE ice cores and the average of 10 Snow Radar frames which are closest to the corresponding ice cores (**Figure 4.4-Figure 4.6**). In **Figure 4.4- Figure 4.6**, the red line indicates the ITASE ice core SWE series, the green line indicates the Snow Radar SWE series, and the green error bar on the green line indicates the standard deviation in the averaged 10 frames. These figures show that the SWE series from ITASE-01-3 has the most identical pattern with its nearby Snow Radar frames, the SWE series from ITASE-01-2 also has noticeable similarity with its nearby Snow Radar frames, and the SWE series from ITASE-00-1 has a poor correlation with its nearby Snow Radar frames. In **Figure 4.4**, the two series of snow accumulation from Snow Radar and ice core have the greatest disagreement during the years 1979 to 1984, and the period of 1985 to 1992 which could be due to a miscounted layer in Snow Radar echograms. The correlation could be improved by carefully re-picking, improving the signal processing procedure, or in the future, using a Snow radar system with higher resolution. The Snow Radar frames near ITASE-01-2 have the largest spatial variability for its largest standard deviation.

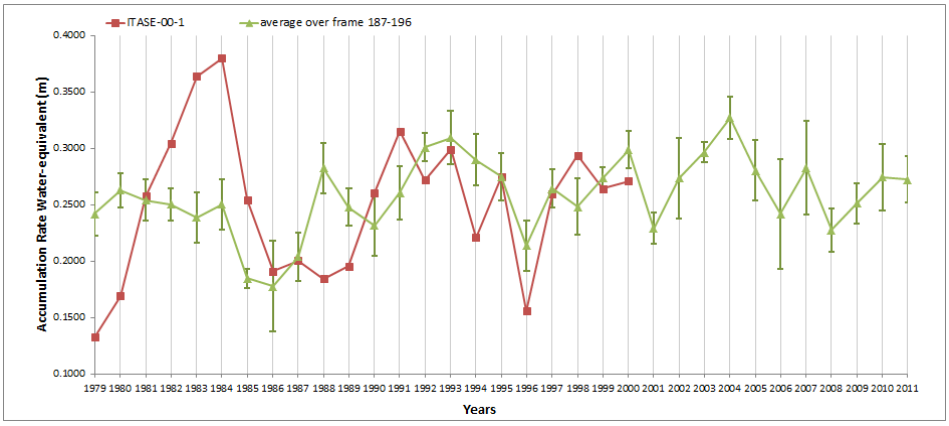

Figure 4.4 Plot of SWE series from ITASE-00-1 and Snow Radar frame 187-196.

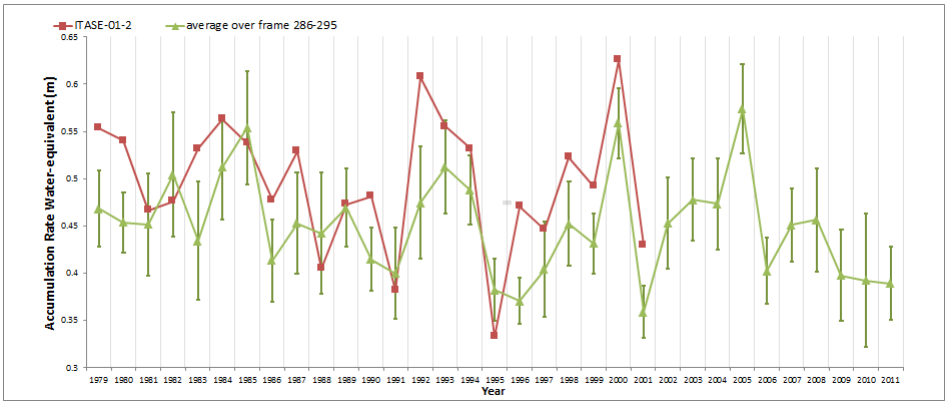

Figure 4.5 Plot of SWE series from ITASE-01-2 and Snow Radar frame 286-295.

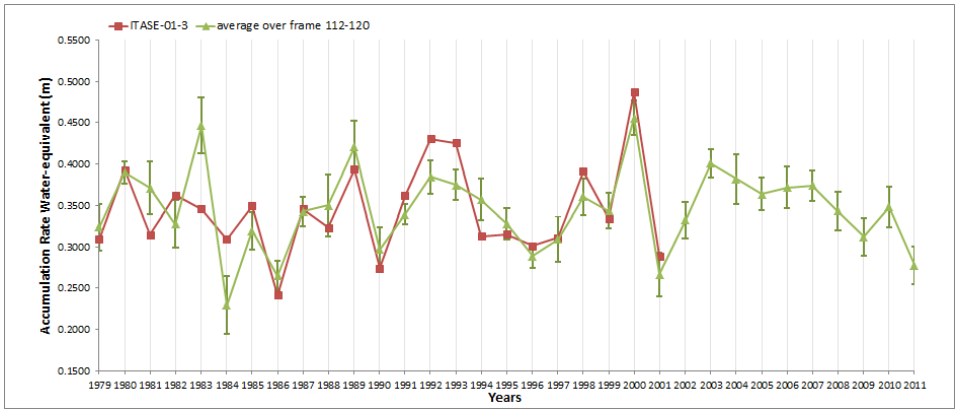

Figure 4.6 Plot of SWE series from ITASE-01-3 and Snow Radar frame 112-121.

Then, I calculated the correlation coefficients and p-values between SWE series from each frame with the three ice core SWE profiles. The comparison between 95 Snow Radar frames and three ITASE ice cores ends up with 285 pairs of correlation coefficients and p-values. From these correlation coefficients and p-values, it can be observed that ITASE-00-1 has nearly no relation with any of the frames. ITASE-01-2 only has strong correlation with the ten frames on the 20111112_01 segment that are within 20 km with the ice core. The correlation coefficients between ITASE-01-2 and the ten frames on segment 20111112_01 are around 0.65, and all of them are at a 1% significance level. ITASE-01-3 has correlation that at a 1% significance level with most of the frames, except frames from low accumulation area (frames 191-196). The correlation coefficients between frames and ITASE-01-3 range from 0.30 to 0.75. In addition, the correlation coefficients experience a decrease on segment 20111109_02 when moving away from ITASE-01-3. The resulting correlation coefficients and p-values are given in **Figure 7.1-Figure 7.3**.

As frames in the low accumulation area show a poor correlation with the ice core profiles, the temporal snow accumulation pattern may largely vary within close distance. Frames 142-169 are much closer to ITASE-01-2 ice core than to ITASE-01-3 ice core; however, the distance between frames 142-169 and ITASE-01-2 is perpendicular to the coast and the distance between frames 142-169 and ITASE-01-3 is parallel to the coast. In the result, frames 142-169 share a better correlation with ITASE-01-3 than with ITASE-01-2. This provides evidence for the assumption that the SWE temporal pattern changes more rapidly along the distance perpendicular to the coast than the distance parallel to the coast. Good consistency exists between the ice core annual accumulation pattern (ITASE-01-2/ITASE-01-3) and

corresponding Snow Radar detected horizons, despite noticeable differences between ice cores and Snow Radar SWE series. With the consideration of their different locations, the results of the comparison between Snow Radar and ice cores provides strong evidence that the layers between horizons represent annual accumulation.

4.1.3 Comparison between Snow Radar and RACMO2.1/ANT

RACMO2.1/ANT covers the time period from 1978 to 2012, with a monthly resolution. The sum of 12 months snow accumulation (January to December) defines the annual period and is used to compare with the Snow Radar derived annual snow accumulation. The RACMO2.1/ANT data is a gridded dataset, with a size of 0.25 degree per cell, which giving an approximate 27 km x 27 km cell size. RACMO2.1/ANT data provides the average snow accumulation within a grid cell. Overlaying Snow Radar flight line on the RACMO2.1/ANT grid shows the location of the flight line in terms of the grid cells (**Figure 4.7**). In **Figure 4.7**, the red/pink color block stands for flight line that is in different RACMO2.1/ANT grid cell, the grid boundary of the grid that has flight line comes through is drawn in blue, and the grids are numbered for further analysis.

In order to compare Snow Radar and RACMO2.1/ANT derived snow accumulation, the flight line is divided based on where it crosses a grid cell boundary. The averaged snow accumulation of the Snow Radar data subset within every grid cell is calculated to compare with the RACMO2.1/ANT grid cell average snow accumulation. 201111009_02 segment spreads over 19 RACMO2.1/ANT grid cells; 20111112_01 segment spreads over 4 RACMO2.1/ANT grid cells. The lengths of the flight line

segment in each RACMO2.1/ANT grid cell vary, directly relating to the number of picked layer points. It is reasonable to expect that the consistency between Snow Radar and RACMO2.1/ANT data is when the flight line is longer and has a larger number of picked layer points within a grid cell. The numbers of picked layer points in each grid cell are shown in **Figure 4.8.**

The mean and standard deviation values of the 33-year SWE series along the flight segment and the grid cell are similar (**Table 7-2**). In addition, 23 pairs (23 grid cell) of SWE series from Snow Radar and RACMO2.1/ANT are compared using correlation coefficients and p-values. The result is shown in **Figure 4.8**.

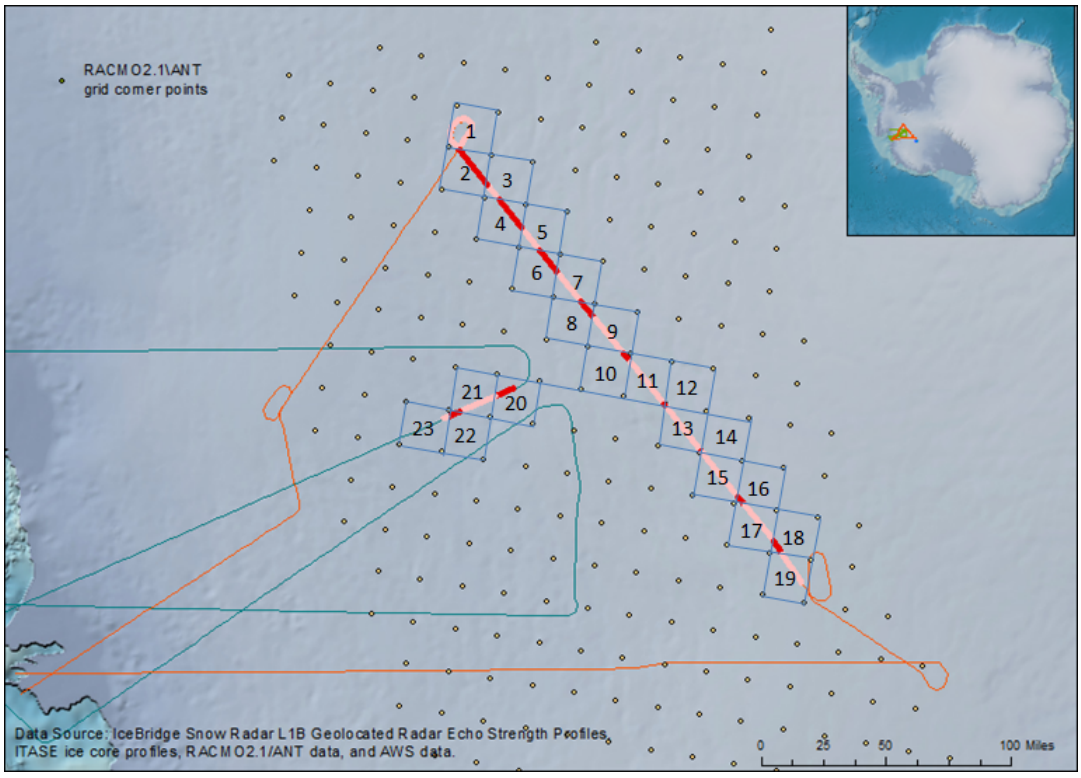

Figure 4.7 Distribution of flight line in RACMO2.1/ANT grid cell (red/pink color block along the study segment subset indicates flight line in different RACMO2.1/ANT grid, and the blue boxes indicate the grid cell boundary).

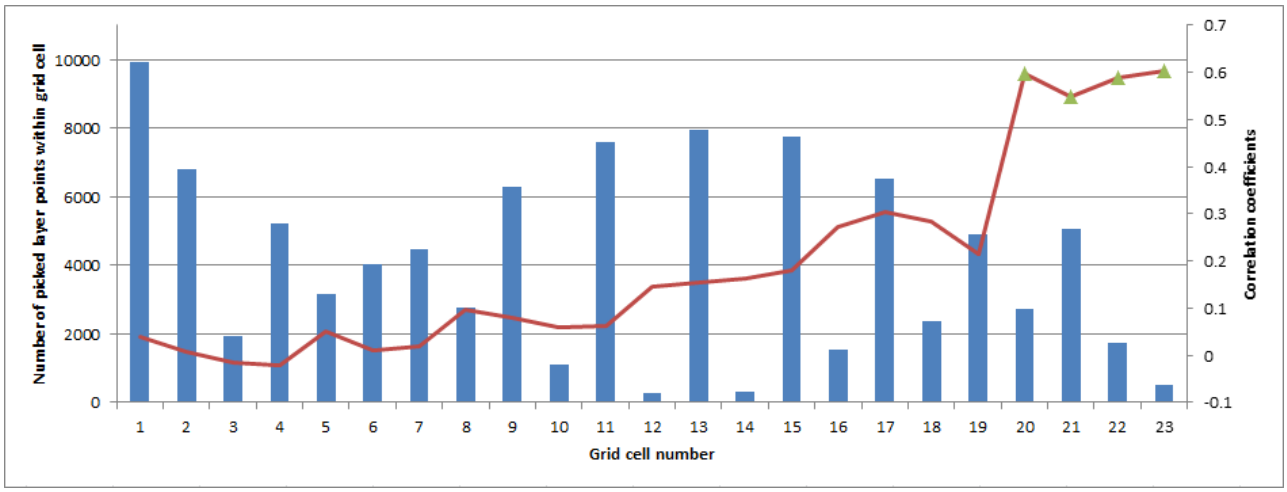

Figure 4.8 Number of picked points within grid cell (blue histogram represents number of picked points in each grid cell, red line represents correlation coefficients, and green triangle marker represents the correlation coefficients that are significant at 5% significant level)

The correlation coefficients that are significant at the 1% significance level are found in grid cells 20, 21, 22 and 23, and their values are around 0.6. The rest of the grid cells fail to have good consistency between the two datasets. There is no noticeable correlation between the number of picked points in each grid cell and the correlation coefficients, as expected. To verify this result, I further compared RACMO2.1/ANT data with ice core data. Their correlation coefficients and p-values illustrate the same result that a similar snow accumulation pattern is found only in grid cell 21 with ITASE-01-2. The correlation coefficient between grid cell 21 and ITASE-01-2 is 0.53 and is significant at the 1% significance level. It seems that model data shares a better correlation with other datasets in locations closer to the coast, rather than areas further inland. Another finding is that in grid cell 1 to grid cell 19, the meteorological model estimated mean annual accumulations are all smaller than that obtained by the Snow Radar with a mean bias of 0.096 m, and in grid cell 20 to grid cell 23, the meteorological model

estimated mean annual accumulations that are all larger than that obtained with the Snow Radar with a mean bias of 0.065 m.

4.1.4 Volcanic Layers Detection

When large volcanic eruptions occur, huge quantities of acids and aerosols are introduced into the atmosphere and distributed over vast areas. In ice cores, volcanic layers can sometimes be identified, and are widely used in ice core dating (Ferris et al., 2011; Gao et al., 2008). During my study period, two major volcanic eruptions occurred: El Chichón (Mexico) in 1982 and Pinatubo (Philippines) in 1991. Because of the huge quantities of aerosols emitted from these two volcanic eruptions, the stratospheric optical thickness of atmosphere shows the two peaks occurring after each eruption (**Figure 4.9**).

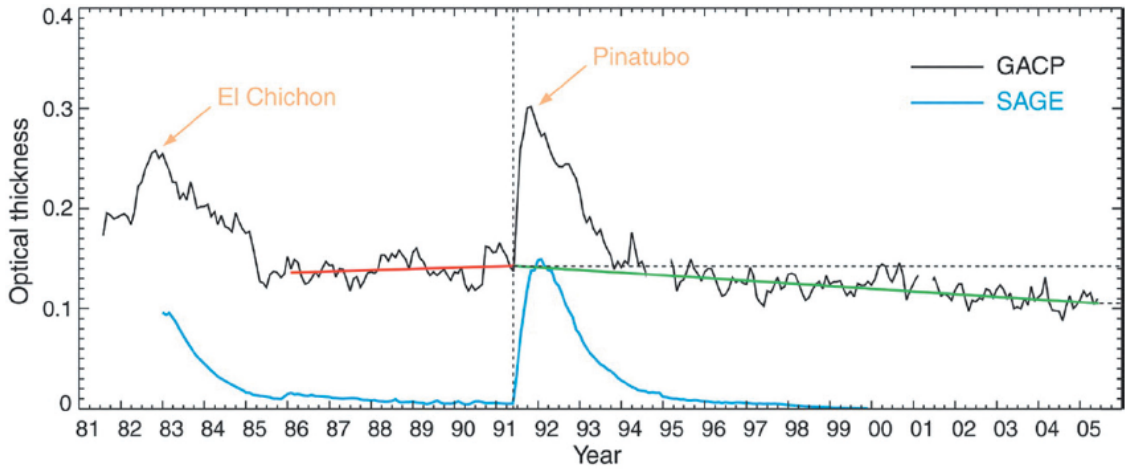

Figure 4.9 Time series of the globally-averaged column AOT over the oceans and the SAGE record of globally-averaged stratospheric AOT (Lee, Li et al. 2009).

Given one or two years transport and deposition time, the acids and aerosols from volcanic eruptions can be found in ice segments associated with years 1982/1983 and 1992/1993. In most of the studied Snow Radar echograms, the internal layers for the years 1982 and 1993 were found to have slightly stronger echoes (**Figure 4.7**). These stronger echoes can serves as a tie point in reconstructing the chronology of the Snow Radar detected internal layers, and provide further evidence that the internal layers detected are annual layers.

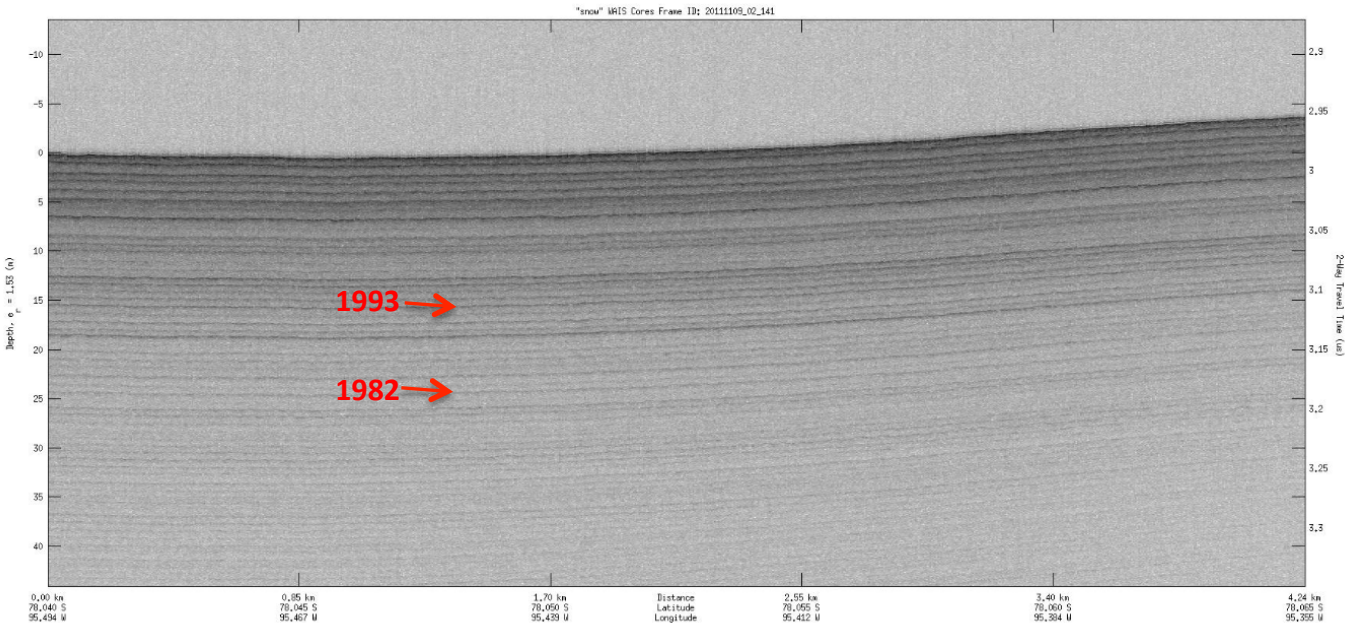

Figure 4.10 Snow Radar echogram (frame 141).

4.1.5 Conclusion on Chronology of Snow Radar

According to the analysis in **4.1.2 Comparison between Snow Radar and Ice Core, 4.1.3 Comparison between Snow Radar and RACMO2.1/ANT, and 4.1.4 Volcanic Layers Detection**,

there is strong evidence that the chronology of Snow Radar echoes generally follow an annual pattern. The following tests and analyses assume the detected internal layers are annual layers.

4.2 Snow Radar Annual Layer Detection Limit

In **3.1 Measurement Error in Picking**, a method to estimate measurement error variance is provided for a given SWE range. A regression model can be applied to model the relationship between measured error variance and SWE. With this model, one can decide the best regions where the current Snow Radar configuration can be flown to obtain annual accumulation layers.

To derive a more accurate correlation between variance of measurement error and SWE, more re-picking of the data is better. But, due to the large time commitment currently required by the picking process, I obtained additional "re-picking" data by shortening the average distance over the repeat picking I had already done (Section 3.1), instead of actually picking additional data. The data used in Section **3.1** is the mean value over the selected frame groups, each of which contains two frames. This process provides only one measurement error variance per selected frame group. If the SWE series is averaged over a shorter distance, additional measurement error variance values can be obtained from the original frame group. To accomplish this, I averaged the SWE series over a distance of 2 km. Then every frame group provides five values of measurement error variance. The derived measurement error variance is plotted against the correspondent mean annual SWE (**Figure 4.11**).

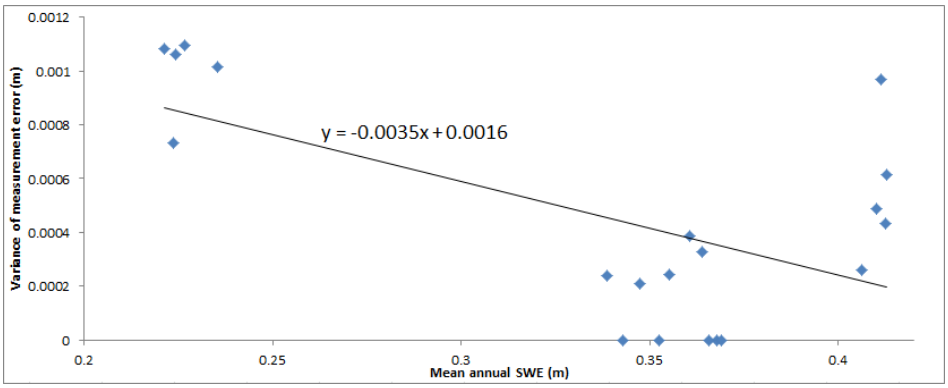

Figure 4.11 Variance of measurement error against the mean annual SWE.

A linear regression is plotted in **Figure 4.11**. This observed negative slope has R-sq of 0.37, F-ratio of 10.42, and significant level of 0.0047. Thus it has more than 99% confidence that the negative relation exists between the measurement error variance and the mean annual SWE. This correlation is described as:

$$\sigma_{U_{ij}}^2 = -0.0035 \cdot SWE + 0.0016. \tag{4.1}$$

and the standard deviation of measurement error is:

$$\sigma_{U_{ij}} = \sqrt{-0.0035 \cdot SWE + 0.0016}. \tag{4.2}$$

When the standard deviation of measurement error is much smaller than the standard deviation of repeated picking, the echogram should be very easy to pick; as the standard deviation of measurement error increases, the picking accuracy decreases, since the measurement error produces more fluctuation in the result than the normal picking process. As discussed in **3.1.2 Size of Measurement Error**, most

of the standard deviation of repeated picking is less than 0.017 m. I set the threshold for easy picking as this value, and at larger values, difficulties in picking annual layers chould be expected.

RACMO2.1/ANT provides annual SWE for all of Antarctica; using this along with the regression equation (4.2) the standard deviation of measurement error can be used to map the difficulty of picking over Antarctica as shown in **Figure 4.11**. In this map, the red and orange colored areas have a standard deviation of measurement error smaller than 0.017, representing areas where the Snow Radar data can readily resolve annual firn layers. Yellow, light green, and dark green areas have a standard deviations of measurement error that indicate an increased difficulty in the detection of annual layers. **Figure 4.12** shares a similar spatial distribution with the mean annual SWE map. In the interior of Antarctica where annual SWE is low, measurement error variance is large, whereas along the coastal margins where annual SWE is high, measurement error variance is small. Thus this measurement error variance map provides a guide for consideration in future fieldwork.

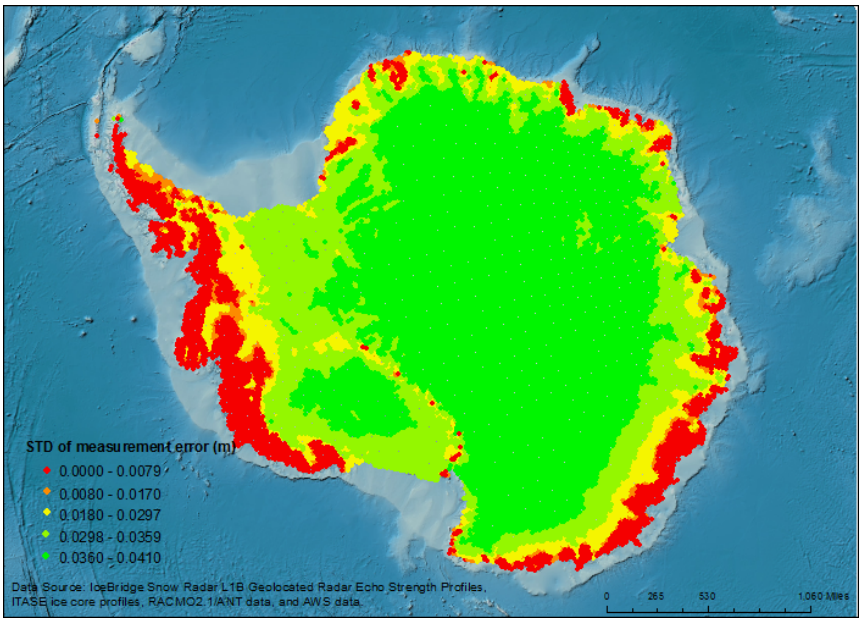

Figure 4.12 Standard deviation of Snow Radar picking measurement error.

4.3 Snow Accumulation Trend Test Results

In order to find the long-term trends in snow accumulation during the studied period of 1979 to 2011, linear regression models have been applied to the SWE series derived from Snow Radar, ITASE ice core, and RACMO2.1/ANT with time series. The R-sq and F-values are calculated to assess whether a trend is significant. Secondly, the TFPW Mann-Kendall trend test introduced in Section **3.4 (Mann-Kendall Trend Test)** is also applied to the three datasets. Considering the time span of the datasets, 22/23 years SWE series (1979-2000 for ITASE-00-1; 1979-2001 for ITASE-01-2 and ITASE-01-3) will be tested in ITASE dataset for trend. Both Snow Radar and RACMO2.1/ANT dataset will be tested for trends during the period from 1979 to 2011.

4.3.1 Linear Regression Model

A linear regression model is a simple but effective way to test whether a trend exists in a series of values. The R-sq and F-ratio mentioned in Section **3.1.1 (Classical Additive Measurement Error Model)** provide a reliable way to evaluate a linear regression. For the three datasets examined, I have tested each SWE series using R-sq and F-ratio. The three ice cores are calculated separately. The 23 RACMO2.1/ANT grid cells mentioned in Section **4.2.3 (Comparison between Snow Radar and RACMO2.1/ANT)** are selected to represent RACMO2.1/ANT data. Based on the frames' spatial distribution to ice core locations (**Figure 3.7**), Snow Radar data are divided into frame groups 112-142, 143-169, 170-196, and 286-295. The resulting R-sq values are all very small (< 0.05). The F-ratio values are also very small (< 2), while the Table of critical values for the F distribution from NIST/SEMTECH Engineering Statistics Handbook (Filliben, 2002) provides 4.35 for 1 regression DF and 20 residual DF level and 4.33 for 1 regression DF and 21 residual DF at 5% significance. The p-values are very large, larger than 0.5, indicating failures to reject null hypothesis. Thus the result from linear regression suggests that no trend in snow accumulation exists during the study period for any of the three datasets.

4.3.2 TFPW Mann-Kendall Trend Test

According to Section **3.4.3 (Modified Mann-Kendall Trend Test for Auto-correlated Data)**, the S, t, z-value, and p-value are calculated for each SWE series from the three datasets. The resulting t values are very small, while p-values are large. Specifically, the t values from the TFPW Mann-Kendall trend test are all < 0.02, for the Snow Radar, ITASE ice core, and RACMO2.1/ANT SWE series. Such small t value indicates the lack of a trend. The resulting p-values are all > 0.4. The null hypothesis cannot be

rejected according to these p-values. Therefore, the TFPW Mann-Kendall trend test also finds no trend exists in the snow accumulation time series. The resulting S scores, t, z-values, and p-values from TFPW Mann-Kendall trend test are shown in **7.3 Trend Test Results**.

4.3.3 Conclusion on Trend Test

Both the linear regression model and TFPW Mann-Kendall trend test show that SWE does not experience any significant trend during the studied time period. This result agrees with my hypothesis that was based on prior studies (Lenaerts et al., 2012a; Medley et al., 2013; Monaghan et al., 2006). The stable SWE through the studied three decades is counter to an expected SWE increase due to evidence of regional warming: the long-term (1957-2011) surface temperature archive in Byrd AWS shows a significant increase ($0.47 \pm 0.23°C$ per decade), which is substantially greater than the global average ($0.13 \pm 0.03°C$ per decade) (Bromwich, 2012). Accompanied by an accelerating ice loss along the WA coast (King et al., 2012; Rignot, 2006; Rignot et al., 2008), the net mass loss in WA is greater than expected.

4.4 Spatial Distribution of SWE and Possible Reasons for Such Distribution

In addition to the temporal distribution of SWE discussed in the above sections, the spatial distribution of SWE is also of interest. In EA, the spatial variability of snow accumulation at the kilometer scale is found to be one order of magnitude higher than temporal variability at the multi-decadal scale (Frezzotti et al., 2005), indicating the importance of SWE spatial distribution. The spatial distribution of SWE is

influenced by interactions between the large-scale surface topography of ice divides and the wind field of strong-wind events that are often associated with high-precipitation events (Fujita et al., 2011; Veen et al., 2001). Topography and wind are the two factors in SWE spatial distribution that have been studied most frequently (Dadic et al., 2010; Fujita et al., 2011; Trujillo et al., 2007).

Topography is often described by elevation, surface slope, and surface roughness in the study of ice sheets (Muszynski and Birchfield, 1985; Van der Veen et al., 2009; Veen et al., 2001). Surface slope provides information on the degree of surface slope and its orientation, which influences SWE in the company of wind redistribution (Arcone et al., 2005; King et al., 2004). Surface roughness on a large scale (> 1 km) relates to elevation and on a small scale (< 1 km) relates to snow redistribution (Van der Veen et al., 2009; Veen and Bolzan, 1999). Since the spatial scale of data frames used in this study are large (~ 4.5 km), I tested the correlation between elevation, surface slope and SWE. Plots of the mean annual SWE along the flight lines versus local elevation are given in **Figures 4.13 - 4.14**.

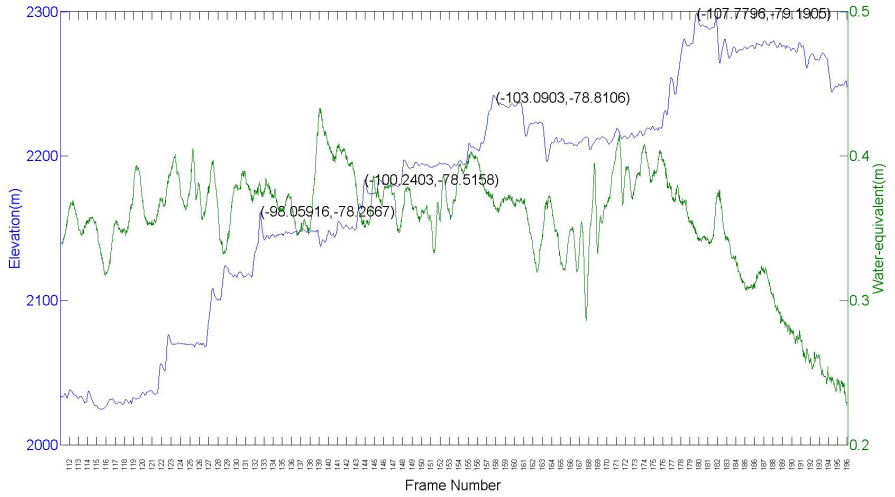

Figure 4.13 SWE against elevation (segment 20111109_02).

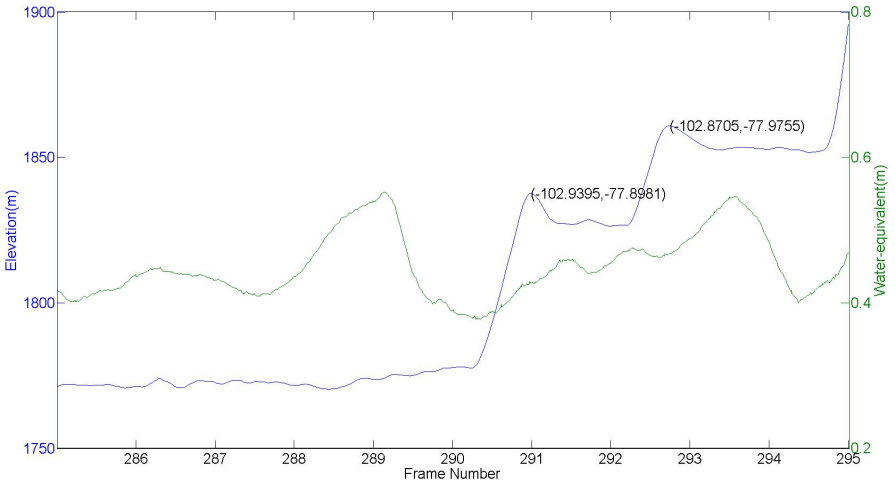

Figure 4.14 SWE against elevation (segment 20111112_01).

The correlation between elevation and SWE seems to be negative in **Figure 4.9**, but no clear correlation between them can be seen in **Figure 4.10**. The Wilcoxon rank sum test is performed, and both of the segments return a value of 1, implying the existence of a relation between elevation and SWE. The correlation coefficient and p-value between elevation and SWE is correspondingly -0.3601 and ~0 in

segment 20111109_02, while 0.2710 and ~0 in segment 20111112_01. For the extremely small p-value, the slight negative and positive correlations between elevation and SWE separately in segment 20111109_02 and 20111112_01 both have high confidence. The different correlation between elevation and SWE found in the two segments may be due to the difference in their path length and height. While studied frames on segment 20111109_02 extends for about 370 km, studied frames on segment 20111112_01 extends only for 40 km. Shorter length may not be able to correctly reflect the correlation between elevation and SWE, since other factors may influence snow distribution. Further, the elevation along segment 20111109_02 changes by 274 m, while the elevation along segment 20111112_01 changes only 125 m. The less elevation change along segment 20111112_01 may also be the reason for the positive correlation. Negative correlation between elevation and SWE has been found in large area in Antarctica and may be explained by the decreasing surface temperature associated with increasing elevation, or precipitation shadow effects caused by passing over an ice divide (Giovinetto et al., 1990; Medley et al., 2013).

Wind plays a key part in snow redistribution and sublimation on smaller scales. It has been found that SWE is generally lower on leeward slopes than on the windward slopes (Arcone et al., 2005; King et al., 2004). This study has incorporated wind information from Byrd Station AWS to assess this. The 16 wind direction sectors have been used to examine the prevailing wind directions at Byrd station. From the wind data provided by Byrd AWS, the dominant wind directions are found to be from N to NE (**Figure 4.12**). To be able to move the surface snow, a wind speed of ~6 m/s is required. Thus, when

considering the wind direction distribution, this study excluded observations where the wind speed was lower than 6 m/s.

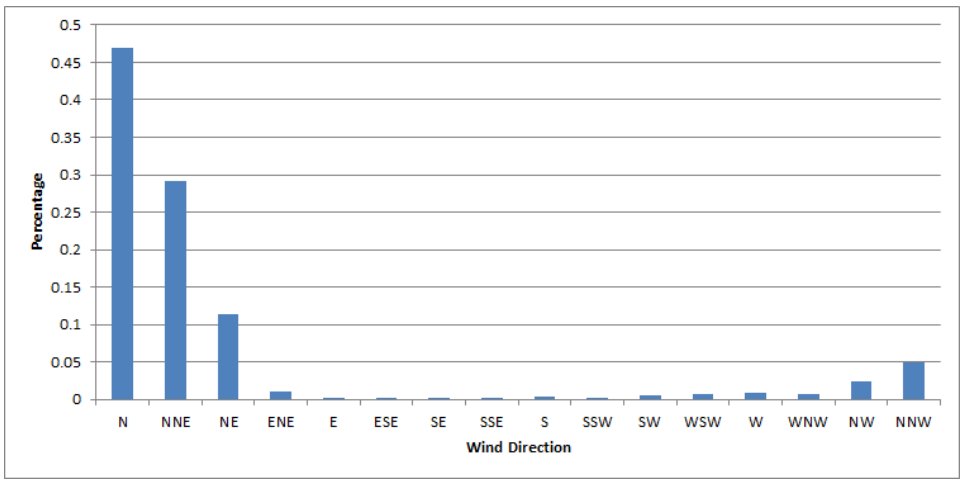

Figure 4.15 Wind direction distribution for wind speeds greater than or equal to 6 m/s (Byrd AWS).

With this dominant wind direction, the leeward slope direction is S to SW (180° – 202.5°), with a windward direction from N to NE (0° – 67.5°). Frame 112 to 196 on segment 20111109_02 aligns SW-WSW to NE-ENE. Thus the wind direction is from 112 to 196 with an approximate offset angle of 20° to 30°between the flight segment and prevailing wind direction. This study estimates the surface slope over every 1 km from frame 112 to 196 using linear regression model. Under this estimation, positive slope indicates windward slope, and negative slope indicates leeward slope. The Wilcoxon rank sum test shows there is a relation between surface slope and SWE. The correlation coefficient and p-value for these two parameters are 0.1258 and 0.0155. Local SWE maxima mostly associate with positive slope (windward) and local SWE minima mostly associate with negative slope (leeward) (**Figure 4.16**). These results thus agree with the study by Arcone et al (Arcone et al., 2005).

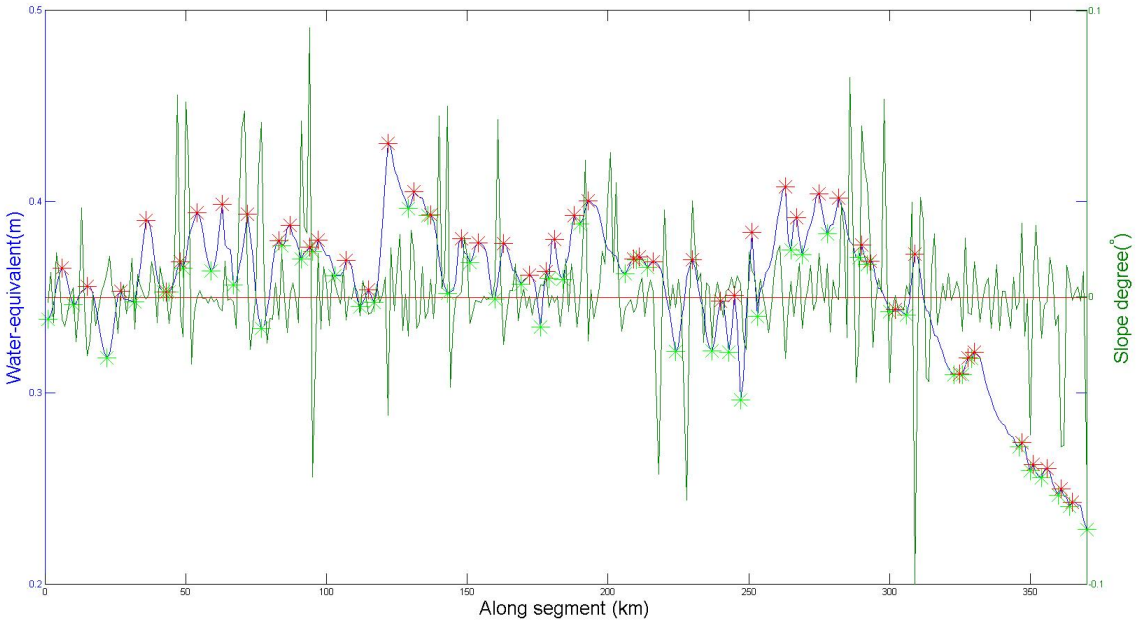

Figure 4.16 SWE versus elevation linear regression coefficient: red star marker represents local maxima and green star marker represents local minima.

4.5 Relations with AWS and SIE data

Although there is no obvious long-term trend that resides in the SWE series, it is still valuable to test if there are any small fluctuations within the SWE series that relate to weather events. The analysis of AWS and SIE data has been described in Section **2.5 (AWS and SIE)**. AWS data provide observations of surface temperature, pressure, wind speed, and wind direction. The surface temperature and atmospheric pressure can be related to precipitation through synoptic scale weather systems. Higher temperatures can be related to moist marine air masses in this region that can influence precipitation amounts; while lower surface pressure is associated strong storms (low pressure systems). Wind mainly influences snow accumulation through snow redistribution. SIE influences the distance marine moisture

travels to ice sheet areas. This study tests the correlation between the SWE series derived from four Snow Radar frame groups (112-142, 143-169, 170-196, and 286-295 (**Figure 4.17**)) with surface temperature, pressure percentiles and SIE data.

Another concern is that Byrd AWS is located about 100 km from the closest frame (196). It is thus necessary to test the representativeness of these data to local weather parameters. Kominko-Slade AWS (79.47°S, 112.11°W) is located about 20 km away from the closest frame (196) (**Figure 4.17**), but data are only start in 2009. A comparison between the overlapping five years (2009-2012) between Byrd and Kominko-Slade AWSs shows good consistency in the trend of surface temperature and pressure values at 5%ile and 95%ile (**Figure 4.18**). Hence we must keep in mind that the weather data provided by Byrd AWS may not sufficiently represent weather conditions in the study area.

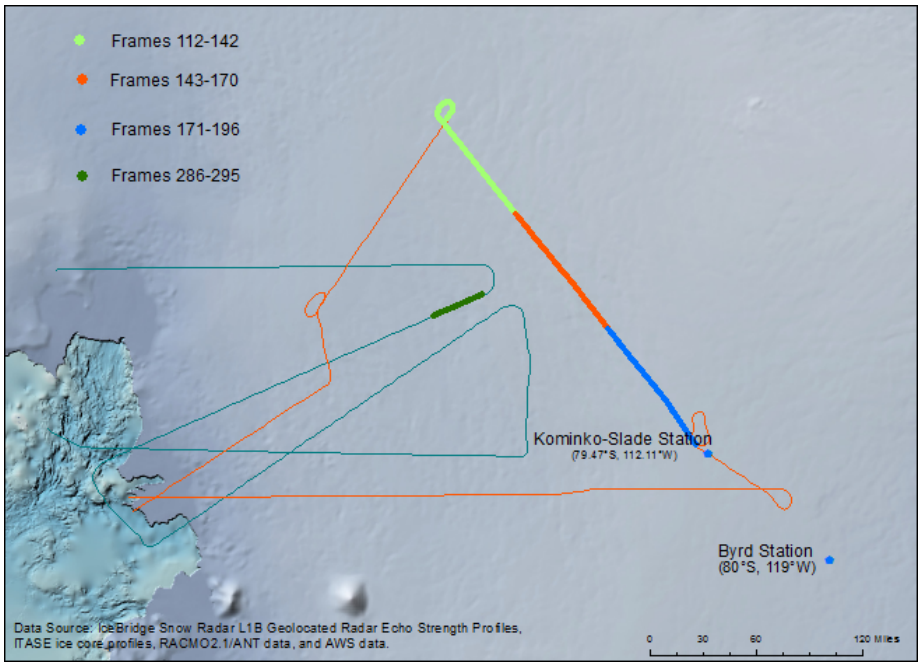

Figure 4.17 Locations of Byrd and Kominko-Slade AWS

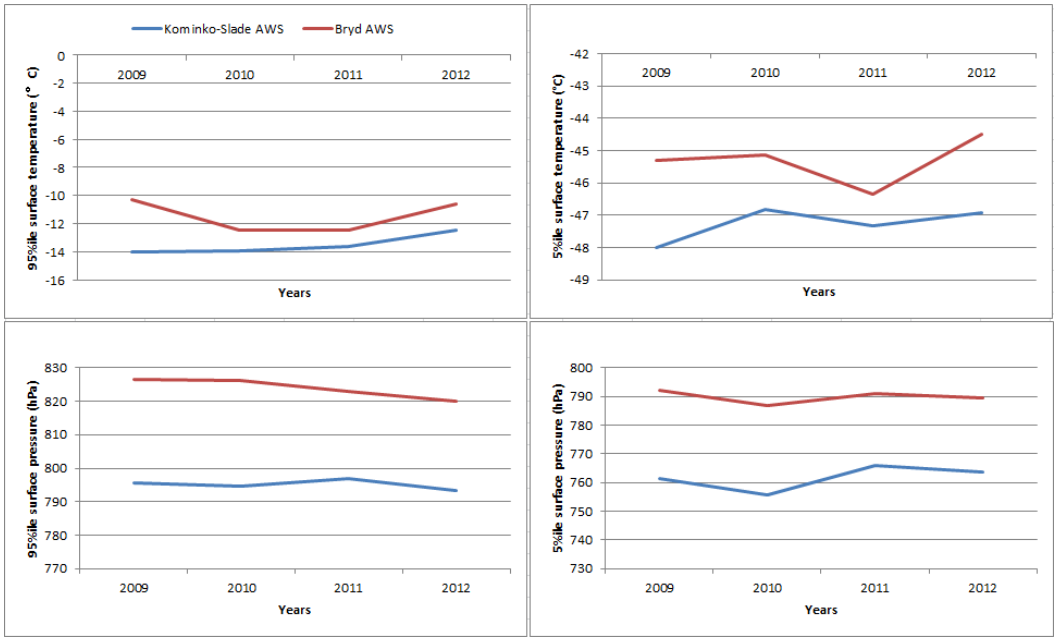

Figure 4.18 Comparison between surface temperatures and pressures at 5%ile and 95%ile from Byrd AWS and Kominko-Slade AWS

The temporal coverage of AWS is 1980-2011, with missing data for the years 1988, 1989, 1992, 1993, 1996, 1999, 2001,2002, 2004, and 2005; the temporal coverage of SIE is 1980-2010. The available records that can be compared to SWE series are 21 for AWS data and 31 for SIE data. For the small number of available records, it is unreliable to use the t-test to determine the existence of a relation between SWE, AWS and SIE data. Hence this study adopted the Wilcoxon rank sum test, a nonparametric alternative to the t-test. The seven parameters from AWS and SIE (95%ile temperature, 5%ile temperature, 95%ile pressure, 5%ile pressure, maximum SIE, median SIE, and minimum SIE) all give result of 1, which implies that SWE relates to the seven parameters. Correlation coefficient and p-values were also calculated between SWE, AWS, and SIE data (**Table 4-1**). From the resulting correlation coefficients and p-values, both the temperature 5%ile and pressure 5%ile show positive

correlations to SWE in frame group 143-169 and 170-196, with a correlation coefficient around 0.4 and p-value smaller than 0.05. For the rest of the parameters, no statistically significant correlations are found. The correlation coefficients and p-values between snow accumulation and the mean and median values of AWS and SIE are shown in Appendices (**Table 7-6**). This research also tested the correlation between snow accumulation and Southern Oscillation Index and found no statistically significant correlations.

Table 4-1 Correlation coefficient and p-value between SWE, AWS, and SIE data

Name	**R**	**P-value**	**R**	**P-value**	**R**	**P-value**	**R**	**P-value**
	T 95%		**T 5%**		**P 95%**		**P 5%**	
112-142	-0.031	0.8903	0.384	0.0770	-0.122	0.5791	0.314	0.1444
143-170	-0.069	0.7604	0.494	0.0193	-0.205	0.3465	0.420	0.0459
170-196	-0.013	0.9531	0.448	0.0362	-0.185	0.3965	0.447	0.0321
286-295	-0.092	0.6809	0.117	0.6024	-0.254	0.2421	0.110	0.6157
Name	**R**	**P-value**	**R**	**P-value**	**R**	**P-value**		
	max		**med**		**min**			
112-142	-0.349	0.0539	-0.24	0.1803	-0.042	0.8225		
143-170	-0.297	0.1041	-0.30	0.0902	-0.144	0.4390		
170-196	-0.335	0.0647	-0.33	0.0625	-0.269	0.1433		
286-295	-0.121	0.5155	-0.11	0.5478	0.24	0.1891		

Temperature at 95% percentile is shorten as T 95%, temperature at 5% percentile is shorten as T 5%, pressure at 95% percentile is shorten as P 95%, pressure at 5% percentile is shorten as P 5%, maximum SIE is shorten as max, median SIE is shorten as median, and minimum SIE is shorten as min for space reason.

*. Correlation is significant at the 0.05 level.

5 Conclusion and Future Work

5.1 Overview of Significant Findings

The objective of this research is to determine annual snow accumulation over a large area of West Antarctica using airborne Snow Radar data. The Snow Radar was designed, built and operated by CReSIS, and for this study, was flown on a NASA DC-8 aircraft as part of Operation IceBridge. Starting with processed radar data (echograms), this study identified near-surface internal layers in the echograms. This study aimed to assess the accuracy and uncertainties of Snow Radar data and its ability to provide annual resolution of snow accumulation. Ice cores and regional climate model provide assured annual snow accumulation as reference. Comparison between the snow accumulation derived from Snow Radar, ice cores, and regional climate model are made to address the chronology of Snow Radar detected ice sheet internal layers. The long-term (33 year) snow accumulation series is analyzed to identify trends, if any, over the study period (1979-2011). Spatial distribution of annual accumulation has also been examined, in terms of elevation and surface slope. Weather observations from an AWS

and observations of sea ice extent in the Amundsen Sea have also been compared with annual snow accumulation series.

In regards to the first research question, this study has established that there is a high confidence that the internal layers detected to depths of 20-30 m by the Snow Radar have approximately an annual separation. This fact allows a chronology of snow accumulation with annual resolution to be obtained. This has been accomplished through comparisons with ice core and regional climate model data. The three methods of determining snow accumulation show similar mean and standard deviation values, and have similar temporal patterns. In the correlation analysis between Snow Radar and the ice cores, and between Snow Radar and regional climate model data, good consistency is found. In addition, two strong echoes are spotted in most of the analyzed Snow Radar echograms, which points to two major volcanic events: El Chichón (Mexico) in 1982 and Pinatubo (Philippines) in 1991. Thus, the chronology of Snow Radar detected layers is supported as annual layers.

With the evidence that the Snow Radar chronology is approximately annual, the detected 33 accumulation layers are dated as a SWE time series from 1979 to 2011. Both temporal and spatial distributions in SWE have been analyzed for the second research question. West Antarctic accumulation data examined here (Snow Radar, ice core, and meteorological model) all show no detectable trend during the three decades (1979-2011). This has implications for sea level rise, since the mass flux from melting and calving processes along the ice sheet margins are accelerating (King et al., 2012; Rignot, 2006; Rignot et al., 2008).

In order to find the causes for the spatial distribution of snow accumulation in study area, this study examined the relationship between accumulation and both elevation and surface slope. A statistically significant negative correlation between mean annual snow accumulation and elevation was found along a 370 km flight line segment. This relationship is likely explained by upslope depletion and precipitation shadow effects. The surface slope and wind direction were also found to be related to the mean annual accumulation spatial distribution. These results were similar to previous studies that showed accumulation is generally lower on leeward slopes as compared to the windward slopes (Arcone et al., 2005; King et al., 2004).

To answer the third research question, possible relationships between the annual fluctuations of accumulation and observations of surface temperature, pressure and sea ice extent have been examined. Comparing accumulation to the annual 5%ile value of temperature and pressure resulted in positive correlation coefficients of ~0.4 that are significant at 5% significance level. These results point to a connection between years with very strong cyclonic weather events and decreased precipitation (possibly due to blowing snow), and years having warmer winter temperatures (marine air mass influence) being associated with increased precipitation.

5.2 Future Work

In the process of answering the main research questions, new questions were raised. Several directions for future work and improvement can be suggested. First, one area of improvement could be to involve more than one person in tracking and quantifying the internal layers observed in the Snow Radar data.

The measurement error analysis conducted in this study was based on only one experienced "picker", and it is not clear how representative these results are for a group of experienced "pickers". Second, assessment of the results presented in the research could be performed as new ice core data in this region becomes available (i.e. SEAT cores (Burgener et al., 2013)). Third, additional flight paths need to be analysed to obtain broader coverage of accumulation within West Antarctica.

The analysis on the correlation between snow accumulation and climate in this research is limited, with only statistically significant correlations found for temperature and atmospheric pressure extremes. Evidence of teleconnections between El Niño Southern Oscillation (ENSO), WA climate and WA snow accumulation has been previously found (Gregory and Noone, 2008; Harangozo, 2000; Peterson and White, 1998; Schneider et al., 2012; Yuan, 2004), as well as an identified teleconnection between ENSO and WA climate via local sea ice extent (Harangozo, 2000). $\delta^{18}O$ isotope in WA ice core records is also found to be teleconnected with ENSO (Gregory and Noone, 2008). However, in the 33 year period examined in this study, a significant correlation between ENSO and snow accumulation was not found. The Snow Radar dataset has the potential to examine regional accumulation for a longer time period, and it would be worthwhile to examine a longer time series, which is the fourth possible improvement.

The high frequency airborne radar continues to be improved, and will continue to be an important tool in understanding snow accumulation in polar regions, and leading to improved understanding of spatial and temporal trends in accumulation. The Snow Radar provides a unique method of assessing regional scale accumulation on ice sheets and over sea ice that will continue.

6 References

Ackley, S. and Keliher, T., 1979. Ice sheet internal radio-echo reflections and associated physical property changes with depth. Journal of Geophysical Research: Solid Earth (1978–2012), 84(B10): 5675-5680.

Allen, C., A Brief History Of Radio–Echo Sounding Of Ice.

Alley, R., Blankenship, D., Bentley, C. and Rooney, S.T., 1986. Deformation of till beneath ice stream B, West Antarctica.

Arcone, S.A., Spikes, V.B. and Hamilton, G.S., 2005. Stratigraphic variation within polar firn caused by differential accumulation and ice flow: Interpretation of a 400 MHz short-pulse radar profile from West Antarctica. Journal of Glaciology, 51(174): 407-422.

Bamber, J., 1987. Internal reflecting horizons in Spitsbergen glaciers. Ann. Glaciol, 9: 5-10.

Bromwich, D.H., Nicolas, J.P., Monaghan, A.J., Lazzara, M.A., Keller, L.M., Weidner, G.A., Wilson, A.B., 2012. Central West Antarctica among the most rapidly warming regions on Earth. Nature Geoscience: 139-145.

Burgener, L. et al., 2013. An observed negative trend in West Antarctic accumulation rates from 1975 to 2010: Evidence from new observed and simulated records. Journal of Geophysical Research: Atmospheres, 118(10): 4205-4216.

Butler, W., Poitevin, P. and Bjomholt, J., 2007. Benefits of wide area intrusion detection systems using FMCW radar, Security Technology, 2007 41st Annual IEEE International Carnahan Conference on. IEEE, pp. 176-182.

Carroll, R.J., Ruppert, D., Stefanski, L.A. and Crainiceanu, C.M., 2012. Measurement error in nonlinear models: a modern perspective. CRC press.

Chen, J., Wilson, C., Blankenship, D. and Tapley, B., 2009. Accelerated Antarctic ice loss from satellite gravity measurements. Nature Geoscience, 2(12): 859-862.

Chen, J.L., Wilson, C. R., Tapley, B. D., 2013. Contribution of ice sheet and mountain glacier melt to recent sea level rise. Nature Geoscience, 6: 549-552.

Crandall, D.J., Fox, G.C. and Paden, J.D., 2012. Layer-finding in radar echograms using probabilistic graphical models, Pattern Recognition (ICPR), 2012 21st International Conference on. IEEE, pp. 1530-1533.

Dadic, R., Mott, R., Lehning, M. and Burlando, P., 2010. Wind influence on snow depth distribution and accumulation over glaciers. Journal of Geophysical Research: Earth Surface (2003–2012), 115(F1).

Danneberg, J., 2012. Changes in runoff time series in Thuringia, Germany–Mann-Kendall trend test and extreme value analysis. Advances in Geosciences, 31.

Davis, C.H., Dean, R.H. and Xin, W., 1990. Radar reflections from water injected into an Antarctic glacier. Geoscience and Remote Sensing, IEEE Transactions on, 28(4): 723-726.

Davis, C.H., Li, Y., McConnell, J.R., Frey, M.M. and Hanna, E., 2005. Snowfall-driven growth in East Antarctic ice sheet mitigates recent sea-level rise. Science, 308(5730): 1898-1901.

Davis, C.H., Li, Y., McConnell, J. R., Frey, M. M., Hanna, E., 2005. Snowfall-driven growth in East Antarctic ice sheet mitigates recent sea-level rise. Science, 308: 1898-1901.

Divers, J., Redden, D.T., Carroll, R.J. and Allison, D.B., 2011. How to estimate the measurement error variance associated with ancestry proportion estimates. Statistics and its interface, 4(3): 327.

Drewry, D.J., 1975. Comparison of electromagnetic and seismic-gravity ice thickness measurements in East Antarctica. Journal of Glaciology, 15: 137-150.

Eisen, O., Nixdorf, U., Wilhelms, F. and Miller, H., 2004. Age estimates of isochronous reflection horizons by combining ice core, survey, and synthetic radar data. Journal of Geophysical Research: Solid Earth (1978–2012), 109(B4).

Evans, S. and Smith, B., 1969. A radio echo equipment for depth sounding in polar ice sheets. Journal of Physics E: Scientific Instruments, 2(2): 131.

Feldl, N. and Roe, G.H., 2011. Climate variability and the shape of daily precipitation: A case study of ENSO and the American West. Journal of Climate, 24(10): 2483-2499.

Ferris, D.G., Cole-Dai, J., Reyes, A.R. and Budner, D.M., 2011. South Pole ice core record of explosive volcanic eruptions in the first and second millennia AD and evidence of a large eruption in the tropics around 535 AD. Journal of Geophysical Research: Atmospheres (1984–2012), 116(D17).

Field, C.B., 2012. Managing the risks of extreme events and disasters to advance climate change adaptation: special report of the intergovernmental panel on climate change. Cambridge University Press.

Filliben, J., 2002. NIST/SEMTECH Engineering Statistics Handbook. Gaithersburg: www. itl. nist. gov/div898/handbook, NIST.

Frezzotti, M. et al., 2005. Spatial and temporal variability of snow accumulation in East Antarctica from traverse data. Journal of glaciology, 51(172): 113-124.

Fujita, S. et al., 2011. Spatial and temporal variability of snow accumulation rate on the East Antarctic ice divide between Dome Fuji and EPICA DML. The Cryosphere, 5(4): 1057-1081.

Fujita, S. and Mae, S., 1994. Causes and nature of ice-sheet radio-echo internal reflections estimated from the dielectric properties of ice. Annals of Glaciology, 20(1): 80-86.

Fujita, S. et al., 1999. Nature of radio echo layering in the Antarctic Ice Sheet detected by a two-frequency experiment. Journal of Geophysical Research: Solid Earth (1978–2012), 104(B6): 13013-13024.

Fujita, S., Matsuoka, T., Ishida, T., Matsuoka, K. and Mae, S., 2000. A summary of the complex dielectric permittivity of ice in the megahertz range and its applications for radar sounding of polar ice sheets. Physics of Ice Core Records: 185-212.

Gao, C., Robock, A. and Ammann, C., 2008. Volcanic forcing of climate over the past 1500 years: An improved ice core-based index for climate models. Journal of Geophysical Research: Atmospheres (1984–2012), 113(D23).

Gao, P., Mu, X.-M., Wang, F. and Li, R., 2011. Changes in streamflow and sediment discharge and the response to human activities in the middle reaches of the Yellow River. Hydrology & Earth System Sciences, 15(1).

Gershunov, A., 1998. ENSO influence on intraseasonal extreme rainfall and temperature frequencies in the contiguous United States: Implications for long-range predictability. Journal of Climate, 11(12): 3192-3203.

Giovinetto, M., Waters, N. and Bentley, C., 1990. Dependence of Antarctic surface mass balance on temperature, elevation, and distance to open ocean. Journal of Geophysical Research: Atmospheres (1984–2012), 95(D4): 3517-3531.

Gogineni, S., Prescott, G., Braaten, D., Allen, C. and Team, P., 2003. Polar radar for ice sheet measurements, INTERNATIONAL GEOSCIENCE AND REMOTE SENSING SYMPOSIUM. Citeseer, pp. III: 1607-1609.

Gregory, J.M., Huybrechts, P. and Raper, S.C., 2004. Climatology: Threatened loss of the Greenland ice-sheet. Nature, 428(6983): 616-616.

Gregory, S. and Noone, D., 2008. Variability in the teleconnection between the El Nino–Southern Oscillation and West Antarctic climate deduced from West Antarctic ice core isotope records. Journal of Geophysical Research: Atmospheres (1984–2012), 113(D17).

Griggs, J.A., Bamber, J. L., 2011. Antarctic ice-shelf thickness from satellite radar altimetry. Journal of Glaciology: 485-498.

Hamed, K.H. and Ramachandra Rao, A., 1998. A modified Mann-Kendall trend test for autocorrelated data. Journal of Hydrology, 204(1): 182-196.

Hammer, C.U., 1980. Acidity of polar ice cores in relation to absolute dating, past volcanism, and radio-echoes. Journal of Glaciology, 25: 359-372.

Harangozo, S., 2000. A search for ENSO teleconnections in the west Antarctic Peninsula climate in austral winter. International Journal of Climatology, 20(6): 663-679.

Harrison, C., 1973. Radio echo sounding of horizontal layers in ice. Journal of glaciology, 12: 383-397.

Hellmer, H., 2004. Impact of Antarctic ice shelf basal melting on sea ice and deep ocean properties. Geophysical Research Letters, 31(10).

Horwath, M., Legrésy, B., Blarel, F., Rémy, F., Lemoine, J.-M., 2012. Consistent patterns of Antarctic ice sheet interannual variations from ENVISAT radar altimetry and GRACE. Geophysical Journal International, 189(2): 863-876.

Horwath, M., Legrésy, B., Ramillien, G., Blarel, F., Rémy, F., Lemoine, J.-M., 2009. Antarctic and Greenland ice sheet changes seen by ENVISAT radar altimetry and GRACE: comparison and synthesis, EGU General Assembly, Vienna, pp. 7098.

Hu, Y. and Schennach, S.M., 2008. Instrumental variable treatment of nonclassical measurement error models. Econometrica, 76(1): 195-216.

Ivins, E.R. et al., 2013. Antarctic contribution to sea level rise observed by GRACE with improved GIA correction. Journal of Geophysical Research: Solid Earth, 118(6): 3126-3141.

Jacobel, R.W. and Hodge, S.M., 1995. Radar internal layers from the Greenland summit. Geophysical Research Letters, 22(5): 587-590.

Joughin, I. and Alley, R.B., 2011. Stability of the West Antarctic ice sheet in a warming world. Nature Geoscience, 4(8): 506-513.

Kanagaratnam, P., Gogineni, S.P., Ramasami, V. and Braaten, D., 2004. A wideband radar for high-resolution mapping of near-surface internal layers in glacial ice. Geoscience and Remote Sensing, IEEE Transactions on, 42(3): 483-490.

Kaspari, S. et al., 2004. Climate variability in West Antarctica derived from annual accumulation-rate records from ITASE firn/ice cores. Annals of Glaciology, 39(1): 585-594.

Kendall, M.G., 1948. Rank correlation methods.

King, J. et al., 2004. Wind-borne redistribution of snow across an Antarctic ice rise. Journal of Geophysical Research: Atmospheres (1984–2012), 109(D11).

King, M.A. et al., 2012. Lower satellite-gravimetry estimates of Antarctic sea-level contribution. Nature, 491(7425): 586-589.

Kulkarni, A. and von Storch, H., 1995. Monte Carlo experiments on the effect of serial correlation on the Mann-Kendall test of trend. Meteorologische Zeitschrift, 4(2): 82-85.

Lazzara, M.A., Weidner, G.A., Keller, L.M., Thom, J.E. and Cassano, J.J., 2012. ANTARCTIC AUTOMATIC WEATHER STATION PROGRAM. Bulletin of the American Meteorological Society, 93(10).

Lenaerts, J., den Broeke, M., Berg, W., Meijgaard, E.v. and Kuipers Munneke, P., 2012a. A new, high-resolution surface mass balance map of Antarctica (1979–2010) based on regional atmospheric climate modeling. Geophysical Research Letters, 39(4).

Lenaerts, J. et al., 2012b. Modeling drifting snow in Antarctica with a regional climate model: 1. Methods and model evaluation. Journal of Geophysical Research: Atmospheres (1984–2012), 117(D5).

Leuschen, C., 2010. IceBridge Snow Radar L1B Geolocated Radar Echo Strength Profiles. Boulder, Colorado USA: NASA DAAC at the National Snow and Ice Data Center.

Mayewski, P.A. et al., 2005. The international trans-antarctic scientific expedition (ITASE): an overview. Annals of glaciology, 41(1): 180-185.

Medley, B. et al., 2013. Airborne-radar and ice-core observations of annual snow accumulation over Thwaites Glacier, West Antarctica confirm the spatiotemporal variability of global and regional atmospheric models. Geophysical Research Letters, 40(14): 3649-3654.

Millar, D., 1982. Acidity levels in ice sheets from radio echo-sounding. Ann. Glaciol, 3: 199-203.

Monaghan, A.J., Bromwich, D.H. and Wang, S.-H., 2006. Recent trends in Antarctic snow accumulation from Polar MM5 simulations. Philosophical Transactions of the Royal Society A: Mathematical, Physical and Engineering Sciences, 364(1844): 1683-1708.

Moore, J., 1988. Dielectric variability of a 130 m Antarctic ice core: Implications for radar sounding. Ann. Glaciol, 11: 95-99.

Morse, D.L., Blankenship, D.D., Waddington, E.D. and Neumann, T.A., 2002. A site for deep ice coring in West Antarctica: Results from aerogeophysical surveys and thermo-kinematic modeling. Annals of Glaciology, 35(1): 36-44.

Morse, D.L. et al., 1999. Accumulation rate measurements at Taylor Dome, East Antarctica: Techniques and strategies for mass balance measurements in polar environments. Geografiska Annaler: Series A, Physical Geography, 81(4): 683-694.

Muszynski, I. and Birchfield, G., 1985. The dependence of Antarctic accumulation rates on surface temperature and elevation. Tellus A, 37(2): 204-208.

Nereson, N., Raymond, C., Jacobel, R. and Waddington, E., 2000. The accumulation pattern across Siple Dome, West Antarctica, inferred from radar-detected internal layers. Journal of Glaciology, 46(152): 75-87.

Oppenheimer, M., 1998. Global warming and the stability of the West Antarctic Ice Sheet. Nature, 393(6683): 325-332.

Panzer, B. et al., 2013. An ultra-wideband, microwave radar for measuring snow thickness on sea ice and mapping near-surface internal layers in polar firn. Journal of Glaciology, 59(214): 244-254.

Paren, G., 1975. Internal reflections in polar ice sheets. Journal oIG/aci% gy, 14(7I): I975.

Peterson, R.G. and White, W.B., 1998. Slow oceanic teleconnections linking the Antarctic Circumpolar Wave with the tropical El Niño-Southern Oscillation. Journal of Geophysical Research: Oceans (1978–2012), 103(C11): 24573-24583.

Pritchard, H. et al., 2012. Antarctic ice-sheet loss driven by basal melting of ice shelves. Nature, 484(7395): 502-505.

Rémy, F., Parouty, S., 2009. Antarctic Ice Sheet and Radar Altimetry: A Review. Remote Sensing: 1212-1239.

Rignot, E., 2006. Changes in ice dynamics and mass balance of the Antarctic ice sheet. Philosophical Transactions of the Royal Society A: Mathematical, Physical and Engineering Sciences, 364(1844): 1637-1655.

Rignot, E. et al., 2008. Recent Antarctic ice mass loss from radar interferometry and regional climate modelling. Nature Geoscience, 1(2): 106-110.

Rignot, E., Mouginot, J. and Scheuchl, B., 2011. Ice flow of the Antarctic ice sheet. Science, 333(6048): 1427-1430.

Rivard, C. and Vigneault, H., 2009. Trend detection in hydrological series: when series are negatively correlated. Hydrological processes, 23(19): 2737-2743.

Rotschky, G., Eisen, O., Wilhelms, F., Nixdorf, U. and Oerter, H., 2004. Spatial distribution of surface mass balance on Amundsenisen plateau, Antarctica, derived from ice-penetrating radar studies. Annals of Glaciology, 39(1): 265-270.

Schneider, D.P., Okumura, Y. and Deser, C., 2012. Observed Antarctic interannual climate variability and tropical linkages. Journal of Climate, 25(12): 4048-4066.

Sen, P.K., 1968. Estimates of the regression coefficient based on Kendall's tau. Journal of the American Statistical Association, 63(324): 1379-1389.

Sen Roy, S. and Balling, R.C., 2004. Trends in extreme daily precipitation indices in India. International Journal of climatology, 24(4): 457-466.

Seneviratne, S. et al., 2012. Changes in climate extremes and their impacts on the natural physical environment: An overview of the IPCC SREX report, EGU General Assembly Conference Abstracts, pp. 12566.

Shabtaie, S. and Bentley, C., 1988. Ice-thickness map of the West Antarctic ice streams by radar sounding. Ann. Glaciol, 11: 126-136.

Steig, E.J. et al., 2005. High-resolution ice cores from US ITASE (West Antarctica): Development and validation of chronologies and determination of precision and accuracy. Annals of Glaciology, 41(1): 77-84.

Stocker, T.F., Dahe, Q. and Plattner, G.-K., 2013. Climate Change 2013: The Physical Science Basis. Working Group I Contribution to the Fifth Assessment Report of the Intergovernmental Panel on Climate Change. Summary for Policymakers (IPCC, 2013).

Theil, H., 1992. A rank-invariant method of linear and polynomial regression analysis, Henri Theil's Contributions to Economics and Econometrics. Springer, pp. 345-381.

Tiuri, M.E., Sihvola, A.H., Nyfors, E. and Hallikaiken, M., 1984. The complex dielectric constant of snow at microwave frequencies. Oceanic Engineering, IEEE Journal of, 9(5): 377-382.

Trujillo, E., Ramírez, J.A. and Elder, K.J., 2007. Topographic, meteorologic, and canopy controls on the scaling characteristics of the spatial distribution of snow depth fields. Water resources research, 43(7).

Van der Veen, C., Ahn, Y., Csatho, B., Mosley-Thompson, E. and Krabill, W., 2009. Surface roughness over the northern half of the Greenland Ice Sheet from airborne laser altimetry. Journal of Geophysical Research: Earth Surface (2003–2012), 114(F1).

Veen, C. and Bolzan, J., 1999. Interannual variability in net accumulation on the Greenland Ice Sheet: Observations and implications for mass balance measurements. Journal of Geophysical Research: Atmospheres (1984–2012), 104(D2): 2009-2014.

Veen, C., Bromwich, D., Csatho, B. and Kim, C., 2001. Trend surface analysis of Greenland accumulation. Journal of Geophysical Research: Atmospheres (1984–2012), 106(D24): 33909-33918.

Velicogna, I., 2009. Increasing rates of ice mass loss from the Greenland and Antarctic ice sheets revealed by GRACE. Geophysical Research Letters, 36(19).

Wilcoxon, F. and Wilcox, R.A., 1964. Some rapid approximate statistical procedures. Lederle Laboratories.

Wingham, D., Shepherd, A., Muir, A. and Marshall, G., 2006. Mass balance of the Antarctic ice sheet. Philosophical Transactions of the Royal Society A: Mathematical, Physical and Engineering Sciences, 364(1844): 1627-1635.

Wingham, D.J., Shepherd, A., Muir, A., Marshall, G. J., 2006. Mass balance of the Antarctic ice sheet. Philosophical Transactions of the Royal Society A: 1627-1635.

Yuan, X., 2004. ENSO-related impacts on Antarctic sea ice: a synthesis of phenomenon and mechanisms. Antarctic Science, 16(04): 415-425.

Yue, S., Pilon, P., Phinney, B. and Cavadias, G., 2002. The influence of autocorrelation on the ability to detect trend in hydrological series. Hydrological Processes, 16(9): 1807-1829.

Zwally, H.J., Giovinetto, M. B., Li, J., Cornejo, H. G., Beckley, M. A., Brenner, A. C., Saba, J. L., Yi, D., 2005. Mass changes of the Greenland and Antarctic ice sheets and shelves and contributions to sea-level rise: 1992–2002. Journal of Glaciology, 51: 509-527.

7 Appendices

7.1 Mean and standard deviation of the three data sources

Table 7-1 Means and standard deviations of the Snow Radar and ITASE ice cores

Name	Mean	STD	Name	Mean	STD	Name	Mean	STD
ITASE-01-3	0.3443	0.0549	**ITASE-01-2**	0.4970	0.0680	**ITASE-00-1**	0.2507	0.0628
09-02-112	0.342806	0.059254	**09-02-143**	0.384899	0.062453	**09-02-170**	0.344363	0.050668
09-02-113	0.359443	0.061611	**09-02-144**	0.348749	0.055091	**09-02-171**	0.372479	0.054734
09-02-114	0.34318	0.051287	**09-02-145**	0.3552	0.050515	**09-02-172**	0.384232	0.054087
09-02-115	0.349882	0.06172	**09-02-146**	0.363613	0.05454	**09-02-173**	0.372572	0.058296
09-02-116	0.323858	0.055825	**09-02-147**	0.368625	0.057606	**09-02-174**	0.38254	0.064906
09-02-117	0.32423	0.055035	**09-02-148**	0.347347	0.054126	**09-02-175**	0.382594	0.064146
09-02-118	0.345376	0.056984	**09-02-149**	0.365369	0.057425	**09-02-176**	0.385017	0.071821
09-02-119	0.354349	0.056504	**09-02-150**	0.351586	0.066185	**09-02-177**	0.374284	0.063742
09-02-120	0.386944	0.059703	**09-02-151**	0.350624	0.062398	**09-02-178**	0.360115	0.0625
09-02-121	0.352893	0.056688	**09-02-152**	0.338939	0.05707	**09-02-179**	0.351865	0.064522
09-02-122	0.358565	0.054527	**09-02-153**	0.364002	0.060373	**09-02-180**	0.336002	0.059681
09-02-123	0.376141	0.053424	**09-02-154**	0.361118	0.06502	**09-02-181**	0.328635	0.059472
09-02-124	0.392182	0.061642	**09-02-155**	0.384597	0.063561	**09-02-182**	0.336782	0.056478
09-02-125	0.366623	0.053629	**09-02-156**	0.394372	0.061857	**09-02-183**	0.346982	0.052643
09-02-126	0.386331	0.059858	**09-02-157**	0.378148	0.065215	**09-02-184**	0.319133	0.056932
09-02-127	0.36329	0.050406	**09-02-158**	0.36277	0.062239	**09-02-185**	0.300944	0.049341
09-02-128	0.384321	0.057271	**09-02-159**	0.358632	0.06269	**09-02-186**	0.291416	0.051632
09-02-129	0.33419	0.049514	**09-02-160**	0.363288	0.06447	**09-02-187**	0.299806	0.046762
09-02-130	0.364582	0.057451	**09-02-161**	0.360398	0.061305	**09-02-188**	0.29398	0.039286
09-02-131	0.38516	0.054414	**09-02-162**	0.345874	0.06202	**09-02-189**	0.271749	0.033754
09-02-132	0.37695	0.056965	**09-02-163**	0.318107	0.053376	**09-02-190**	0.259838	0.028029
09-02-133	0.376491	0.056507	**09-02-164**	0.354657	0.056409	**09-02-191**	0.251543	0.034092
09-02-134	0.377887	0.056964	**09-02-165**	0.337941	0.055738	**09-02-192**	0.239683	0.037934
09-02-135	0.364371	0.054121	**09-02-166**	0.318634	0.055275	**09-02-193**	0.234583	0.036442
09-02-136	0.365327	0.053695	**09-02-167**	0.326713	0.060604	**09-02-194**	0.227304	0.051116

09-02-137	0.347512	0.050291	**09-02-168**	0.314011	0.050523	**09-02-195**	0.220739	0.04068
09-02-138	0.346163	0.050246	**09-02-169**	0.352542	0.056064	**09-02-196**	0.216523	0.03349
09-02-139	0.389595	0.053965						
09-02-140	0.42679	0.065826	**12-01-286**	0.414780	0.0565317			
09-02-141	0.405615	0.066411	**12-01-287**	0.4396359	0.0526718			
09-02-142	0.407354	0.063112	**12-01-288**	0.4201974	0.0527938			
			12-01-289	0.49659737	0.06178513			
			12-01-290	0.46330666	0.05214878			
			12-01-291	0.395135	0.055175			
			12-01-292	0.447698	0.068579			
			12-01-293	0.477163	0.055052			
			12-01-294	0.539104	0.064468			
			12-01-295	0.429508	0.062533			

Table 7-2 Means and standard deviations of the Snow Radar and RACMO2.1/ANT SWE series

Grid cell #	Mean of Snow Radar	STD of Snow Radar	Mean of Model data	STD of model data
1	0.351897	0.051614	0.327121	0.064775
2	0.371774	0.325875	0.050912	0.064935
3	0.369495	0.315899	0.048483	0.06473
4	0.365415	0.29868	0.048526	0.063297
5	0.365119	0.303599	0.049418	0.064559
6	0.389471	0.328117	0.052599	0.068555
7	0.38438	0.310071	0.053398	0.064065
8	0.368147	0.333342	0.05343	0.068116
9	0.367667	0.279506	0.056145	0.057247
10	0.386014	0.289623	0.059182	0.058196
11	0.365551	0.265714	0.05495	0.05127
12	0.346708	0.285877	0.051997	0.05343
13	0.353103	0.26638	0.050038	0.0493
14	0.390144	0.222081	0.055938	0.040741
15	0.379574	0.22712	0.058024	0.042521
16	0.356344	0.153322	0.055117	0.025871
17	0.331012	0.161584	0.045292	0.028263
18	0.303485	0.137821	0.034748	0.022368
19	0.263589	0.136991	0.027575	0.022296
20	0.396318	0.47044	0.083625	0.059877
21	0.45004	0.463014	0.053294	0.096259
22	0.438771	0.536303	0.050155	0.106803
23	0.413213	0.488908	0.056929	0.08967

7.2 Correlated coefficients and p-values between Snow Radar and ITASE Ice Core

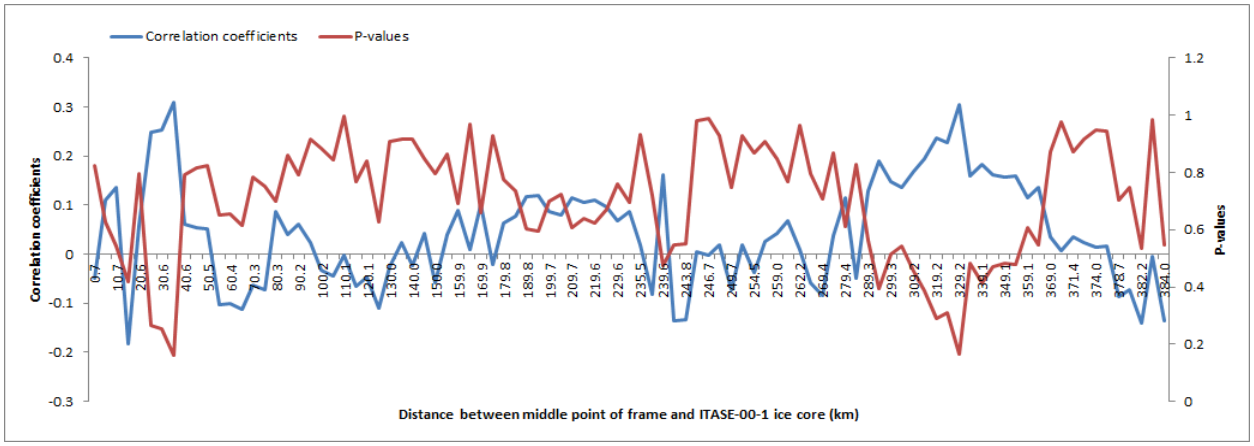

Figure 7.1 Correlation coefficients between Snow Radar and ITASE-00-1 ice core profile.

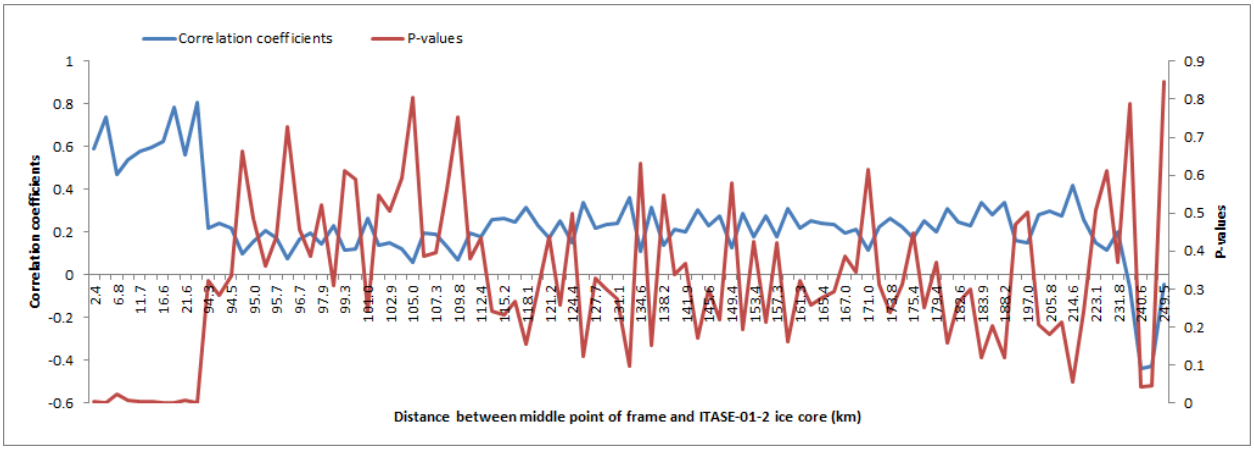

Figure 7.2 Correlation coefficients between Snow Radar and ITASE-01-2 ice core profile.

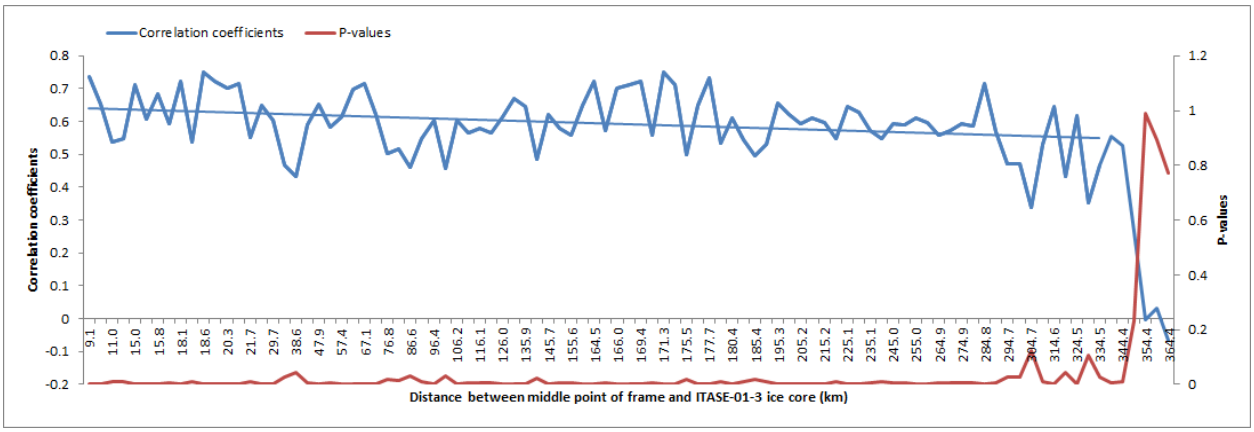

Figure 7.3 Correlation coefficients between Snow Radar and ITASE-01-3 ice core profile.

7.3 Trend Test Results

Table 7-3 S, t, z-value, and p-value of SWE series (Snow Radar, 1979-2011)

	Frames 112-142	Frames 143-169	Frames 170-196	Frames 286-295
S	2	10	10	-12
t	0.0038	0.0189	0.0189	-0.0227
Z-value	0.0310	0.1549	0.1549	-0.1859
P-value	0.5120	0.5596	0.5596	0.4286

Table 7-4 S, t, z-value, and p-value of SWE series (ITASE, 1979-2000/2001)

	ITASE-00-1	ITASE-01-2	ITASE-01-3
S	9	-6	0
t	0.0390	-0.0237	0
Z-value	0.2538	-0.1585	0
P-value	0.59871	0.44038	0.5

Table 7-5 S, t, z-value, and p-value of SWE series (RACMO2.1/ANT, 1979-2011)

	Part 1	Part 2	Part 3	Part 4
S	4	6	0	4
t	0.0076	0.0114	0	0.0076
Z-value	0.0620	0.0930	0	0.0620
P-value	0.5239	0.5359	0.5000	0.5239

7.4 Correlation coefficients and p-values between SWE and mean/median values of AWS and SIE data

Table 7-6 Correlation coefficient and p-value between SWE and mean/median values of AWS and SIE data

Name	R	P-value	R	P-valu	R	P-value	R	P-value
	T mean		T median		P mean		P median	
112-142	0.1898	0.40973	0.270444	0.2357	0.1094	0.636744	0.200269	0.38407
143-170	0.2260	0.32443	0.344947	0.1256	0.1257	0.586982	0.287315	0.20664
170-196	0.2305	0.31461	0.411170	0.0640	0.1414	0.540796	0.350265	0.11956
286-295	0.1007	0.66381	-0.066253	0.6024	0.1462	0.526898	-0.14437	0.53236

Mean temperature is shorten as T mean, median temperature is shorten as T median, mean pressure is shorten as P mean, and median pressure is shorten as P median.

7.5 Source Code

The codes used in this research are all programmed using Matlab and are included in CReSIS function data. Below is the list of functions and their usages:

(1) SnowRadarToWE.m: derive snow accumulation water-equivalent and layer depth for picking point and average them over frames.

```
function [depth,meanDep,WE,meanWE]=SnowRadarToWE(data,first,last,CoreDensity,CoreDep)
standData=interpAlongTrack(data,first,last);
depth=layerDepth(CoreDensity,CoreDep,standData);
for i=1:length(depth)
    depth(1,i).frames(1,:)='';
end
meanDep=averageF(depth);
midDep=Dep2midPt(meanDep);
% Insert your density/depth fitted line function here
density=-5e-8*midDep.^4+1e-5*midDep.^3-0.0006*midDep.^2+0.02*midDep+0.392;
[layerThick,WE]=waterEquiv(depth,density);
meanWE=averageF(WE);
```

(2) interpAlongTrack.m: interpolates layer data to surface GPS time.

```
function [standData]=interpAlongTrack(Data,first,last)
for i=first:last
    frame=Data(1,i);
    surface=frame.frames.layerData(Chen et al., 2009);
% Delete the duplicated points
    [surface.gps_time,o,p]=unique(surface.gps_time);
    [sort1,sort2]=sort(o);
    surface.longitude=surface.longitude(sort1);
    surface.latitude=surface.latitude(sort1);
```

```
    surface.elevation=surface.elevation(sort1);
    surface.twtt=surface.twtt(sort1);

    track=geodetic_to_along_track(surface.latitude,surface.longitude,surface.elevation);
    track0=[track(1,1):5:track(1,size(track,2))];
    surface.longitude=interp1(track,surface.longitude,track0,'linear','extrap');
    surface.latitude=interp1(track,surface.latitude,track0,'linear','extrap');
    surface.elevation=interp1(track,surface.elevation,track0,'linear','extrap');
    surface.twtt=interp1(track,surface.twtt,track0,'linear','extrap');
surface=struct('name',surface.name,'longitude',surface.longitude,'latitude',surface.latitude,'elevation'
,surface.elevation,'twtt',surface.twtt);
    layerData=struct('layers',surface);
    len=size(frame.frames.layerData,2);
    %interpolate every layer to surface and put them into the final result
    for j=2:len
        layer=frame.frames.layerData;
        [layer.gps_time,q,r]=unique(layer.gps_time);
        [sort1,sort2]=sort(q);
        layer.longitude=layer.longitude(sort1);
        layer.latitude=layer.latitude(sort1);
        layer.elevation=layer.elevation(sort1);
        layer.twtt=layer.twtt(sort1);
        track=geodetic_to_along_track(layer.latitude,layer.longitude,layer.elevation);
        newlon=interp1(track,layer.longitude,track0,'linear','extrap');
        newlat=interp1(track,layer.latitude,track0,'linear','extrap');
        newele=interp1(track,layer.elevation,track0,'linear','extrap');
        newtwtt=interp1(track,layer.twtt,track0,'linear','extrap');
newlayer=struct('name',layer.name,'longitude',newlon,'latitude',newlat,'elevation',newele,'twtt',newtwtt
);
        layerData(j)=struct('layers',newlayer);
    end
    if i==first
        standData=struct('frames',layerData);
    else
        standData(i-first+1)=struct('frames',layerData);
    end
end
```

(3) layerDepth.m: calculate layer depth profile from original Snow Radar.

```
function [result]=layerDepth(density,depth,standData)
```

```
nums=size(standData,2);
for i=1:nums
    oSurTwtt=standData(1,i).frames(1,1).layers.twtt;
    rows=size(standData(1,i).frames,2);
    for j=1:rows
        standData(1,i).frames(1,j).layers.twtt=standData(1,i).frames(1,j).layers.twtt-oSurTwtt;
    end
end
for k=1:nums
    rows=size(standData(1,k).frames,2);
    cols=size(standData(1,k).frames(1,1).layers.longitude,2);
    layerdepth=ones(rows,cols);
    density=density(1:rows,1);
    er=iceSummit(density);
    freq=5e9;
    depth=depth(1:rows,1);
    depth1=depth';
    [TWtime,gain] = genPropProfileFromPerm(depth1,er,freq);
    len=size(TWtime,1);
    depth1=depth1(1,2:len+1);
    for j=1:rows
        layer=standData(1,k).frames(1,j).layers;
        layer_twtt=layer.twtt;
        layer_depth = interp1(TWtime,depth1,layer_twtt,'linear','extrap');
        layerdepth(j,:)=layer_depth;
    end
    layerdepth=sortrows(layerdepth,1);
    surface=layerdepth(1,:);
    a=size(layerdepth,1);
    for m=1:a
        layerdepth(m,:)=layerdepth(m,:)-surface;
    end
    result(k)=struct('frames',layerdepth);
end
```

(4) averageF.m: calculate average value over a frame.

```
function [average]=averageF(frames)
numF=length(frames);
numF2=0;
for i=1:numF
```

```
    numF2=numF2+size(frames(1,i).frames,2);
end
numF1=size(frames(1,i).frames,1);
layer=zeros(numF1,numF2);

numF3=0;
for i=1:numF
    numF4=numF3;
    numF3=numF3+size(frames(1,i).frames,2);
    layer(:,numF4+1:numF3)=frames(1,i).frames;
end
average=mean(layer,2);
```

(5) Dep2midPt.m: convert depth to mid-point depth.

```
function [midPt]=Dep2midPt(depth)
num=length(depth);
midPt=zeros(num,1);
for i=1:num
    if i==1
        midPt(i,1)=depth(i,1)/2;
    else
        midPt(i,1)=depth(i,1)-(depth(i,1)-depth(i-1,1))/2;
    end
end
```

(6) waterEquiv.m: convert depth to snow accumulation water-equivalent.

```
function [layerThick,waterEquiv]=waterEquiv(layerDepth,density)
len=length(layerDepth);
for i=1:len
    depth=layerDepth(1,i).frames;
    row=size(depth,1);
    col=size(depth,2);
    thick=zeros(row,col);
    thick(1,:)=depth(1,:);
    for j=2:row
        thick(j,:)=depth(j,:)-depth(j-1,:);
    end
    if i==1
        layerThick=struct('frames',thick);
```

```
    else
        layerThick(i)=struct('frames',thick);
    end
end
for i=1:len
    thick=layerThick(1,i).frames;
    sizeOfThick=size(thick);
    row= sizeOfThick(1,1);
    col= sizeOfThick(1,2);
    waterE=zeros(row,col);
    for j=1:row
        waterE(j,:)=thick(j,:)*density(j,1);
    end
    if i==1
        waterEquiv=struct('frames',waterE);
    else
        waterEquiv(i)=struct('frames',waterE);
    end
end
```

As the original OpenPolarServer has been upgraded, the current data structure is revised for better performance. The above functions cannot be directly used now. An additional function, “adjustData.m”, should be run before the above functions.

(7) adjustData.m: rearrange the new data structure to fit the existed codes.

```
function [result]=adjustData(data,gap)
[lyr_id,q,r]=unique(data.properties.lyr_id);
numL=length(lyr_id);
% Separate different layer data from the raw data, after which the bigLayer structure stores layers
for i=1:numL
  if i==1
% Delete repeated data in surface
    surface_pos=find(data.properties.lyr_id==lyr_id(i));
    surface_gps_time=data.properties.gps_time(surface_pos);
    surface_twtt=data.properties.twtt(surface_pos);
    surface_lat=data.properties.lat(surface_pos);
    surface_lon=data.properties.lon(surface_pos);
```

```
    surface_ele=data.properties.elev(surface_pos);
    [surface_gps_time,q,r]=unique(surface_gps_time);
    surface_gps_time=surface_gps_time(q);
    surface_lon=surface_lon(q);
    surface_lat=surface_lat(q);
    surface_ele=surface_ele(q);
    surface_twtt=surface_twtt(q);
    track=geodetic_to_along_track(surface_lat,surface_lon,surface_ele);
    track0=[track(1,1):5:track(1,size(track,2))];
    surface_gps_time=interp1(track,surface_gps_time,track0,'linear','extrap');
    surface_lon=interp1(track,surface_lon,track0,'linear','extrap');
    surface_lat=interp1(track,surface_lat,track0,'linear','extrap');
    surface_ele=interp1(track,surface_ele,track0,'linear','extrap');
    surface_twtt=interp1(track,surface_twtt,track0,'linear','extrap');
surface=struct('name',lyr_id(i),'gps_time',surface_gps_time,'longitude',surface_lon,'latitude',surface_l
at,'elevation',surface_ele,'twtt',surface_twtt,'track',track0);
    bigLayer=struct('layers',surface);
  else
% Delete repeated data in each layer
    layer_pos=find(data.properties.lyr_id==lyr_id(i));
    layer_gps_time=data.properties.gps_time(layer_pos);
    layer_twtt=data.properties.twtt(layer_pos);
    layer_lat=data.properties.lat(layer_pos);
    layer_lon=data.properties.lon(layer_pos);
    layer_ele=data.properties.elev(layer_pos);
    [layer_gps_time,q,r]=unique(layer_gps_time);
    layer_gps_time=layer_gps_time(q);
    layer_lon=layer_lon(q);
    layer_lat=layer_lat(q);
    layer_ele=layer_ele(q);
    layer_twtt=layer_twtt(q);
    track=geodetic_to_along_track(layer_lat,layer_lon,layer_ele);
    layer_gps_time=interp1(track,layer_gps_time,track0,'linear','extrap');
    layer_lon=interp1(track,layer_lon,track0,'linear','extrap');
    layer_lat=interp1(track,layer_lat,track0,'linear','extrap');
    layer_ele=interp1(track,layer_ele,track0,'linear','extrap');
    layer_twtt=interp1(track,layer_twtt,track0,'linear','extrap');
layer=struct('name',lyr_id(i),'gps_time',layer_gps_time,'longitude',layer_lon,'latitude',layer_lat,'elev
ation',layer_ele,'twtt',layer_twtt,'track',track0);
    bigLayer(i)=struct('layers',layer);
  end
```

```
end
% Calculate the number of parts this segment needs to be broke into
len=ceil(length(surface_gps_time)/gap);
ends=[1:len];
ends=ends*gap;
ends(1,len)=length(surface_gps_time);
% Create layers structure to store layer data
for i=1:len
  surface=bigLayer(1).layers;
  if i==1
    surface_gps_time1=surface.gps_time(1:ends(i));
    surface_lon1=surface.longitude(1:ends(i));
    surface_lat1=surface.latitude(1:ends(i));
    surface_ele1=surface.elevation(1:ends(i));
    surface_twtt1=surface.twtt(1:ends(i));
    surface_track1=surface.track(1:ends(i));
  else
    surface_gps_time1=surface.gps_time(ends(i-1)+1:ends(i));
    surface_lon1=surface.longitude(ends(i-1)+1:ends(i));
    surface_lat1=surface.latitude(ends(i-1)+1:ends(i));
    surface_ele1=surface.elevation(ends(i-1)+1:ends(i));
    surface_twtt1=surface.twtt(ends(i-1)+1:ends(i));
    surface_track1=surface.track(ends(i-1)+1:ends(i));
  end
surface=struct('name',1,'gps_time',surface_gps_time1,'longitude',surface_lon1,'latitude',surface_lat1,'e
levation',surface_ele1,'twtt',surface_twtt1);
  layerData=struct('layers',surface);
  for j=2:numL
    layer=bigLayer(j).layers;
% Find the layer point that cover the same GPS time with the selected surface range
    minTrack=min(surface_track1);
    maxTrack=max(surface_track1);
    layerI=find(layer.track>=minTrack & layer.track<=maxTrack);
    layer_gps_time1=layer.gps_time(layerI);
    layer_lat1=layer.latitude(layerI);
    layer_lon1=layer.longitude(layerI);
    layer_ele1=layer.elevation(layerI);
    layer_twtt1=layer.twtt(layerI);
    layer_track1=layer.track(layerI);
    newGPS=interp1(layer_track1,layer_gps_time1,surface_track1,'linear','extrap');
    newlon=interp1(layer_track1,layer_lon1,surface_track1,'linear','extrap');
```

```
    newlat=interp1(layer_track1,layer_lat1,surface_track1,'linear','extrap');
    newele=interp1(layer_track1,layer_ele1,surface_track1,'linear','extrap');
    newtwtt=interp1(layer_track1,layer_twtt1,surface_track1,'linear','extrap');
newlayer=struct('name',lyr_id(j),'gps_time',newGPS,'longitude',newlon,'latitude',newlat,'elevation',newe
le,'twtt',newtwtt);
    layerData(j)=struct('layers',newlayer);
  end
  if i==1
    result=struct('frames',layerData);
  else
    result(i)=struct('frames',layerData);
  end
end
```

(8) TFPWMannKendall.m: perform the TFPW Mann-Kendall trend test for a given number series.

```
function [S,Z,t]=TFPWMannKendall(ranking)
len=length(ranking);
t=[1:len]';
n=len*(len-1)/2;
%Step 1: Remove the series trend using TSA
bS=zeros(1,n);
count=1;
for i=1:len
    for j=i+1:len
        b1=(ranking(j,1)-ranking(i,1))/(j-i);
         bS(1,count)=b1;
         count=count+1;
    end
end
b=median(King et al.);
ranking=ranking-b.*t;
%Step 2: Remove the correlation using the lag-1 autocorrelation coefficient
r1=0;
r2=0;
for i=2:len
    r1=(ranking(i,1)*ranking(i-1,1))+r1;
end
for i=1:len
    r2=(ranking(i,1)*ranking(i,1))+r2;
end
```

```
r=r1/r2;
ranking=ranking-r.*ranking;
%Step 3: Put back the slope in the series
ranking=ranking+b.*t;
%Step 4: Apply the non-parametric Mann-Kendall test to the modified series (of step 3)
data1=ranking(1:len-1);
data2=ranking(2:len);
S=0;
for i=1:len-1
    if data1(i,1)-data2(i,1)<0
         S=S+1;
    elseif data1(i,1)-data2(i,1)==0
        S=S+0;
    else
        S=S-1;
    end
end
varS=len*(len-1)*(2*len+5)/18;
Z=S/(varS^0.5);
t=2*S/(len*(len-1));
```